THE KINEMATICS AND DYNAMICS OF POLOIDAL–TOROIDAL COUPLING IN MANTLE FLOW: THE IMPORTANCE OF SURFACE PLATES AND LATERAL VISCOSITY VARIATIONS

ALESSANDRO M. FORTE*
Department of Earth and Planetary Science
Harvard University
Cambridge, Massachusetts 02138

W. RICHARD PELTIER
Department of Physics
University of Toronto
Toronto, Ontario
Canada M5S 1A1

1. INTRODUCTION

The ability of the mantle and lithosphere to creep over geologic time scales is due to the presence of naturally occurring atomic-scale defects in the lattice of crystal grains (e.g., Weertman and Weertman, 1975; Carter, 1976; Nicolas and Poirier, 1976; Weertman, 1978). The imposition of deviatoric stresses causes these defects to propagate and thus allows mantle material to creep or "flow." If the ambient temperature is sufficiently high, this solid-state flow will persist so long as the stress is maintained and the deformation process may achieve steady state. The steady-state creep of crystalline substances may be characterized by a single parameter, the effective viscosity (e.g., Stocker and Ashby, 1973; Weertman and Weertman, 1975).

This effective viscosity η provides the link between imposed deviatoric stress and resulting deviatoric strain rate as follows:

$$\tau_{ij} = 2\eta\ E_{ij}, \tag{1}$$

in which E_{ij} is the deviatoric strain-rate tensor and τ_{ij} is the deviatoric stress tensor. The deviatoric strain-rate tensor is defined in terms of the material flow velocity $\mathbf{u}$ as follows:

$$E_{ij} = \frac{1}{2}\left(\partial_i u_j + \partial_j u_i - \frac{2}{3}\,\partial_k u_k \delta_{ij}\right), \tag{2}$$

where $\partial_i \equiv \partial/\partial x_i$. Solid-state creep in crystalline media generally occurs by two independent mechanisms: dislocation glide and climb (e.g., Weertman, 1968) and diffusion of point defects through crystal grains and/or along grain boundaries (e.g., Herring, 1950; Coble, 1963; Green, 1970). The theoretical expression for

*Present address: Institut de Physique du Globe, Département de Sismologie, 75252 Paris, France

the effective viscosity, derived from detailed consideration of these creep mechanisms, is

$$\eta = Ad^m \tau^{1-n} kT \exp\left[\frac{\Delta E + P\Delta V}{kT}\right], \tag{3}$$

where A is a dimensional constant that depends on the details of the creep mechanism, d is the effective size of crystal grains, $\tau = [\tau_{ij}\tau_{ij}]^{1/2}$ is the square root of the second stress-tensor invariant (Stocker and Ashby, 1973), k is Boltzmann's constant, T is the absolute temperature, ΔE is the diffusion activation energy, ΔV is the diffusion activation volume, and P is the total pressure.

The theoretical expression (3) for the effective viscosity of crystalline media is useful for understanding the importance of viscosity variations in the Earth's mantle. If mantle creep occurred dominantly through diffusion of point defects, the effective viscosity in (3) would be independent of stress (i.e., $n = 1$). The grain-size dependence of diffusion creep is quite pronounced and $m = 2$ for Herring (bulk) diffusion and $m = 3$ for Coble (grain-boundary) diffusion. If mantle creep instead occurred through propagation of dislocations, the effective viscosity will be insensitive to grain size (i.e., $m = 0$) and sensitive to the ambient deviatoric stress, with the stress exponent $n \approx 3$ being typical (e.g., Weertman, 1968; Carter, 1976). In either creep mechanism, steady-state creep is ultimately dependent on the creation and diffusion of point defects and is therefore thermally activated. This is manifested by the exponential temperature dependence in (3). The effective viscosity of the mantle is therefore expected to be most sensitive to variations in temperature. Over the past decade numerous studies have also indicated the importance of chemical environment (e.g., the presence of H_2O and CO_2) on the effective viscosity of mantle rocks (e.g., Kohlstedt and Hornack, 1981; Ricoult and Kohlstedt, 1985; Karato *et al.*, 1986; Borch and Green, 1987). The dependence of effective viscosity on grain size, stress, pressure, temperature, and chemical environment implies that the viscosity of the mantle is expected to be very heterogeneous, owing to the lateral and depth variation of these thermodynamic state variables.

The significant mathematical difficulties arising from the treatment of arbitrary three-dimensional (3D) viscosity variations have led to an overwhelming focus on mantle flow models in which the viscosity is assumed to be constant, or to vary with depth only. Such simplifications have nonetheless led to a deep understanding of the basic physics underlying the thermal convection process responsible for the "drift" of the Earth's tectonic plates and the global variation of surface heat flux (e.g., Turcotte and Oxburgh, 1967; McKenzie *et al.*, 1974; Peltier, 1972, 1985; Jarvis and McKenzie, 1980; Jarvis and Peltier, 1982; Solheim and Peltier, 1990, 1993, 1994; Peltier and Solheim, 1992).

Theoretical modeling of mantle flow, based on the simplifying approximation that the viscosity depends only on depth, culminated with the development of

models that are used to predict the 3D mantle circulation expected on the basis of seismically inferred lateral density heterogeneity (e.g., Richards and Hager, 1984; Ricard *et al.,* 1984; Forte and Peltier, 1987, 1991a). Such flow modeling has demonstrated that the observed long-wavelength nonhydrostatic geoid may be successfully described in terms of the seismically inferred global heterogeneity in the mantle (e.g., Hager *et al.,* 1985; Forte and Peltier, 1987, 1991a; Hager and Clayton, 1989; Forte *et al.,* 1992). There therefore appears to be no evidence in the long-wavelength geoid data, or indeed the dynamic surface topography data (Forte *et al.,* 1993a), for the presence of a significant effect due to lateral variations of mantle viscosity. Since such lateral heterogeneity must exist if the crystalline mantle is in a state of motion determined by the thermal convection process, the success of these simple models would appear to indicate that the dynamics of flow in a laterally heterogeneous mantle are such that the existence of lateral rheology variations does not significantly impact surface observables such as dynamic topography and nonhydrostatic geoid anomalies.

The inadequacy of flow models which assume a spherically symmetric viscosity distribution becomes truly apparent only by considering the observed motions of the tectonic plates (e.g., Hager and O'Connell, 1981; Forte and Peltier, 1987). In a fluid shell with spherically symmetric viscosity, buoyancy forces excite only poloidal flow (which produces a pattern of purely converging or diverging flow at the surface) and thus fails completely to account for the strong toroidal (i.e. strike–slip) component of actual plate motions (e.g., Hager and O'Connell, 1981; Forte and Peltier, 1987). The observed equipartitioning of kinetic energy between poloidal and toroidal plate motions is a direct consequence of the plate-like mechanical structure of the lithosphere. This equipartitioning has also been investigated by O'Connell *et al.* (1991), who suggest that the present-day ratio of toroidal to poloidal energy in the plate motions appears to be nearly a minimum. A detailed consideration of the relationship between toroidal energy and the strike–slip motion of plates at transform faults has been presented by Olson and Bercovici (1991).

The mere existence of plates, with their "weak" boundaries and relatively "strong" interiors, implies that the effective viscosity of the lithosphere exhibits extreme lateral variations. The mathematical difficulties of dealing explicitly with such extreme variations of rheology have motivated several studies that attempt to overcome these difficulties by directly employing the observed plate motions (e.g., Hager and O'Connell, 1981) or by employing the geometry of the plates as a surface boundary condition (e.g., Ricard and Vigny, 1989; Forte and Peltier, 1991a,b; Gable *et al.,* 1991). Such treatments of the plates are essentially kinematic. To model the plates in a dynamically consistent manner, and to understand the rheologic coupling of poloidal and toroidal surface flow, requires an explicit treatment of lateral viscosity variations.

The mathematical modeling of lateral viscosity variations in numerical simu-

lations of thermal convection has been almost exclusively carried out in two-dimensional (2D) Cartesian geometry. Perhaps the most complete of such studies, in the detailed investigation of stress-, temperature-, and pressure-dependent viscosity, is that by Christensen (1984). An investigation of the coupling between distinct Fourier harmonic components of the flow field due to lateral viscosity variations in a 2D Cartesian geometry has also been carried out by Richards and Hager (1989). Such studies, confined to 2D geometries, are intrinsically limited because they cannot describe the excitation of toroidal flows and their coupling to poloidal flows. A treatment of poloidal–toroidal coupling requires a full 3D modeling approach.

Numerical investigations of lateral viscosity variations in 3D thermal convection simulations are relatively recent. Christensen and Harder (1991) have carried out simulations with temperature-dependent viscosity in a 3D Cartesian geometry. Recent high-Rayleigh-number simulations of thermal convection in 3D Cartesian geometry, with temperature-dependent viscosity, have also been performed by Tackley (1993).

Initial investigations of the effects of lateral viscosity variations in 3D spherical geometry have been rather limited in scope (e.g., Ricard *et al.,* 1988; Stewart, 1992) and are marred by questionable assumptions. (These difficulties are described later in this chapter.) Significant progress is now being made on the basis of several dynamically consistent formulations of the effects of lateral viscosity variations in the lithosphere (e.g., Ribe, 1992; Forte, 1992) and throughout the entire volume of the mantle (e.g., Forte, 1992; Čadek *et al.,* 1993; Martinec *et al.,* 1993; Zhang and Christensen, 1993).

In this chapter we present a complete description of the recent theoretical developments and results outlined in Forte (1992). We describe three rather different but complementary methods for investigating the effects of lateral rheology variations on mantle–lithosphere flow. In Section 2 we present a formalism for calculating buoyancy-induced plate motions that explicitly satisfy the constraint that each plate moves only by a rigid-body rotation. Although this formalism has been previously employed to model plate motions in Forte and Peltier (1991a,b), a complete mathematical description has not been presented. In Section 2 we therefore provide a detailed derivation of this formalism and illustrate its implications through several calculations of buoyancy-induced plate motions. The essentially kinematic approach described in Section 2 allows us to avoid an explicit consideration of lateral viscosity variations, but we then lose any understanding of the dynamic processes that generate toroidal flow and determine its coupling to poloidal flow.

In Section 3 we therefore present a dynamically consistent treatment of lithospheric flow in which the effects of lateral viscosity variations are explicitly included. We therein assume that these variations are important only in the litho-

sphere and may be neglected in the underlying mantle. This assumption allows us to formulate an inverse problem that we solve for the lateral viscosity variations in the lithosphere that are consistent with the observed plate velocities.

It is not obvious, however, that lateral variations of viscosity in the deep mantle are in fact negligible. The seismically inferred lateral variations of elastic-wave speeds are significant throughout the mantle and the associated temperature variations are expected, from Eq. (3), to yield significant lateral variations of effective viscosity. In Section 4 we therefore provide a complete description of a formalism that allows us to model the effects of 3D viscosity variations in a spherical fluid shell. This theory is based on a variational formulation of the principle of momentum conservation and provides a mathematically efficient, and physically transparent, description of flow dynamics. This formalism, which was initially outlined in Forte (1992), represents the principal contribution of this chapter. In Section 5 we summarize our main conclusions.

The reader will note that the discussion in the main text makes frequent reference to the mathematical Appendixes. In these Appendixes we have assembled, and in many cases derived, the principal tools required for a mathematical analysis of flow dynamics in spherical shells with lateral viscosity variations and rigid-surface plates. While the relegation of much of the formal material to these Appendixes has helped to streamline the discussion in the main text, the material is essential for the comprehension of our analysis.

2. Buoyancy-Driven Plate Motions

The existence of rigid surface plates with weak boundaries represents an extreme manifestation of lateral variations of effective viscosity in the Earth. Hager and O'Connell (1981) proposed a procedure for avoiding the explicit treatment of such rheologic variations that involves matching the stresses exerted by buoyancy-driven flows, acting on a no-slip surface, with the external stresses associated with a prescribed plate velocity field. This procedure was modified somewhat in Gable *et al.* (1991) and Ricard and Vigny (1989), in which the stresses exerted by buoyancy-driven flow acting on a no-slip surface are matched with the imposed surface stresses arising from some generally prescribed field of plate-like surface velocities. This matching then provided the required plate-motion parameters (e.g. the plate angular-velocity vectors). An important simplifying assumption in this approach is that the stresses acting on the plate boundaries are taken to be identically zero. As pointed out in Hager and O'Connell (1981), this assumption is questionable and does not account for the possibly significant collision-related stresses at subduction zones or shear stresses along transform boundaries. Such difficulties motivated the development, described in Forte and Peltier (1991a,b), of a different

approach to the problem of buoyancy-induced plate motions that does not make any *a priori* assumptions concerning the state of stress in the plates. The mathematical development and implementation of this approach is described fully below for the first time.

2.1. Analytic Description of Surface Plate Kinematics

The existence of effectively rigid plates constrained to the move on the surface of a sphere implies, by Euler's theorem (e.g., Goldstein, 1980), that the surface velocity field $\mathbf{v}(\theta, \phi)$ of N plates may be represented by the superposition of the rigid-body rotations of each plate:

$$\mathbf{v}(\theta, \phi) = \sum_{i=1}^{N} H_i(\theta, \phi)\, \boldsymbol{\omega}^i \times \mathbf{r}, \tag{4}$$

where $H_i(\theta, \phi) = 1$ wherever plate i is located and $H_i(\theta, \phi) = 0$ elsewhere, $\boldsymbol{\omega}^i$ is the angular velocity vector of plate i, and $\mathbf{r}$ is the position vector of any location on the Earth's surface. The trivial identity $\Sigma H_i(\theta, \phi) = 1$ may be employed to rewrite (4) as

$$\mathbf{v}(\theta, \phi) = \sum_{i=1}^{N-1} H_i(\theta, \phi)(\boldsymbol{\omega}^i - \boldsymbol{\omega}^N) \times \mathbf{r} + \boldsymbol{\omega}^N \times \mathbf{r}. \tag{5}$$

The last term on the right-hand side of (5) represents a net rotation of the lithosphere with angular velocity of plate N. It is clear that, apart from this net rotation, the surface velocity field is entirely given by the relative rotations of each plate relative to plate N. For example, the Nuvel-1 model (DeMets *et al.*, 1990) specifies the plate velocity field by arbitrarily fixing the Pacific plate (i.e., assuming $\boldsymbol{\omega}_{\text{Pacific}} = 0$). A convenient representation for the relative rotation rate $\boldsymbol{\omega}^i - \boldsymbol{\omega}^N$ is given by

$$\boldsymbol{\omega}^i - \boldsymbol{\omega}^N = \nabla\Omega_i, \tag{6}$$

where

$$\Omega_i = x_1(\omega_1^i - \omega_1^N) + x_2(\omega_2^i - \omega_2^N) + x_3(\omega_3^i - \omega_3^N), \tag{7}$$

where x_1, x_2, x_3 are the Cartesian coordinates of any position $\mathbf{r}$ on the Earth's surface and ω_j^i represents the jth Cartesian component of the rotation-rate vector $\boldsymbol{\omega}^i$. In analogy to Eqs. (6) and (7) we also have

$$\boldsymbol{\omega}^N = \nabla\Omega^N, \tag{8}$$

$$\Omega^N = x_1\omega_1^N + x_2\omega_2^N + x_3\omega_3^N. \tag{9}$$

Inserting Eqs. (6) and (8) into Eq. (5), we obtain

$$\mathbf{v}(\theta, \phi) = -\sum_{i=1}^{N-1} H_i(\theta, \phi)\, \mathbf{\Lambda}\Omega_i - \mathbf{\Lambda}\Omega^N, \tag{10}$$

where $\mathbf{\Lambda} = \mathbf{r} \times \nabla$ is related to the angular-momentum operator (see Backus, 1958, and Appendix I). The horizontal divergence $\nabla_H \cdot \mathbf{v}$ and radial vorticity $\hat{\boldsymbol{r}} \cdot \nabla \times \mathbf{v}$ provide a complete scalar characterization of the observed plate velocities (Forte and Peltier, 1987), and using Eq. (10) we obtain

$$\nabla_H \cdot \mathbf{v} = -\frac{1}{a} \sum_{i=1}^{N-1} [\nabla_1 H_i \cdot \mathbf{\Lambda}\Omega_i], \tag{11}$$

$$\hat{\boldsymbol{r}} \cdot \nabla \times \mathbf{v} = \frac{1}{a} \mathbf{\Lambda} \cdot \mathbf{v} = -\frac{1}{a} \sum_{i=1}^{N-1} [\mathbf{\Lambda} H_i \cdot \mathbf{\Lambda}\Omega_i + H_i \Lambda^2 \Omega_i] - \frac{1}{a} \Lambda^2 \Omega^N, \tag{12}$$

where $r = a$ is the radius of the Earth's solid surface, ∇_1 is the horizontal gradient operator on the unit sphere (see Appendix I), and $\Lambda^2 = \mathbf{\Lambda} \cdot \mathbf{\Lambda}$ is the horizontal Laplacian operator.

In Appendix III we derive the following analytic expressions for the spherical harmonic coefficients of the divergence and vorticity fields in Eqs. (11) and (12):

$$(\nabla_H \cdot \mathbf{v})_\ell^m = \sum_{i=1}^{N-1} \sum_{j=1}^{3} (S_j^i)_\ell^m (\omega_j^i - \omega_j^N), \tag{13}$$

$$(\hat{\boldsymbol{r}} \cdot \nabla \times \mathbf{v})_\ell^m = \sum_{i=1}^{N-1} \sum_{j=1}^{3} (R_j^i)_\ell^m (\omega_j^i - \omega_j^N) + \sum_{j=1}^{3} \delta_{\ell 1} N_j^m \omega_j^N, \tag{14}$$

in which

$$(S_j^i)_\ell^m, \quad (R_j^i)_\ell^m, \quad N_j^m$$

are defined in Appendix III and $\delta_{\ell 1} = 0$ whenever $\ell \neq 1$. In (14) we observe that the net lithospheric rotation associated with the rotation of plate N affects only the degree $\ell = 1$ component of the radial vorticity field and has no effect on the horizontal divergence coefficients in (13). For degrees $\ell > 1$ the horizontal divergence and radial vorticity fields are sensitive to the rotation of each plate relative only to the rotation of the (arbitrarily specified) Nth plate. On the basis of the explicit expressions for the elements

$$(S_j^i)_\ell^m \quad \text{and} \quad (R_j^i)_\ell^m$$

derived in Appendix III we find

$$(S_j^i)_\ell^m \equiv F_j[(H_i)_{\ell+2}^m, (H_i)_\ell^m, (H_i)_{\ell-2}^m], \tag{15}$$

$$(R_j^i)_\ell^m \equiv G_j[(H_i)_{\ell+1}^m, (H_i)_{\ell-1}^m], \tag{16}$$

in which we emphasize that $(S_j^i)_\ell^m$ is a (linear) function F_j of only the degree $\ell + 2, \ell, \ell - 2$ components of the plate functions $H_i(\theta, \phi)$ and $(R_j^i)_\ell^m$ is a (linear) function G_j of only the degree $\ell + 1, \ell - 1$ components of the same plate functions. This implies that the degree ℓ components of the horizontal divergence are sensitive only to the degree $\ell + 2, \ell, \ell - 2$ components of the plate geometry while the degree ℓ radial vorticity depends only on the degree $\ell + 1, \ell - 1$ plate geometry. The plate divergence and vorticity fields thus provide an independent and complementary sampling of the geometry of the surface plates. If, for example, we have a hypothetical planet with only two hemispherical surface plates [when the boundary between the plates coincides with the equator we can easily verify that the harmonic coefficients of each plate function vanish for even degrees ℓ thus, according to the rotational invariance expressed in Eq. (4.14) of Edmonds (1960), we know this will be true for any orientation of the boundary between the two plates] then the spherical harmonic coefficients of the horizontal divergence will vanish for even degrees ℓ while the radial vorticity coefficients will vanish for odd degrees ℓ.

To illustrate the actual use of expressions (13) and (14) let us first consider the simple example of the hypothetical planet with two hemispherical surface plates whose mutual boundary coincidences with the equator. It is straightforward to demonstrate that the harmonic coefficients of plate 1 (the northern-hemisphere plate) and plate 2 (the southern-hemisphere plate) are given by

$$
\begin{aligned}
(H_1)_\ell^m &= \delta_{m0}\left[\frac{1}{2}\,\delta_{\ell 0} + \frac{P_{\ell-1}^m(0)}{\ell+1}\sqrt{\frac{2\ell+1}{2\ell-1}}\,(1-\delta_{\ell 0})\right], \\
(H_2)_\ell^m &= \delta_{m0}\left[\frac{1}{2}\,\delta_{\ell 0} - \frac{P_{\ell-1}^m(0)}{\ell+1}\sqrt{\frac{2\ell+1}{2\ell-1}}\,(1-\delta_{\ell 0})\right],
\end{aligned}
\tag{17}
$$

in which $\delta_{m0} = 0$ whenever $m \neq 0$, $\delta_{\ell 0} = 0$ whenever $\ell \neq 0$, and $P_\ell^m(x)$ is the associated Legendre function that is normalized so that its root-mean-square (rms) amplitude is 1. In Fig. 1a we plot the amplitude spectrum of $H_1(\theta, \phi)$ in which we may observe the clear $1/\ell$ amplitude dependence demonstrated in Eq. (17). The horizontal gradients of the plate functions in Eqs. (11) and (12) are essentially equivalent to multiplication by ℓ (see Appendix III), in the space of spherical harmonics, and therefore we expect the plate divergence and vorticity fields to have a flat amplitude spectrum. This expectation is confirmed in Fig. 1b, in which we plot the amplitude spectrum of the divergence and vorticity fields, calculated using Eqs. (13), (14), and (17), for the following choice of plate rotation vectors:

$$
\boldsymbol{\omega}_1 = \omega\hat{\boldsymbol{z}}, \qquad \boldsymbol{\omega}_2 = \omega\left(-\frac{1}{2}\hat{\boldsymbol{x}} - \frac{\sqrt{3}}{2}\hat{\boldsymbol{z}}\right); \qquad \omega = 1^\circ/\text{Myr} \tag{18}
$$

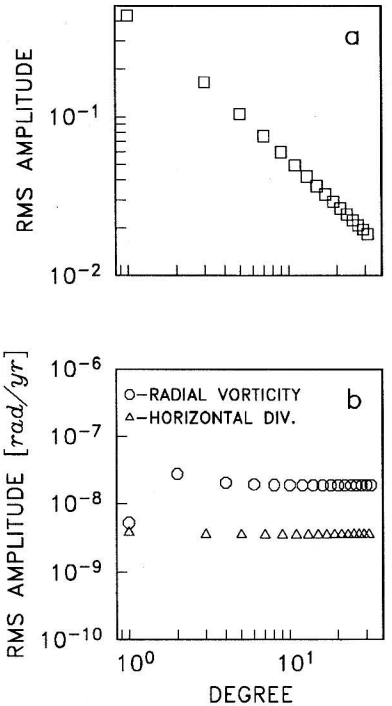

FIG. 1. (a) The root-mean-square (rms) amplitude, at each spherical harmonic degree, of the hemispherical plate function $H(\theta, \phi)$ defined by Eq. (17) in the text. (b) The rms amplitude (units rad/yr), at each degree, for the horizontal divergence and radial vorticity of the two rotating hemispherical plates, with geometry defined by Eq. (17). The rotation vectors of the two plates are specified by Eq. (18) in the text.

(where 1°/Myr = 1 degree per million years). In Fig. 2 we show maps of the actual two-plate divergence and vorticity fields, in which we observe the usual Gibbs side lobes that arise in any truncated series representation of discontinuous fields. An effective means for suppressing such side lobes is to multiply each harmonic coefficient of the divergence and vorticity fields by the following "Lanczos smoothing" factor (Lanczos, 1961; Justice, 1978):

$$L_\ell^m = \left[\frac{\sin(m\pi/M)}{m\pi/M}\right]\left[\frac{\sin(\ell\pi/L)}{\ell\pi/L}\right]. \tag{19}$$

The values of L and M may be set equal to the maximum degree and order employed in the truncated harmonic representation of the given surface field. It should be understood that when either $m = 0$ or $\ell = 0$ the value of L_ℓ^m in (19) is

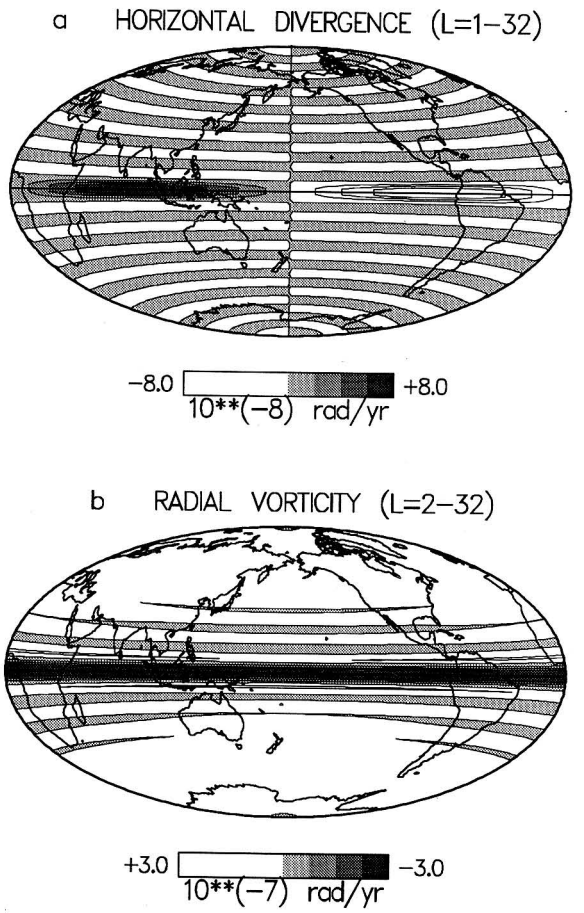

FIG. 2. The horizontal divergence and radial vorticity fields due to the rotation [given by Eq. (18) in the text] of the two hemispherical plates defined by Eq. (17). (a) The divergence field [units 10^{-8} (rad/yr)] is synthesized from the spherical harmonic coefficients, defined by Eq. (13), corresponding to degrees $\ell = 1-32$. The shaded areas indicate regions of positive divergence, and unshaded areas indicate negative divergence. (b) The radial vorticity field (units 10^{-7} rad/yr) is synthesized from coefficients, defined by Eq. (14), corresponding to degrees $\ell = 2-32$. The shaded areas indicate regions of negative vorticity (local clockwise circulation).

determined by the limit $\sin x/x \to 1$ as $x \to 0$. In Fig. 3 we show the effect of applying this Lanczos smoothing (when $L = M = 32$) to the original (unsmoothed) divergence and vorticity fields in Fig. 2.

We now consider the application of Eqs. (13) and (14) to the observed plate motions on the Earth's surface. In Fig. 4a we show the amplitude spectrum of the plate functions $H_i(\theta, \phi)$ corresponding to three different tectonic plates. The very

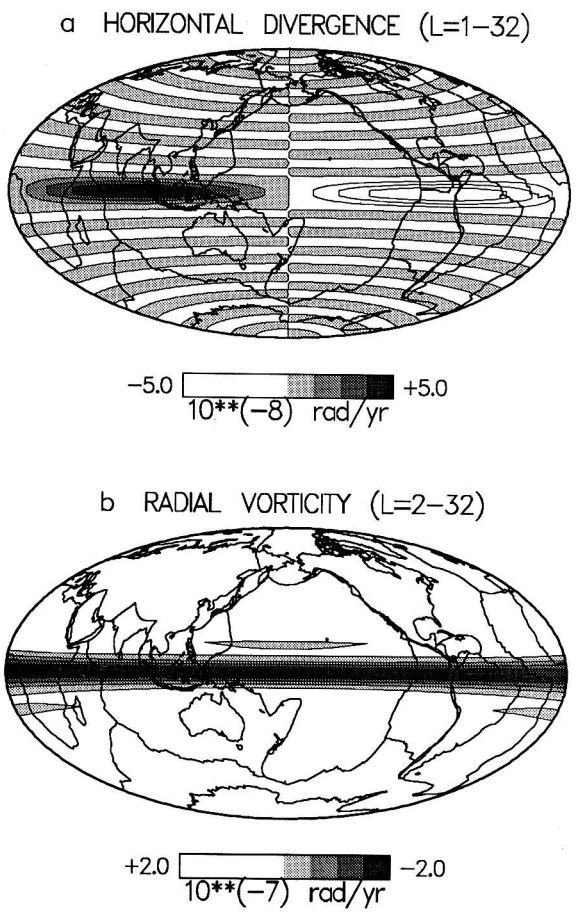

FIG. 3. The smoothed horizontal divergence and radial vorticity fields obtained by multiplying the harmonic coefficients of the corresponding fields in Fig. 2 by the Lanczos smoothing factors in Eq. (19) of the text, with $L = M = 32$.

large African and Pacific plates have an amplitude spectrum that displays the $1/\ell$ variation characteristic of the hemispheric plate shown in Fig. 1a. The smaller Cocos plate instead displays the flat spectrum more characteristic of a very small disk (i.e., a 2D delta function). In Fig. 4b we show the amplitude spectrum of the plate divergence and vorticity calculated according to (13) and (14) and employing the plate rotation vectors for the absolute-motion model AM1-2 of Minster and Jordan (1978). In this calculation we treat the Pacific plate as the Nth reference plate in (13) and (14). In Fig. 4b we observe a relatively flat amplitude spectrum, as in Fig. 1b, arising from the dominating contribution of the largest

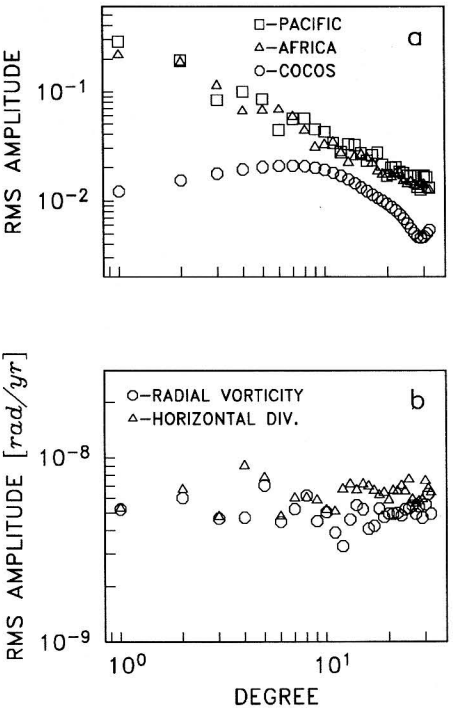

FIG. 4. (a) The rms amplitude, at each spherical harmonic degree, of the plate functions $H_i(\theta, \phi)$ corresponding to the Pacific, African, and Cocos tectonic plates. (b) The rms amplitude (units rad/yr), at each degree, of the horizontal divergence and radial vorticity of the tectonic plate velocities described by the rotation vectors in model AM1-2 of Minster and Jordan (1978).

(e.g., Pacific and African) plates. The smaller (e.g., Cocos) plates contribute to the detailed variability in the amplitude spectrum for large degrees ℓ. The maps of the plate divergence and vorticity synthesized from a truncated sum (up to degree $\ell = 32$) of their harmonic coefficients are very "noisy," due to the strong Gibbs side lobes. We therefore multiplied these coefficients by the smoothing factors in (19) for $L = M = 32$ and the resulting smoothed divergence and vorticity fields are shown in Fig. 5. The horizontal plate divergence in Fig. 5a is clearly dominated by the fast-spreading rates along the East Pacific ridge and the associated convergence along the western Pacific plate boundary. The radial plate vorticity in Fig. 5b is similarly dominated by the strong vorticity along the edges of the Pacific plate. It is worth noting that the observed strong radial vorticity in zones of strong divergence or convergence is a striking departure from the simple model of pure convergence (or divergence) over zones of downwelling (or upwelling) in a fluid with laterally homogeneous rheology.

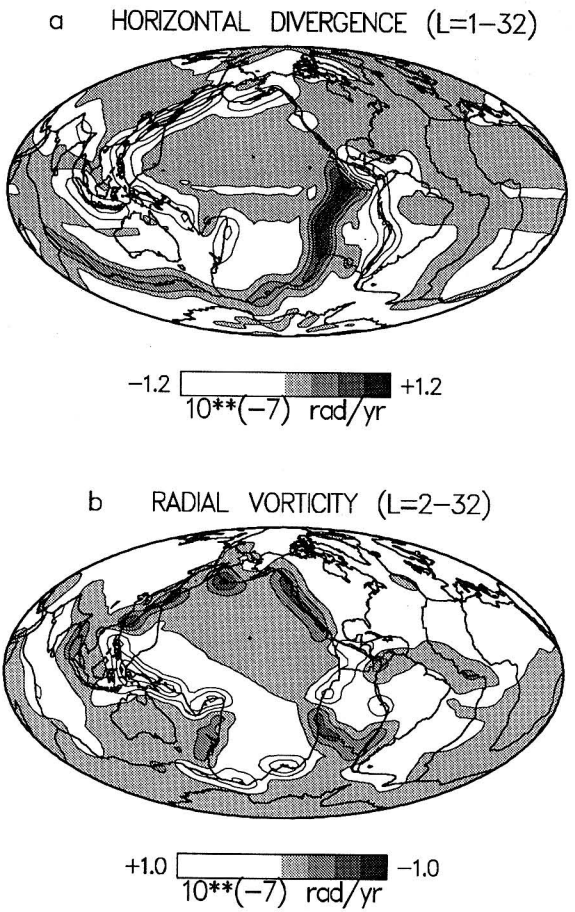

FIG. 5. The smoothed horizontal divergence and radial vorticity of the tectonic plate motions given by the absolute-motion model AM1-2 of Minster and Jordan (1978). The smoothing is performed by multiplying the harmonic coefficients of the divergence and vorticity fields by the Lanczos smoothing factor in Eq. (19), with $L = M = 32$. (a) The divergence field (units 10^{-7} rad/yr) is synthesized from the harmonic coefficients in the range $\ell = 1–32$. (b) The radial vorticity field (units 10^{-7} rad/yr) is synthesized from harmonic coefficients in the range $\ell = 2–32$.

2.2. Buoyancy-Driven Plate Motions

Theory

The theory of buoyancy-induced plate motions employed by Forte and Peltier (1991a,b) is based on the explicit recognition of the limited class of surface plate

motions that are realizable. We begin our development of this theory by rewriting expressions (13) and (14) as the following matrix equations:

$$\mathbf{d} = \underline{\mathbf{S}}\, \Delta\boldsymbol{\omega} \tag{20}$$

$$\boldsymbol{\nu} = \underline{\mathbf{R}}\Delta\boldsymbol{\omega} + \underline{\mathbf{N}}\boldsymbol{\omega}^N, \tag{21}$$

in which $\mathbf{d}$ and $\boldsymbol{\nu}$ are column vectors consisting of the spherical harmonic coefficients $(\nabla_H \cdot \mathbf{v})_\ell^m$ and $(\hat{\boldsymbol{r}} \cdot \nabla \times \mathbf{v})_\ell^m$ respectively, $\underline{\mathbf{S}}$ and $\underline{\mathbf{R}}$ are matrices consisting of the elements $(S_j^i)_\ell^m$ and $(R_j^i)_\ell^m$ in (13) and (14), $\Delta\boldsymbol{\omega}$ is a column vector consisting of the Cartesian components of the relative plate rotations $\omega_j^i - \omega_j^N$, $\underline{\mathbf{N}}$ is the matrix consisting of the elements $\delta_{\ell 1} N_j^m$ in (14), and $\boldsymbol{\omega}^N$ is a column vector consisting of the Cartesian components of the angular velocity of plate N. The matrix $\underline{\mathbf{S}}$ in (20) may be represented by its Lanczos (1961) decomposition [a useful discussion of this decomposition, also called a *singular-value decomposition,* may be found in Aki and Richards (1980)]:

$$\underline{\mathbf{S}} = \underline{\mathbf{U}}\, \underline{\Lambda}\, \underline{\mathbf{V}}^T, \tag{22}$$

in which $\underline{\mathbf{U}}$ and $\underline{\mathbf{V}}$ are orthonormal matrices ($\underline{\mathbf{U}}^T\underline{\mathbf{U}} = \underline{\mathbf{I}} = \underline{\mathbf{V}}^T\underline{\mathbf{V}}$) and $\underline{\Lambda}$ is a diagonal matrix consisting of the singular values of $\underline{\mathbf{S}}$. The columns of $\underline{\mathbf{V}}$ constitute a subset of the totality of all vectors spanning the space of plate rotation vectors $\Delta\boldsymbol{\omega}$. If the singular values in $\underline{\Lambda}$ are all nonzero, then the columns of $\underline{\mathbf{V}}$ span the entire space of rotation vectors $\Delta\boldsymbol{\omega}$ (i.e., $\underline{\mathbf{V}}\,\underline{\mathbf{V}}^T = \underline{\mathbf{I}}$). The columns of $\underline{\mathbf{U}}$ constitute the particular set of vectors that span all permissible *plate-like* horizontal divergence fields [it is obvious from Eqs. (20) and (22) that any field of plate divergence will be given by a linear superposition of the column vectors in $\underline{\mathbf{U}}$]. Since the harmonic coefficients of any realizable plate divergence field must be given by a linear superposition of the columns of $\underline{\mathbf{U}}$, we introduce the following projection operator $\underline{\mathbf{P}}$:

$$\underline{\mathbf{P}} = \underline{\mathbf{U}}\, \underline{\mathbf{U}}^T, \tag{23}$$

which acts on any given column vector $\mathbf{d}_0$ to yield a new column vector $\mathbf{d}_1$,

$$\mathbf{d}_1 = \underline{\mathbf{P}}\, \mathbf{d}_0, \tag{24}$$

in which the elements of $\mathbf{d}_1$ constitute the harmonic coefficients of a realizable field of plate divergence. If the elements of $\mathbf{d}_0$ already constitute the harmonic coefficients of a plate-like divergence field, then it is clear that $\underline{\mathbf{P}}\mathbf{d}_0 = \mathbf{d}_0$. Since the $\underline{\mathbf{S}}$ matrix in (20) is dependent only on the geometry of the plates [see Eq. (15)], it is clear that the projection operator will also be solely dependent on the plate geometry.

In practice we inevitably work with truncated sums of harmonic coefficients, and therefore it is worth understanding the impact of this truncation on the prop-

erties of the projection operator. From expression (15) we know that all the elements in any row of the $\underline{\mathbf{S}}$ matrix in (22), which correspond to degree ℓ of the plate divergence field, are dependent only on the degree $\ell + 2$, ℓ, $\ell - 2$ coefficients of the complete harmonic expansion of the plate functions. It is clear from (22) that this dependence also applies to the matrix $\underline{\mathbf{U}}$ in (23) and therefore an element P_{ij} of the (in practice) finite-dimensional projection matrix $\underline{\mathbf{P}}$ will contain a representation of the degree $\ell + 2$, ℓ, $\ell - 2$ plate coefficients that is uncorrupted by the use of the truncated harmonic sum representation of the plates. This representation will obviously appear more "plate-like" as the maximum degree ℓ in the sum is increased. This increased "plateness" is achieved by increasing the column and row dimension of the projection matrix $\underline{\mathbf{P}}$ while preserving the elements P_{ij} that were already calculated.

Forte and Peltier (1987) have shown that the buoyancy-induced surface flow, in a model of the mantle that has no lateral viscosity variations, may be uniquely represented by its horizontal divergence:

$$(\nabla_H \cdot \mathbf{u})^m_\ell = \frac{g_0}{\eta_0} \int_b^a D_\ell(r) \delta\rho^m_\ell(r)\, dr, \tag{25}$$

in which $(\nabla_H \cdot \mathbf{u})^m_\ell$ are the spherical harmonic coefficients of the horizontal divergence of the predicted surface flow, g_0 is the gravitational acceleration (which is nearly constant in the mantle), η_0 is a reference (scaling value) viscosity for the mantle, $r = a$ and b are respectively the radii of the solid surface and core–mantle boundary, $\delta\rho^m_\ell(r)$ are radially varying spherical harmonic coefficients of the internal density contrasts, and $D_\ell(r)$ are kernel functions whose behavior also depends on the radial profile of relative viscosity $\eta(r)/\eta_0$ in the mantle. Depending on the particular field of density perturbations $\delta\rho^m_\ell$ assumed for the mantle, the predicted surface divergence in (25) will generally not be "plate-like." A plate-like divergence field $(\nabla_H \cdot \mathbf{v})^t_s$ may be obtained from the flow-induced divergence $(\nabla_H \cdot \mathbf{u})^m_\ell$ in (25) by applying the projection operator $\underline{\mathbf{P}}$ described in (23) and (24):

$$(\nabla_H \cdot \mathbf{v})^t_s = P_{st,\ell m} (\nabla_H \cdot \mathbf{u})^m_\ell, \tag{26}$$

in which the combination st and ℓm in $P_{st,\ell m}$ defines a particular row and column, respectively, of the $\underline{\mathbf{P}}$ matrix. If we now substitute (25) into (26), we obtain

$$(\nabla_H \cdot \mathbf{v})^t_s = \frac{g_0}{\eta_0} \int_b^a D_s(r) \delta\hat{\rho}^t_s(r)\, dr, \tag{27}$$

in which

$$\delta\hat{\rho}^t_s(r) = [D_s^{-1}(r) P_{st,\ell m} D_\ell(r)] \delta\rho^m_\ell(r). \tag{28}$$

The density perturbations $\delta\hat{\rho}^t_s(r)$ defined in (28) give rise to a surface divergence field in (27) that is perfectly plate-like (i.e., corresponds to a plate divergence

produced by rigid-body rotations of the plates). On the basis of expression (28) we define a new radially varying projection operator $\hat{P}_{st,\ell m}(r)$:

$$\hat{P}_{st,\ell m}(r) = D_s^{-1}(r) P_{st,\ell m} D_\ell(r), \tag{29}$$

which possesses the fundamental property of all projection operators, namely, $\underline{\hat{\mathbf{P}}}^2 = \underline{\hat{\mathbf{P}}}$ (from Eq. (23) we see that $\underline{\mathbf{P}}^2 = \underline{\mathbf{P}}$). The operator $\underline{\hat{\mathbf{P}}}$ will be uniquely dependent on the geometry of the surface plates and the radial viscosity profile of the mantle [the latter is implicitly contained in the divergence kernels $D_\ell(r)$ and $D_s(r)$ in (29)].

The projection operator $\underline{\hat{\mathbf{P}}}$ defined in (29) allows us to partition any given field of density perturbations $\delta\rho_\ell^m(r)$ in the mantle into two orthogonal components $\delta\hat{\rho}_s^t(r)$ and $\delta\overline{\rho}_s^t(r)$ as follows:

$$\delta\hat{\rho}_s^t(r) = \hat{P}_{st,\ell m}(r)\delta\rho_\ell^m(r), \tag{30}$$

$$\delta\overline{\rho}_s^t(r) = [\delta_{st,\ell m} - \hat{P}_{st,\ell m}(r)]\delta\rho_\ell^m(r), \tag{31}$$

in which (30) is simply Eq. (28) rewritten and $\delta_{st,\ell m}$ is the Kronecker delta ($\delta_{i,j} = 0$ when $i \neq j$ and $\delta_{i,j} = 1$ when $i = j$). The density perturbations $\delta\hat{\rho}_s^t(r)$, delivered by (30), give rise to realizable surface plate motions, while the density perturbations $\delta\overline{\rho}_s^t(r)$ cannot give rise to plate motions [note that $\hat{P}_{st,\ell m}(r)\ \delta\overline{\rho}_\ell^m(r) = 0$]. The mantle flow driven by the density perturbations $\delta\hat{\rho}_s^t(r)$ should be modeled with a free-slip surface boundary condition, while the flow driven by the density perturbations $\delta\overline{\rho}_s^t(r)$ should be modeled with a no-slip surface boundary condition. The surface plates are effectively "locked" into their positions by the mantle flow driven by $\delta\overline{\rho}_s^t(r)$. The density perturbations $\delta\overline{\rho}_s^t(r)$ constitute that portion of the internal mantle heterogeneity that is invisible with respect to the observable plate motions. This last point is clearly important because it shows that the interpretation of past and present plate motions (e.g., Richards and Engebretson, 1992) in terms of density perturbations in the mantle is entirely nonunique. This nonuniqueness will be illustrated in several examples below.

On the basis of the plate-like surface divergence driven by the $\delta\hat{\rho}_s^t(r)$ component of the internal density perturbations, we may determine the corresponding plate rotation vectors $\boldsymbol{\omega}^i - \boldsymbol{\omega}^N$. The generalized inverse $\underline{\mathbf{S}}^\dagger$ of the matrix $\underline{\mathbf{S}}$ in (22) is given by

$$\underline{\mathbf{S}}^\dagger = \underline{\mathbf{V}}\ \underline{\boldsymbol{\Lambda}}^{-1}\ \underline{\mathbf{U}}^T \tag{32}$$

From Eq. (20) we see that the action of $\underline{\mathbf{S}}^\dagger$ on a column vector $\mathbf{d}$, consisting of the harmonic coefficients of the plate-like surface divergence in (27), will yield a column vector $\Delta\boldsymbol{\omega}^\dagger$:

$$\Delta\boldsymbol{\omega}^\dagger = \underline{\mathbf{S}}^\dagger\ \mathbf{d}, \tag{33}$$

in which the elements of $\Delta\boldsymbol{\omega}^\dagger$ are the relative plate rotations $\boldsymbol{\omega}^i - \boldsymbol{\omega}^N$ consistent with the flow-induced surface divergence. It is worth emphasizing that the hori-

zontal divergence field can only constrain the angular velocity vectors of the plates relative to that of some arbitrarily selected reference plate (i.e., plate N). If one or more of the singular values in the diagonal matrix $\underline{\mathbf{\Lambda}}$ are zero, then certain combinations of plate rotations will produce zero plate divergence. The columns of the $\underline{\mathbf{V}}$ matrix in (22), which correspond to the zero singular values, define the plate rotations that produce zero plate divergence. In this situation, the plate rotations delivered by (33) will obviously describe only the restricted class of plate rotations that produce a nonvanishing plate divergence. If we now insert (33) into (21) we obtain

$$\boldsymbol{\nu} = \underline{\mathbf{C}}\mathbf{d} + \underline{\mathbf{N}}\boldsymbol{\omega}^N, \tag{34}$$

in which the coupling matrix

$$\underline{\mathbf{C}} = \underline{\mathbf{R}}\underline{\mathbf{S}}^{\dagger}, \tag{35}$$

describes the radial vorticity of the plates, which arises from the buoyancy-induced plate rotations given by Eq. (33). The coupling matrix $\underline{\mathbf{C}}$ in (35) is dependent only on the geometry of the surface plates.

At this juncture it is worth considering the assertion, by Ricard and Vigny (1989), that a model of buoyancy-induced plate motions cannot describe degree $\ell = 1$ toroidal motion (i.e., a net lithospheric rotation). The coupling matrix $\underline{\mathbf{C}}$ in (34) does indeed give rise to a degree $\ell = 1$ toroidal motion, on the basis of the flow-induced plate-like divergence $\mathbf{d}$. This predicted degree 1 toroidal plate motion is, however, incomplete. A complete specification of the degree 1 toroidal motion also requires knowing the absolute rotation $\boldsymbol{\omega}^N$ of the Nth plate. This absolute rotation cannot be determined on the basis of the theory presented here (see, however, Section 4.7 below).

Examples

We shall now consider several applications of the theory of buoyancy-induced plate motions described in the previous section. An important ingredient in this theory is the calculation of the horizontal divergence kernels $D_\ell(r)$ in Eq. (25). These kernels are a function of the assumed relative viscosity profile $\eta(r)/\eta_0$ of the mantle. The surface observable that is most sensitive to the depth variation of this relative viscosity is the predicted nonhydrostatic geoid. In Fig. 6 (left panel) we thus show the relative mantle viscosity inferred by Forte *et al.* (1993b) on the basis of the fits to the observed nonhydrostatic geoid provided by the seismic heterogeneity model SH8/WM13 of Woodward *et al.* (1993). In Fig. 6 (right panel) we also show the inferred density–velocity proportionality, $\partial \ln \rho / \partial \ln v_s$, which is employed to convert the $\delta v_s / v_s$ heterogeneity in model SH8/WM13 to an equivalent field of density heterogeneity $\delta\rho$. The divergence kernels $D_\ell(r)$ which are calculated on the basis of the geoid-inferred viscosity profile are shown

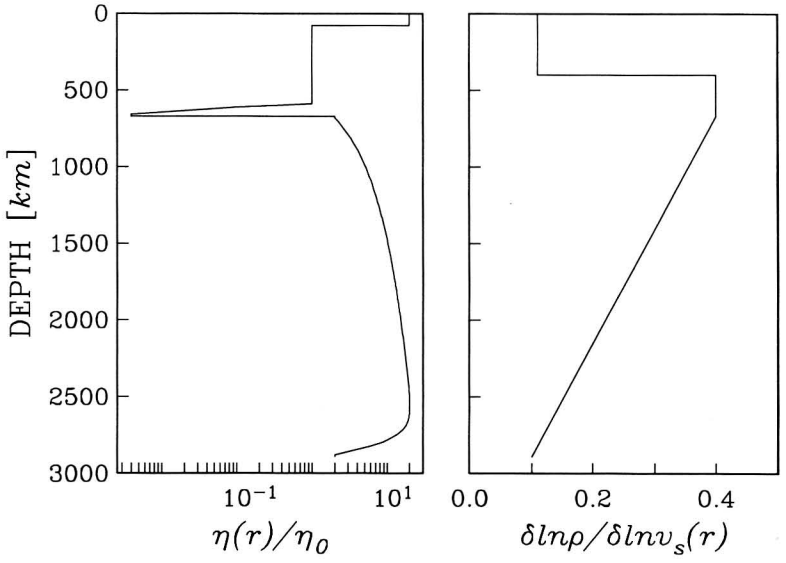

FIG. 6. In the left panel is shown the relative viscosity profile $\eta(r)/\eta_0$ inferred from the nonhydrostatic geoid by Forte *et al.* (1993b). In the right panel is shown the depth-varying proportionality between density perturbations and shear velocity perturbations in the mantle.

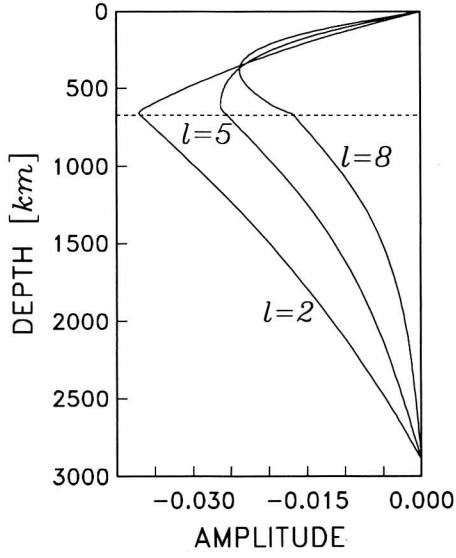

FIG. 7. The horizontal divergence kernels $D_\ell(r)$, defined in Eq. (25), calculated for the relative viscosity profile shown in Fig. 6. The kernels were calculated for a compressible mantle according to the method described in Forte and Peltier (1991a). The location of the 670-km seismic discontinuity is indicated by the dashed horizontal line.

in Fig. 7, where we observe that long-wavelength density heterogeneity near the bottom of the upper mantle excites surface flow most effectively.

We shall first illustrate the interaction of buoyancy-induced mantle flow with surface plates by considering the mantle flow driven only by the degree $\ell = 2$ density heterogeneity derived from model SH8/WM13 of Woodward *et al.* (1993). In Fig. 8a we show the degree 2 surface horizontal divergence that is predicted for a mantle without surface plates. In this calculation we convolve the degree 2 divergence kernel in Fig. 7 with the degree 2 density perturbation in the mantle according to Eq. (25) [in which we select $\eta_0 = 10^{21}$ Pa s (pascal seconds) on the basis of the postglacial rebound analysis of Peltier (1982, 1989)]. In Fig. 8b we show the result of the interaction of the flow in Fig. 8a with a hypothetical lithosphere consisting of two hemispherical surface plates whose mutual boundary coincides with the equator (this geometry was considered previously in Figs. 1 and 2 and in Eq. (17)). The surface divergence in Fig. 8b was calculated according to Eq. (27), in which the density perturbations $\delta\hat{\rho}^t_s(r)$ were obtained using the projection operator [in Eq. (29)] calculated for the two hemispherical plates. The elements of the projection operator in Eq. (29) were calculated on the basis of a spherical harmonic description of the plate functions $H_i(\theta, \phi)$ up to degree and order 32. However, for numerical convenience, we employ only the elements of the operator $\hat{P}_{st,\ell m}(r)$ that correspond to $s \leqslant 15$, $\ell \leqslant 15$. It is clear, from the amplitude scale in Fig. 8b, that the projection operator has almost completely annihilated the internal density perturbation and thus yields a vanishingly small surface divergence. This example illustrates the importance of the alignment between the plate-boundary geometry and the geometry of the upwellings and downwellings in underlying mantle flow. It is rather clear that the symmetry of the mantle flow in Fig. 8a is such that the hemispherical plates in Fig. 8b will be essentially "locked" into position. In Fig. 8c we now observe the result of the interaction of the mantle flow in Fig. 8a with the actual geometry of surface plates (represented by a spherical harmonic expansion up to degree and order 32). In this case we observe that the peak amplitude of the surface divergence is similar to the peak amplitude obtained in the absence of plates (Fig. 8a). The observed surface plates are apparently aligned favorably with respect to the mantle flow derived from even the longest wavelength (degree 2) seismic heterogeneity. In Fig. 9 we show that the surface plate motions in Fig. 8c agree rather well with the observed plate motions, on horizontal length scales which are much smaller than that of the internal degree 2 density perturbations.

We shall now consider the interaction of the observed surface plates with the mantle flow driven by all components (up to degree and order 8) of the mantle heterogeneity given by model SH8/WM13 of Woodward *et al.* (1993). The shear velocity heterogeneity in model SH8/WM13 is converted to density heterogeneity using the $\partial \ln \rho / \partial \ln v_s$ values in Fig. 6 (right panel). The resulting field of density perturbations is partitioned by the plate-projection operator according to (30) and

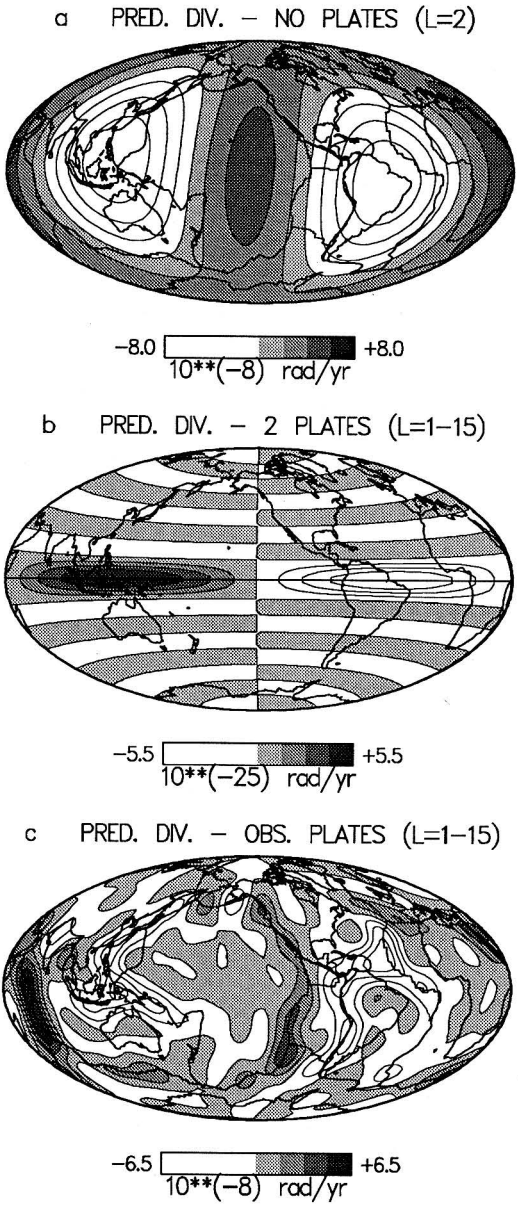

FIG. 8. (a) The degree 2 horizontal divergence predicted [according to Eq. (25)] with model SH8/WM13, using the $\delta \ln \rho / \delta \ln v_s$ conversion in Fig. 6 and the divergence kernels in Fig. 4. Units are 10^{-8} rad/yr. (b) The horizontal divergence, in the range ℓ 1–15, due to the interaction of the degree 2 mantle flow in (a) with a lithosphere consisting of two hemispherical plates with their boundary at the equator. This plate-like divergence field was calculated according to Eq. (27). Units are 10^{-25} rad/yr. (c) The plate-like horizontal divergence, in the range $\ell = 1-15$, due to the interaction of the degree 2 mantle flow in (a) with the actual plates on the Earth's surface. The units are 10^{-8} rad/yr. In calculating the flow shown in (a), (b) and (c), a reference viscosity value $\eta_0 = 10^{21}$ Pa s was employed.

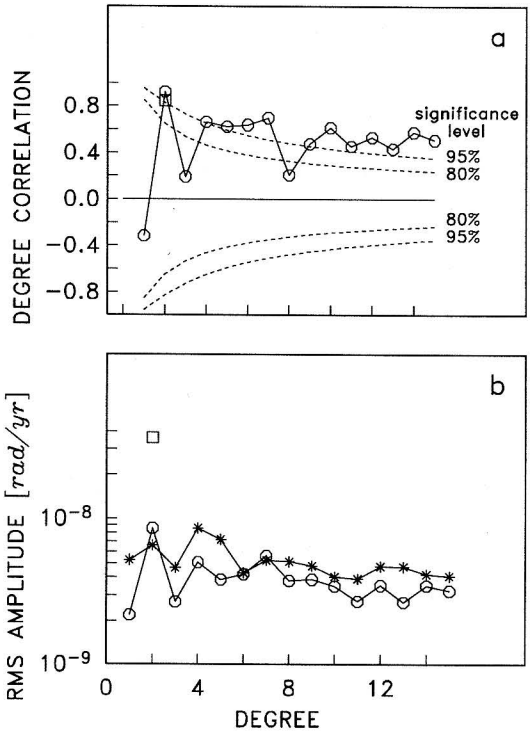

FIG. 9. (a) The cross-correlation, at each harmonic degree ℓ, between the observed plate divergence (shown in Fig. 5a) and the degree 2 divergence in Fig. 8a (□, "no plates"), the plate-like divergence in Fig. 8c (○, "with plates"). (b) The rms amplitude, at each degree, of the observed plate divergence (*, "observed"), the degree 2 divergence (□, "no plates"), and the plate-like divergence (○, "with plates"). Units are rad/yr.

(31) and the plate-like surface divergence is calculated according to (27) (in which we employ the divergence kernels in Fig. 7). The projection operator is calculated on the basis of a spherical harmonic description of the plate functions $H_i(\theta, \phi)$ up to degree and order 32. For numerical convenience, we employ only the elements of the operator $\hat{P}_{st,\ell m}(r)$ that correspond to $s \leqslant 15$, $\ell \leqslant 15$. In Fig. 10b we show the predicted plate-like surface divergence along with the surface divergence of the observed plate velocities in Fig. 10a. The agreement between the two maps is clearly very good, and the predicted divergence in Fig. 10b accounts for 70% of the variance of the observed divergence in Fig. 10a. This good match is achieved by selecting the value of the reference viscosity in Eq. (27) to be $\eta_0 = 10^{21}$ Pa s. On the basis of the relative viscosity $\eta(r)/\eta_0$ in Fig. 6 (left panel), we thus infer an absolute viscosity of 10^{21} Pa s in most of the upper mantle and the absolute viscosity at the top of the lower mantle is 2.0×10^{21} Pa s (increasing linearly to a

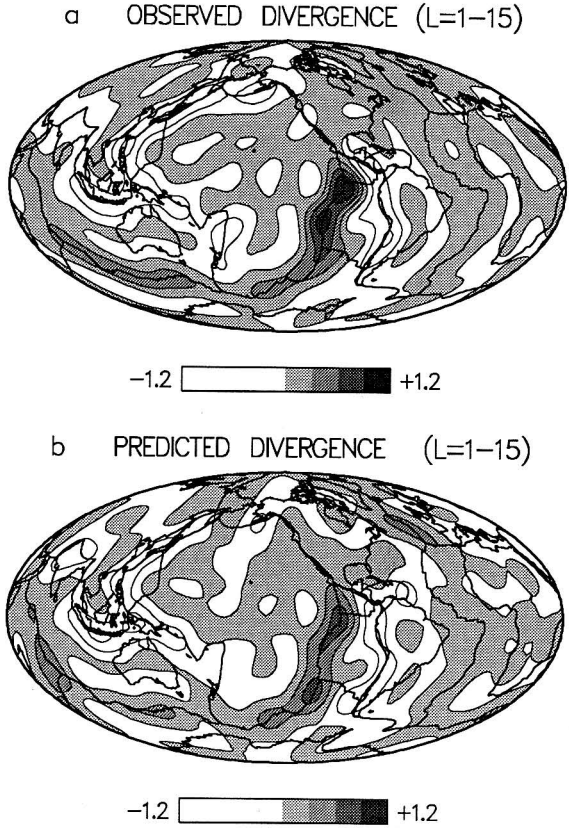

FIG. 10. (a, c) The horizontal divergence (in the range $\ell = 1-15$) and the radial vorticity (in the range $\ell = 2-15$) of the observed plate velocities. These two fields were previously shown (up to $\ell = 32$) in Fig. 5. (b, d) The horizontal divergence (in the range $\ell = 1-15$) and the radial vorticity (in the range $\ell = 2-15$) predicted with model SH8/WM13, using the $\delta \ln \rho / \delta \ln v_s$ values in Fig. 6 and the divergence kernels in Fig. 7. In the calculation of the predicted plate-like surface motions, according to Eqs. (27), (28), and (34), the reference viscosity value $\eta_0 = 10^{21}$ Pa s was employed. In all maps, the units on the scale bars are rad/(10 Myr).

value of 20.0×10^{21} Pa s at 2500-km depth). It is interesting to note that the inferred value of the upper mantle viscosity and the viscosity at the top of the lower mantle are fully compatible with the values previously deduced on the basis of the analysis of postglacial rebound data (Peltier, 1982, 1989).

We may now obtain the buoyancy-induced radial vorticity of the plates from the predicted surface divergence, in Fig. 10b, by employing the coupling matrix (calculated to degree and order 15) in Eqs. (34) and (35). The resulting plate-like

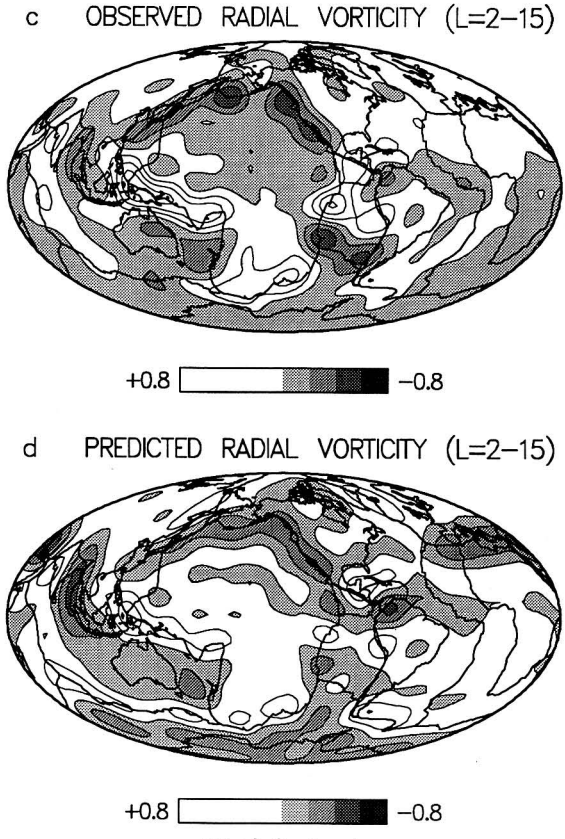

FIG. 10. Continued.

radial vorticity predictions are shown in Fig. 10d along with the radial vorticity of the observed plate motions in Fig. 10c. The agreement between the two maps is fairly good, and the predicted vorticity in Fig. 10d accounts for 38% of the variance of the observed radial vorticity in Figure 10c. The observed plate motions, in Figs. 10a and 10c, as well as the elements of the projection operators, in Eqs. (29) and (34), have been smoothed by the Lanczos factors, in Eq. (19) for which we select the values $L = M = 32$. In Fig. 11 we provide a detailed degree-by-degree comparison of the predicted plate-like surface divergence and the observed plate divergence. Here we also compare the predictions obtained for a mantle without surface plates, calculated according to Eq. (25) in which $\eta_0 = 10^{21}$ Pa s. It is clear from Fig. 11 that the interaction of the long wavelength mantle flow, driven by the seismically inferred density contrasts, with the surface plates

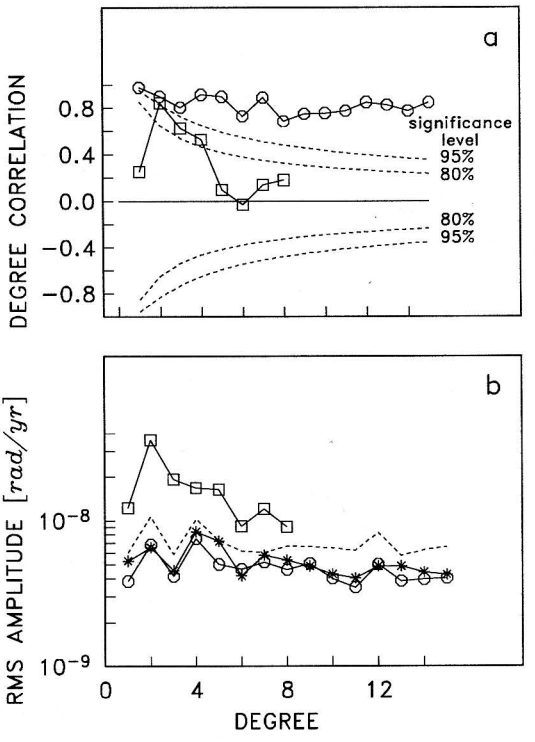

FIG. 11. (a) The cross-correlation, at each degree ℓ, between the observed long-wavelength plate divergence (shown in Fig. 10a) and: the buoyancy-induced surface divergence in the absence of surface plates (□, "no plates") (calculated with model SH8/WM13, using $\delta \ln \rho / \delta \ln v_s$ in Fig. 6, and the divergence kernels in Fig. 7), the predicted plate-like divergence in Fig. 10b (○, "with plates"). (b) The rms amplitude, at each degree ℓ, of the observed long-wavelength plate, divergence (*, "observed"), of the buoyancy-induced surface divergence in the absence of plates (□, "no plates"), and of the plate-like surface divergence (○, "with plates") calculated on the basis of a harmonic expansion of the plates up to degree 32. The dashed line instead represents the plate-like divergence when the plate expansion is limited to degree 15. Units are rad/yr.

does indeed yield a predicted surface divergence that agrees closely with the observed plate divergence. In Fig. 12 we also show a degree-by-degree comparison of the predicted plate-like radial vorticity and the radial vorticity of the observed plate motions.

A good illustration of the nonuniqueness inherent in the interpretation of surface plate motions was provided in Fig. 8. In Fig. 8b we observed that, despite the presence of substantial (degree 2) density heterogeneity in the mantle, the resulting plate motions were essentially zero. In Fig. 8c we also observed that very long-wavelength density heterogeneity could produce realistic plate motions on much

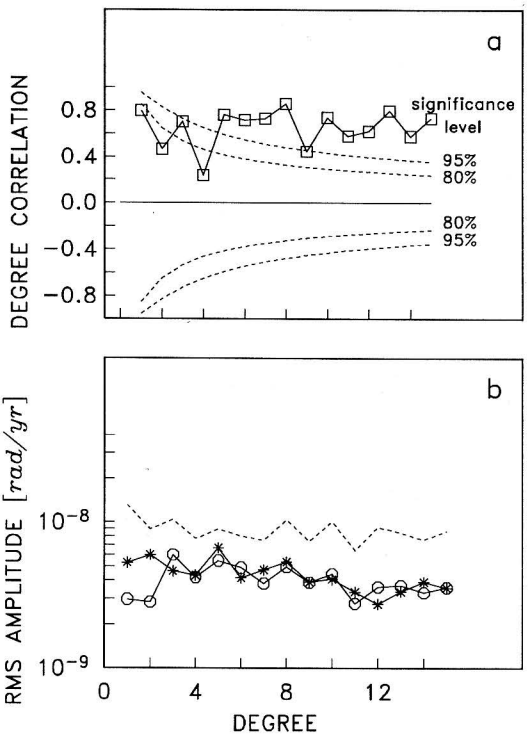

FIG. 12. (a) The cross-correlation, at each degree ℓ, between the observed long-wavelength radial vorticity of the plate velocities (shown in Fig. 10c) and the predicted plate-like radial vorticity in Fig. 10d. (b) The rms amplitude, at each degree ℓ, of the observed radial vorticity of the plate velocities (*, "observed") and of the predicted plate-like radial vorticity (○, "predicted") calculated on the basis of a harmonic expansion of the plates up to degree 32. The dashed line instead represents the plate-like vorticity when the plate expansion is limited to degree 15. Units are rad/yr.

smaller horizontal-length scales. Such results are, of course, completely different from those expected for a mantle without surface plates.

A further illustration of the nonunique interpretation of plate motions is provided by considering two extreme situations in which the density contrasts in the mantle either exist only beneath the midocean ridges or only beneath subduction zones. In Fig. 13a we show the model of midocean ridge heterogeneity constructed from a spherical harmonic expansion (up to degree and order 32) of the four major midocean ridge systems. In Fig. 13b we show the model of slab heterogeneity constructed by Su and Dziewonski (1992) from a spherical harmonic expansion (up to degree and order 50) of International Seismological Center-determined hypocenters in the depth interval 150–250 km. To each model of density heterogeneity in the mantle, we shall apply the plate-projection operator

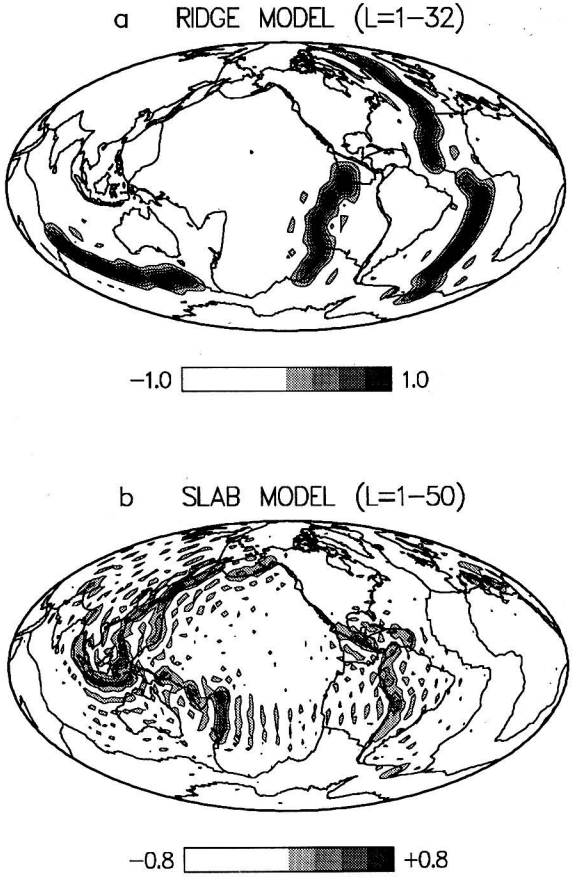

FIG. 13. (a) A model of midocean ridge heterogeneity (in the degree range $\ell = 1-32$) constructed on the basis of a $5° \times 5°$ discretization of the Earth's surface. The heterogeneity pattern is defined by assigning a value of 1 to any $5° \times 5°$ element that coincides with a midocean ridge and a value of 0 elsewhere. (b) A model of subducted slab heterogeneity (in the degree range $\ell = 1-50$) constructed by Su and Dziewonski (1992) on the basis of a $1° \times 1°$ sampling of the ISC hypocentre locations in the depth interval 150–250 km. The heterogeneity is defined by assigning a value of 1 to any $1° \times 1°$ element occupied by an earthquake hypocenter and a value of 0 elsewhere.

[Eqs. (29) and (30)] employed previously for the plate-motion predictions in Figs. 8c and 10b. The mantle viscosity profile we shall employ is again given by Fig. 6 (left panel), and we choose $\eta_0 = 10^{21}$ Pa s. The ridge–slab heterogeneity in Fig. 13 is assumed to extend vertically downward to a depth (chosen arbitrarily) of 1500 km.

In Fig. 14b we now show the predicted plate divergence for the slab-heterogeneity model, in which we maximize the least-squares fit to the observed

plate divergence in Fig. 14a by selecting the optimum density contrast for the slabs (treating all slabs equally) in Fig. 13b. The density contrast we thus find is 0.10 Mg/m^3, and the predicted divergence field in Fig. 14b accounts for 62% of the variance in the observed divergence field in Fig. 14a. It is rather evident from these two figures that the slab-heterogeneity model by itself substantially underpredicts the rate of plate divergence along the East Pacific rise.

In Fig. 14c we show the plate divergence predicted for the ridge-heterogeneity model, in which we again maximize the least-squares fit to the observed plate divergence by assigning optimal density contrasts to each of the four ridges in Fig. 13a. The density contrasts so obtained are -0.010 Mg/m^3 for the North Atlantic ridge heterogeneity, -0.011 Mg/m^3 for the South Atlantic ridge, -0.020 Mg/m^3 for the Southeast Indian ridge, and -0.032 Mg/m^3 for the East Pacific ridge. The predicted divergence field in Fig. 14c accounts for 77% of the variance of the observed field in Fig. 14a. It is noteworthy that the ridge heterogeneity model predicts a realistic pattern of convergence in the west Pacific trench system, and in the Peru–Chile trench system, with an amplitude that is about 60% of that observed in Fig. 14a. A naive interpretation of these simulated trench convergence rates may lead to the conclusion that considerable subducted slab heterogeneity exists in the mantle when, in fact, there is none in this idealized mantle-heterogeneity model.

Finally in Fig. 14d we show the plate divergence predicted for a combined slab–ridge-heterogeneity model, in which we maximize the fit to the observed divergence by selecting optimal density contrasts for the slabs and ridges in Fig. 13. In this case we infer a slab density contrast of 0.063 Mg/m^3, a North Atlantic ridge contrast of -0.004 Mg/m^3, a South Atlantic ridge contrast of -0.006 Mg/m^3, a Southeast Indian ridge contrast of -0.012 Mg/m^3, and an East-Pacific ridge contrast of -0.024 Mg/m^3. It is interesting that the inferred slab density contrast agrees closely with that independently inferred by Hager and O'Connell (1981) and by Hager and Richards (1989) in separate analyses of plate motions and the geoid. The predicted divergence field in Fig. 14d now accounts for 92% of the variance of the observed field in Fig. 14a. This analysis strongly suggests that both the positive density heterogeneity beneath trenches and the negative density heterogeneity beneath ridges contribute significantly to the observed motion of the plates. The ridges therefore appear to be active regions of forcing.

2.3. An Assessment

The cornerstone of previously published treatments of buoyancy-induced plate motions (e.g., Hager and O'Connell, 1981; Ricard and Vigny, 1989; Gable *et al.*, 1991; Forte and Peltier, 1991a,b), including that presented above, is the assumption that the long-term behavior of tectonic plates is that of rigid bodies. Although

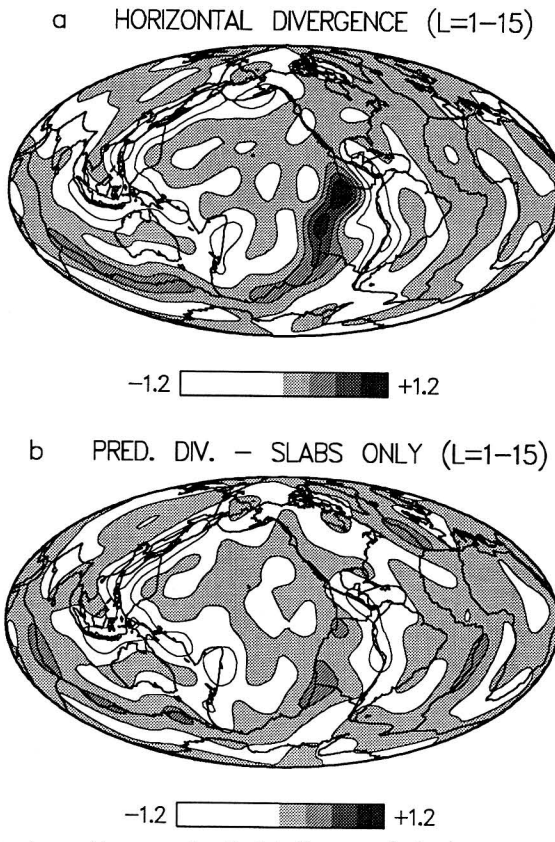

FIG. 14. (a) The observed long-wavelength plate divergence in the degree range $\ell = 1-15$. (b) The plate-like divergence (in the range $\ell = 1-15$) predicted with a best-fitting model of subducted slab heterogeneity (see text for details). (c) The plate-like divergence predicted with a best-fitting model of midocean ridge heterogeneity (see text for details). (d) The plate-like divergence predicted with a best-fitting model of combined slab and ridge heterogeneity. In all predictions the divergence kernels in Fig. 7 are employed and the reference viscosity value is $\eta_0 = 10^{21}$ Pa s. The units on all scale bars are rad/(10 Myr).

this assumption appears to simplify matters, so that the motion of each plate may be specified with only three parameters (the components of its angular-velocity vector), it can also lead to serious inconsistencies when matching the plate motions to the buoyancy-driven flow in the mantle. A precise mathematical description of large-scale flow in a spherically symmetric mantle may be achieved with a limited number of spherical harmonic basis functions, whereas an infinite number of harmonics are required for a precise mathematical description of rigid plate motion. This distinction presents obvious difficulties when modeling plate motions in the spectral domain.

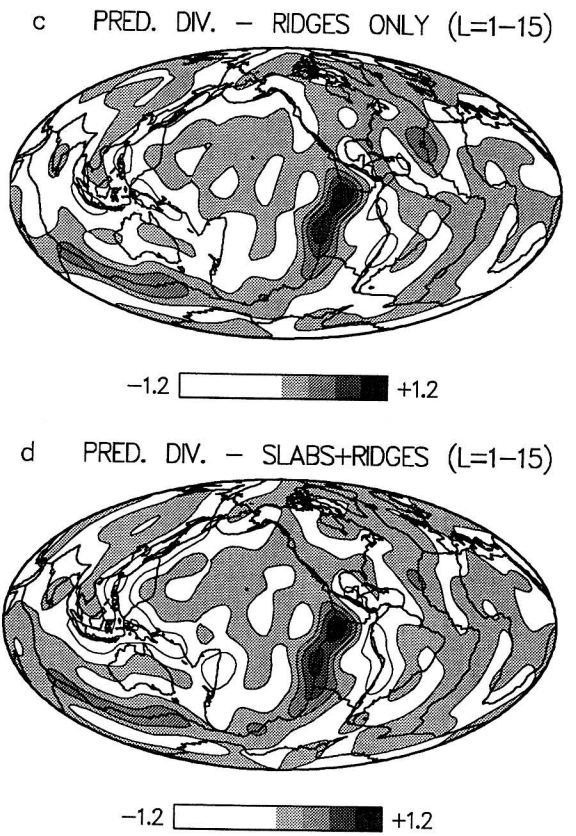

FIG. 14. Continued.

These difficulties are clearly manifested in the spectral-domain treatment of plate motions by Hager and O'Connell (1981). Their treatment in essence consists of two separate calculations: (1) plate velocities are imposed at the surface and the surface-shear-driven flow in the mantle is calculated, and (2) the assumed density perturbations in the mantle excite a flow that is calculated with a no-slip surface boundary condition. Dynamical consistency is assumed if the surface shear stresses, generated in (1), balance the buoyancy-induced surface shear stresses generated in (2). Problems arise because the surface shear stresses in (1) become unbounded as the number of terms retained in the harmonic description of the plates increases indefinitely (see Fig. 3 in Hager and O'Connell, 1981). Infinitely large stresses are required to move a surface layer composed of perfectly rigid contiguous plates. Such infinite stresses cannot be matched to the surface stresses in (2), which always remain finite. Hager and O'Connell (1981) suggest that this inconsistency is resolved by simply postulating that the lithosphere fails

at some critical yield stress. This failure criterion is used, however, only in a separate evaluation of net force exerted on the plates. The impact of this failure on the underlying mantle flow is never determined.

The treatment of plate motions by Ricard and Vigny (1989) is also formulated in the spectral domain and is a modification of the two-step approach proposed by Hager and O'Connell (1981). Ricard and Vigny solve for the set of plate angular-velocity vectors that provide a balance between the surface stresses generated by the plate-driven mantle flow and by the buoyancy-driven flow acting on a no-slip surface boundary. The key assumption employed in this balancing of stresses, is that the forces acting on the plate boundaries are presumed to be identically zero. This assumption is clearly at odds, however, with the actual state of stress at the surface. The surface stresses generated by the plate-driven mantle flow must again become infinite as the number of harmonics that describe the plates increase indefinitely.

The generation of unbounded surface stresses is the inevitable consequence of a procedure that models the mantle flow driven by prescribed plate velocities. To avoid this difficulty we proposed the alternative treatment described in Section 2.2. In this treatment the observable plate motions are generated by the subset of internal buoyancy sources, described in Eq. (30), which interact with a free-slip (i.e., zero-stress) surface. The only surface stresses that are generated are those due to the buoyancy sources in Eq. (31), which interact with a no-slip surface. These surface stresses always remain finite. It is important to appreciate, however, that the fraction of internal buoyancy sources that generates the plate motions becomes increasingly smaller as the number of harmonics used to describe the plates increases. This is understood by noting that the buoyancy sources that produce observable plate motions must be located in the vicinity of the plate boundaries. As these boundaries become narrower (with the increasing resolution of the plates themselves), so does the distribution of effective buoyancy sources. In the limit in which the plate boundaries are infinitely narrow, the plate-driving buoyancy sources in Eq. (30) vanish entirely. This limit is achieved when the number of harmonics used to describe the plates is infinite.

We can illustrate this important point by calculating the plate-projection operator, in Eq. (29), using a spherical harmonic expression of the plates that is limited to degree 15. This limited representation is less plate-like, and characterized by effectively wider plate boundaries, than is a plate representation that includes harmonics up to degree 32 (as in Figs. 5 and 10). We therefore expect that the buoyancy-induced surface motions will possess significantly greater amplitudes. This is confirmed in Figs. 11 and 12, in which the dashed lines represent the rms amplitude of the surface divergence and vorticity predicted on the basis of a harmonic expansion of the plates that is limited to degree 15.

The maximum degree to be retained in a spherical harmonic expansion of the plates depends on the actual rigidity of the tectonic plates. Real plate boundaries

must have a finite region of weakness, or else they could not accommodate the deformations arising from their relative motions. This region of weakness along the edges of the plates may be simulated by truncating the spherical harmonic expansion of the plates. The effective width of the region of weakness, in a harmonic expansion limited to degree 32, is shown by the width of nonzero divergence rates in Fig. 5a. The choice of maximum harmonic degree is, of course, arbitrary, unless we have *a priori* data concerning the mechanical strength of plate boundaries. Such data would permit the determination of the actual lateral variations of rheology in the lithosphere.

3. Lateral Viscosity Variations in the Lithosphere

The technique for calculating surface plate motions, described in Section 2, is evidently rather convenient as it allows us to avoid dealing explicitly with the lateral variations of effective viscosity that characterize the plate-like structure of the lithosphere. This technique is, however, essentially kinematic because the plates are introduced only as a surface boundary constraint on the permitted surface flows. The dynamical details of the flow processes in the lithosphere that mediate the coupling of the surface poloidal and toroidal motions is never determined and remains unknown. A dynamically consistent treatment of the lithosphere requires that we return to the original problem of explicitly treating the effects of lateral variations of effective viscosity in the lithosphere. In this section we shall directly show that the observed toroidal plate motions, and their coupling to poloidal motions, may be understood to first order in terms of plausible lateral variations of viscosity in the lithosphere itself.

The term *viscosity,* when applied to the lithosphere (or the mantle), must be understood in the context of a steady-state rheology of a creeping polycrystalline solid. As discussed in the Introduction (Section 1), the steady-state creep of any crystalline material may be characterized in terms of an *effective* viscosity. This concept of effective viscosity also applies to highly nonlinear materials characterized by stress- or strain-induced softening [see Eq. (3)]. The lateral variations of viscosity in the lithosphere, which will be investigated in this section, should therefore be regarded as an effective physical representation of a possibly nonlinear rheology.

3.1. Theory

The equation of momentum conservation governing quasistatic flow in a continuum with heterogeneous viscosity is given by Eq. (IV.9) in Appendix IV. The coupled scalar expressions that describe the buoyancy-induced poloidal and toroi-

dal flows in such a medium are given by Eqs. (IV.10) and (IV.11). An inspection of these equations immediately reveals that a direct solution, for an arbitrary field of viscosity variations, will be rather difficult. This difficulty might reasonably be circumvented, in the case of the Earth's mantle, by initially assuming that the lateral variations of effective viscosity in the lithosphere are much stronger than in the underlying mantle. To the extent that this assumption is reasonable we may then treat the sublithospheric mantle as a region in which the lateral variations of viscosity may be ignored. As we show below, this assumption allows us to effectively replace the direct solution of Eq. (IV.9) by an equivalent treatment based on the matching of stresses at the two bounding surfaces that define the lithospheric layer. Since the thickness of the Earth's lithosphere ($\approx$100 km) is much less than the radius of the solid upper surface (r = 6368 km), we may employ a locally valid Taylor expansion for the lithospheric flow field.

By virtue of the *tangent-vector theorem* (Backus, 1967) we may write the horizontal component of the lithospheric flow $\mathbf{u}_H$ in the form

$$\frac{\mathbf{u}_H(r,\,\theta,\,\phi)}{r} = \frac{1}{a}\,[\nabla_1 V(r,\,\theta,\,\phi) + \Lambda W(r,\,\theta,\,\phi)]. \tag{36}$$

If we expand the scalars V and W as a Taylor series in r and retain the lowest-order terms, we obtain

$$V(r,\,\theta,\,\phi) \approx V_0(\theta,\,\phi) + \frac{(r-a)}{a}\,V_1(\theta,\,\phi) + \frac{(r-a)^2}{2a^2}\,V_2(\theta,\,\phi), \tag{37}$$

$$W(r,\,\theta,\,\phi) \approx W_0(\theta,\,\phi) + \frac{(r-a)}{a}\,W_1(\theta,\,\phi) + \frac{(r-a)^2}{2a^2}\,W_2(\theta,\,\phi), \tag{38}$$

where $r = a$ (= 6368 km) is the radius of the solid outer surface. The application of the free-slip (zero tangential stress) boundary condition at the outer surface

$$\frac{\partial}{\partial r}\left[\frac{\mathbf{u}_H}{r}\right]_{r=a} = 0, \tag{39}$$

implies that

$$V_1(\theta,\,\phi) = W_1(\theta,\,\phi) = 0. \tag{40}$$

The radial component $u_r(r,\,\theta,\,\phi)$ of the lithospheric flow may be determined from the equation of mass conservation $\nabla \cdot \mathbf{u} = 0$ for an incompressible lithosphere:

$$\frac{1}{r^2}\frac{\partial}{\partial r}\,r^2 u_r = -\frac{1}{r}\,\nabla_1 \cdot \mathbf{u}_H. \tag{41}$$

By substituting Eq. (36) into (41), employing results (37), (38), and (40), and finally integrating with respect to radius, we obtain

$$u_r(r, \theta, \phi) = \left(\frac{a^3 - r^3}{3ar^2}\right)\Lambda^2 V_0 + \frac{(a - r)^3}{6a^3r^2} \times \left[r^2 + \frac{r(a - r)}{2} + \frac{(a - r)^2}{10}\right]\Lambda^2 V_2. \tag{42}$$

In obtaining (42) we have also made use of the condition of zero radial velocity, $u_r(r = a, \theta, \phi) = 0$, at the upper bounding surface.

The scalars V_0 and W_0 in Eqs. (37) and (38) may be directly constrained by the observed tectonic plate velocities $\mathbf{v}(\theta, \phi)$. Indeed it is straightforward to verify, using (36)–(38), that

$$\mathbf{v}(\theta, \phi) = \nabla_1 V_0(\theta, \phi) + \Lambda W_0(\theta, \phi). \tag{43}$$

The scalars V_2 and W_2 in Eqs. (37) and (38) may be related to the known scalars V_0 and W_0 in (43) by substituting expressions (36) and (42) into Eqs. (IV.9) and (IV.10) and "solving" for V_2 and W_2. Apart from the ensuing mathematical difficulties, such an approach requires that we already know the lateral variations of effective viscosity of the lithosphere. Unfortunately we do not possess, *a priori,* a sufficiently complete or realistic description of the rheology of the lithosphere. Another method for determining the values of V_2 and W_2 involves matching the buoyancy-induced normal stress from the mantle flow to the normal stresses generated by the lithospheric flow field in Eqs. (36) and (42). This method, quite apart from requiring a knowledge of the buoyancy forces in the mantle itself, again requires that we know the lateral variations of viscosity in the lithosphere. This is unsatisfactory because we wish to discover the nature of these lateral variations in the first place.

To overcome these difficulties we shall make the following simplifying "quasirigid lithosphere" approximation:

$$\mathbf{u}_H(r = r_L, \theta, \phi) = c\ \mathbf{u}_H(r = a, \theta, \phi) \tag{44}$$

in which $r = r_L$ is the radius defining the lower bounding surface of the lithosphere and c is some as yet undetermined constant. By invoking (44) we are in effect assuming that the tangential flow velocities at the base of the lithosphere are parallel to those at the surface; hence the term *quasirigid.* Equation (44) implies that

$$V_2(\theta, \phi) = KV_0(\theta, \phi) \quad \text{and} \quad W_2(\theta, \phi) = KW_0(\theta, \phi), \tag{45}$$

in which K is a constant. We again emphasize that the quasirigid assumption, and the consequent appearance of the scalar K in Eq. (45), is introduced because of our lack of knowledge concerning the lateral variations of effective viscosity in the lithosphere. The ultimate validity of the approximation in Eq. (45) may be judged by the inferences of these lateral viscosity variations, presented in Section 3.3 below.

We may attempt to estimate the magnitude of the constant K by matching the dynamic surface topography, expected on the basis of the lithospheric flow in (36) and (42), with the dynamic surface topography estimated by isostatic reduction (Forte *et al.*, 1993a) of the observed topography. From Eq. (A18) in Forte and Peltier (1987) we have

$$(\delta a)^m_\ell = \frac{1}{\Delta\rho_{m0}} \frac{\eta_L}{g_0} \left[-r \frac{d^3}{dr^3} + \frac{3\ell(\ell+1)}{r} \frac{d}{dr} \right]_{r=a} p^m_\ell(r), \tag{46}$$

in which $(\delta a)^m_\ell$ is the spherical harmonic coefficient of the dynamic surface topography, $\Delta\rho_{mo}$ is the density jump across the lithosphere–ocean boundary, and $p^m_\ell(r)$ is the poloidal generating scalar that describes the lithospheric flow field. The radial velocity in (42) is directly related to the poloidal-flow scalar by $u_r = \Lambda^2 p/r$ and therefore

$$p(r, \theta, \phi) = \left\{ \left(\frac{a^3 - r^3}{3ar} \right) + K \frac{(a-r)^3}{6a^3 r} \times \left(r^2 + \frac{r(a-r)}{2} + \frac{(a-r)^2}{10} \right) \right\} V_0(\theta, \phi). \tag{47}$$

The scalar $V_0(\theta, \phi)$ may be related to the surface horizontal divergence of the lithospheric flow field and, on the basis of Eq. (43), we have

$$\nabla_H \cdot \mathbf{v} = \frac{\Lambda^2}{a} V_0. \tag{48}$$

We similarly have the following relationship between the scalar $W_0(\theta, \phi)$ and the radial vorticity of the lithospheric flow field:

$$\hat{\mathbf{r}} \cdot \nabla \times \mathbf{v} = \frac{\Lambda^2}{a} W_0. \tag{49}$$

Combining expressions (47) and (48) with Eq. (46) we finally obtain

$$\frac{\Delta\rho_{mo} g_0 \delta a^m_\ell}{\eta_L} = \left[3 - \frac{(2+K)}{\ell(\ell+1)} \right] (\nabla_H \cdot \mathbf{v})^m_\ell. \tag{50}$$

The isostatically reduced surface topography (Forte *et al.*, 1993a) is most strongly correlated with the observed plate divergence at harmonic degrees 3 and 4. The rms amplitude of the isostatically reduced surface topography, at degrees $\ell = 3$ and 4, is respectively 0.3 and 0.5 km. The rms amplitude of the horizontal divergence of the observed plate velocities, at degrees $\ell = 3$ and 4, is respectively 0.46×10^{-8} and 0.86×10^{-8} rad/yr. We find that Eq. (50) may be satisfied at degrees 3 and 4 by the following selection of K and η_L values:

$$\begin{aligned} K &= 0 \rightarrow \eta_L \approx 15 \times 10^{21} \text{ Pa s} \\ K &= -20 \rightarrow \eta_L \approx 10 \times 10^{21} \text{ Pa s} \\ K &= -40 \rightarrow \eta_L \approx 8 \times 10^{21} \text{ Pa s} \\ K &= -60 \rightarrow \eta_L \approx 6 \times 10^{21} \text{ Pa s} \end{aligned} \tag{51}$$

We have obviously not presented a complete list of (K, η_L) values in (51), but it is nonetheless clear that a large range of K values corresponds to a much smaller variation of η_L values. We do not possess reliable estimates of the absolute, spherically averaged, effective viscosity of the lithosphere and, given the very rough approximation represented by Eq. (50), we cannot use (51) to reliably distinguish which K value is most appropriate. We defer the selection of appropriate K values to Section 3.3 below.

The locally valid expression which describes the lithospheric flow is thus obtained by combining Eqs. (36)–(38), (40), (42), and (45) to obtain

$$\begin{aligned} \mathbf{u}(r, \theta, \phi) = \hat{\boldsymbol{r}} &\left[\frac{a^3 - r^3}{3ar^2} + K \frac{(a-r)^3}{6a^3r^2} \left(r^2 + \frac{r(a-r)}{2} + \frac{(a-r)^2}{10} \right) \right] \\ &\times \Lambda^2 V_0 + \frac{r}{a} \left(1 + K \frac{(r-a)^2}{2a^2} \right) [\nabla_1 V_0 + \boldsymbol{\Lambda} W_0]. \end{aligned} \tag{52}$$

We may now consider how expression (52) may ultimately be employed, in conjunction with the condition of stress continuity across the lithosphere–mantle boundary, to constrain the possible lateral variations of the effective viscosity in the lithosphere.

As shown in Appendix V [Eq. (V.9)], the continuity of horizontal stress across the lithosphere–mantle interface implies that

$$\eta_L(\theta, \phi) \left[\nabla_H u_r + r \frac{\partial}{\partial r} \left(\frac{\mathbf{u}_H}{r} \right) \right]_{r=r_L^+} = \eta_M \left[\nabla_H u_r + r \frac{\partial}{\partial r} \left(\frac{\mathbf{u}_H}{r} \right) \right]_{r=r_L^-}, \tag{53}$$

in which $\eta_L(\theta, \phi)$ is the field of lateral viscosity variations in the lithosphere and η_M is the viscosity of the sublithospheric mantle, which is assumed to be spherically symmetric. We shall find it advantageous to consider the toroidal component of the horizontal stress matching, obtained by applying the operator $\boldsymbol{\Lambda} \cdot$ to both sides of (53):

$$\begin{aligned} \boldsymbol{\Lambda}\eta_L \cdot \left[\nabla_H u_r + r \frac{\partial}{\partial r} \left(\frac{\mathbf{u}_H}{r} \right) \right]_{r=r_L^+} + \eta_L \left[r \frac{\partial}{\partial r} \left(\frac{\boldsymbol{\Lambda} \cdot \mathbf{u}_H}{r} \right) \right]_{r=r_L^+} \\ = \eta_M \left[r \frac{\partial}{\partial r} \left(\frac{\boldsymbol{\Lambda} \cdot \mathbf{u}_H}{r} \right) \right]_{r=r_L^-}. \end{aligned} \tag{54}$$

In Eq. (54) we now substitute the lithospheric flow field given by Eq. (52) and, after some manipulation, obtain

$$\varepsilon \mathbf{\Lambda} \nu_L \cdot [\nabla_1(\Lambda^2 - K)V_0 - K\mathbf{\Lambda}W_0] - \varepsilon(1 + \nu_L)K\Lambda^2 W_0 = \frac{\eta_M}{\langle \eta_L \rangle} r_L^2 \left[\frac{\partial}{\partial r} \left(\frac{\Lambda^2 q}{r} \right) \right]_{r=r_L^-}, \quad (55)$$

in which $\varepsilon = h/a$, where h is the thickness of the lithosphere, $\langle \eta_L \rangle$ is the average lithospheric viscosity and is given by the $\ell = 0$, $m = 0$ coefficient of the spherical harmonic decomposition of $\eta_L(\theta, \phi)$, $\nu_L(\theta, \phi)$ is the dimensionless departure of the lithospheric viscosity from its average value defined according to

$$\eta_L(\theta, \phi) = \langle \eta_L \rangle [1 + \nu_L(\theta, \phi)], \quad (56)$$

and $q(r, \theta, \phi)$ is the scalar field defining the sublithospheric toroidal flow as follows:

$$\mathbf{u}_{\text{tor}}(r, \theta, \phi) = \mathbf{\Lambda} q(r, \theta, \phi). \quad (57)$$

In the derivation of Eq. (55) we have neglected all terms of order ε^2 and smaller. The quantity $\varepsilon \nu_L = \varepsilon(\eta_L / \langle \eta_L \rangle - 1)$ is analogous to the "stiffness" parameter employed by Ribe (1992). The term $\Lambda^2 V_0$ that appears on the left-hand side of Eq. (55) arises from radial velocity u_r in the lithosphere, given by expression (52). This term is clearly not negligible and indeed becomes increasingly dominant with decreasing horizontal wavelength (i.e., as the spherical harmonic degree ℓ increases). We emphasize this point because the treatment of lithosphere–mantle coupling by Ricard *et al.* (1988), employed again in Ricard *et al.* (1991), assumes that the contribution to the horizontal stress by u_r is negligible. Equation (55) demonstrates that this assumption is not valid.

The mathematical advantage of assuming a spherically symmetric viscosity in the sublithospheric mantle is most apparent when treating the dynamics of toroidal flow in this region. Indeed, if we assume for simplicity that the mantle consists of two constant viscosity layers (e.g., the upper and lower mantle) the equation governing the toroidal flow in each layer is, according to Eq. (IV.11) in Appendix IV

$$\nabla^2 \Lambda^2 q = 0, \quad (58)$$

in which we have employed Eq. (57). This simple equation demonstrates that there are no internal sources of toroidal flow in a medium with spherically symmetric viscosity. The toroidal flow in the mantle will therefore be identically zero (except at degree $\ell = 1$; see below) unless there are inhomogeneous boundary conditions. In Eq. (55) we have an important example of such an inhomogeneous boundary condition. Here we observe that the presence of a lithosphere with lateral viscosity variations gives rise to horizontal shear stresses that drive toroidal flow in the sublithospheric mantle.

The solution to Eq. (58) is readily obtained if we expand $q(r, \theta, \phi)$ in terms of spherical harmonic basis functions. We thus find that the spherical harmonic coefficients $q_\ell^m(r)$ satisfy the following equation:

$$\left[\frac{d^2}{dr^2} + \frac{2}{r}\frac{d}{dr} - \frac{\ell(\ell+1)}{r^2}\right] q_\ell^m(r) = 0. \tag{59}$$

The solution of Eq. (59) is of the form

$$q_\ell^m(r) = E_\ell^m r^\ell + \frac{F_\ell^m}{r^{\ell+1}}, \tag{60}$$

in which the constants E_ℓ^m and F_ℓ^m are determined by the boundary conditions in our problem. In our simplified mantle, consisting of two constant-viscosity layers, the boundary condition at the core–mantle boundary $r = b$ is

$$\frac{d}{dr}\left(\frac{q_\ell^m}{r}\right)_{r=b} = 0, \tag{61}$$

valid for a free-slip boundary. At $r = d$, the surface that defines the horizon between the two mantle layers, we have the following boundary conditions that express the continuity of velocity and stress:

$$q_\ell^m(r = d^+) = q_\ell^m(r = d^-), \tag{62}$$

$$\eta_+ \frac{d}{dr}\left(\frac{q_\ell^m}{r}\right)_{r=d^+} = \eta_- \frac{d}{dr}\left(\frac{q_\ell^m}{r}\right)_{r=d^-}, \tag{63}$$

in which η_+ [$= \eta_M$ in Eqs. (53)–(55)] is the upper-layer viscosity and η_- is the lower-layer viscosity. Equation (55) provides the remaining boundary condition

$$\frac{d}{dr}\left(\frac{q_\ell^m}{r}\right)_{r=r_L^-} = -\frac{\langle\eta_L\rangle}{\eta_M}\frac{T_\ell^m}{r_L^2\ell(\ell+1)}, \tag{64}$$

in which T_ℓ^m is the spherical harmonic coefficient in the harmonic expansion of the left-hand side of Eq. (55):

$$T_\ell^m = \frac{1}{4\pi}\int\int Y_\ell^{m*}\{\varepsilon\mathbf{\Lambda}\nu_L \cdot [\nabla_1(\Lambda^2 - K)V_0 - K\mathbf{\Lambda}W_0] - \varepsilon(1+\nu_L)K\Lambda^2 W_0\}\sin\theta\, d\theta\, d\phi. \tag{65}$$

The normalization convention we employ for the Y_ℓ^m throughout this chapter is given by Eq. (II.3) in Appendix II. We shall omit the algebraic details involved in determining the constants E_ℓ^m, F_ℓ^m that satisfy conditions (61)–(64) and simply point out that the values of $(E_+)_\ell^m$ and $(F_+)_\ell^m$, which define the toroidal flow in the upper layer of the mantle, are given by

$$(E_+)_\ell^m = -\frac{\langle \eta_L \rangle}{\eta_M} \frac{T_\ell^m}{r_L^\ell \ell(\ell+1)(\ell-1)} \frac{B_\ell}{[B_\ell - (\ell+2)(d/r_L)^{2\ell+1} A_\ell]} \tag{66}$$

$$(F_+)_\ell^m = -\frac{\langle \eta_L \rangle}{\eta_M} \frac{T_\ell^m}{r_L^\ell \ell(\ell+1)} \frac{d^{2\ell+1} A_\ell}{[B_\ell - (\ell+2)(d/r_L)^{2\ell+1} A_\ell]}, \tag{67}$$

where

$$A_\ell = (1-\gamma) + (b/d)^{2\ell+1}\left(\frac{\ell-1}{\ell+2} + \gamma\right) \tag{68}$$

$$B_\ell = (\ell+2) + \gamma(\ell-1) + (\ell-1)(b/d)^{2\ell+1}(1-\gamma), \tag{69}$$

in which $\gamma = \eta_-/\eta_+$. Employing expressions (66) and (67) we then find that value of the toroidal-flow scalar, immediately below the lithosphere–mantle interface, is given by

$$q_\ell^m(r_L^-) = -\frac{\langle \eta_L \rangle}{\eta_M} \frac{T_\ell^m}{\ell(\ell+1)(\ell-1)} \frac{[B_\ell + (\ell-1)(d/r_L)^{2\ell+1} A_\ell]}{[B_\ell - (\ell+2)(d/r_L)^{2\ell+1} A_\ell]}. \tag{70}$$

It is straightforward to show, on the basis of expressions (68) and (69), that when the viscosity of the lower layer is much greater than that of the upper layer ($\gamma \gg 1$), Eq. (70) reduces to the following expression:

$$q_\ell^m(r_L^-) \approx -\frac{\langle \eta_L \rangle}{\eta_M} \frac{T_\ell^m}{\ell(\ell+1)} \frac{[1 - (d/r_L)^{2\ell+1}]}{[(\ell-1) + (\ell+2)(d/r_L)^{2\ell+1}]}. \tag{71}$$

Equation (71) will be exactly true for a perfectly rigid lower mantle, which thus appears as a no-slip lower boundary (except at $\ell = 1$; see below) for the upper-layer toroidal flow.

The requirement that tangential shear stresses be finite at the lithosphere–mantle interface implies that the tangential flow velocity must be continuous and therefore

$$(\mathbf{\Lambda} \cdot \mathbf{u}_H)_{r=r_L^+} = (\mathbf{\Lambda} \cdot \mathbf{u}_H)_{r=r_L^-}. \tag{72}$$

If we now substitute Eqs. (52) and (57) into Eq. (72) and expand the flow scalars in terms of their spherical harmonic coefficients, we then obtain

$$(1-\varepsilon)(W_0)_\ell^m = q_\ell^m(r_L^-), \tag{73}$$

in which ε is the dimensionless thickness of the lithosphere, introduced in Eq. (55). All terms of order ε^2 and smaller have been omitted from the left-hand side of Eq. (73). For $\varepsilon \ll 1$ we may also safely ignore the term containing ε in (73). Combining Eqs. (70) and (73) we thus obtain

$$-\ell(\ell+1)(\ell-1)\frac{[B_\ell-(\ell+2)(d/r_L)^{2\ell+1}A_\ell]}{[B_\ell+(\ell-1)(d/r_L)^{2\ell+1}A_\ell]}(W_0)_\ell^m=\frac{\langle\eta_L\rangle}{\eta_M}T_\ell^m. \quad (74)$$

It is clear from the defining equation [Eq. (65)] for T_ℓ^m that Eq. (74) describes the coupling that must exist, as a consequence of lateral viscosity variations in the lithosphere, between the toroidal and poloidal components of lithospheric flow. This coupling was obtained on the basis of the continuity of horizontal stress and horizontal velocity at the lithosphere–mantle boundary.

3.2. Net Rotations in the Lithosphere and Mantle

The matching of stresses and velocities at the lithosphere–mantle interface merits additional consideration when dealing with the degree $\ell = 1$ component of toroidal flow in the mantle. The toroidal-flow scalar in the upper and lower mantle layers is given by the expression (60). At $\ell = 1$ the free-slip condition at the core–mantle boundary (CMB), given by Eq. (61), implies that $F_1^m = 0$ in the lower layer and thus $q_1^m(r) = E_1^m r$ in the lower layer. In the upper layer Eq. (60) applies again and, owing to the matching conditions (62) and (63), we again have $q_1^m(r) = E_1^m r$. The degree 1 toroidal flow field throughout the mantle is thus given by the following simple expression:

$$\mathbf{v}_{\text{tor}}(r,\theta,\phi)=\mathbf{\Lambda}\sum_{m=-1}^{+1}rE_1^mY_1^m(\theta,\phi). \quad (75)$$

In Eqs. (5) and (10) we previously showed that a rigid-body rotation may be expressed as

$$\mathbf{v}_{\text{rigid}}(r,\theta,\phi)=\boldsymbol{\omega}\times\mathbf{r}=-\mathbf{\Lambda}\,\Omega, \quad (76)$$

where

$$\Omega=\frac{r}{\sqrt{6}}[(-\omega_x+\imath\omega_y)Y_1^1(\theta,\phi)+\sqrt{2}\omega_zY_1^0(\theta,\phi)+(\omega_x+\imath\omega_y)Y_1^{-1}(\theta,\phi)] \quad (77)$$

is derived in Appendix III. The vector $\boldsymbol{\omega}=\omega_x\hat{\boldsymbol{\imath}}+\omega_y\hat{\boldsymbol{\jmath}}+\omega_z\hat{\mathbf{k}}$ describes the angular velocity of the rigid-body rotation. A comparison of Eq. (75) and Eqs. (76) and (77) shows that the $\ell = 1$ toroidal flow is a rigid-body rotation of the entire mantle. The components of the angular velocity vector that describe this rotation are given by

$$\omega_x=\sqrt{6}\,\text{Re}[E_1^1],\ \omega_y=-\sqrt{6}\,\text{Im}[E_1^1],\ \omega_z=-\sqrt{3}E_1^0. \quad (78)$$

The rigid-body rotation described by Eq. (75) was derived by assuming that the

viscosity in the mantle is spherically symmetric. This motion does not produce any tangential stresses, either within the mantle or at the bounding surfaces. An arbitrary rigid-body rotation of a fluid shell, with free-slip boundaries and spherically symmetric viscosity, is always a possible mode of "flow." We may eliminate this rigid-body motion by transferring to a frame of reference rotating with angular velocity (78) relative to the original frame. Since flow in an infinite Prandtl number fluid (like the mantle) is not influenced by inertial forces, this new frame of reference is dynamically equivalent to the original frame.

Arbitrary rigid-body rotation is a degenerate solution of the viscous flow equations in a spherically symmetric mantle. This degeneracy is eliminated by introducing lateral viscosity variations, in which case the degree $\ell = 1$ toroidal flow will not possess the simple linear dependence on radius in Eq. (75). The $\ell = 1$ toroidal flow field will in general be described by $\mathbf{v}_{\text{tor}} = \mathbf{\Lambda} \Sigma_m E_1^m(r) Y_1^m(\theta, \phi)$, and thus each infinitesimally thick spherical shell at radius r in the mantle will rotate with a different angular velocity given by

$$\omega_x(r) = \frac{\sqrt{6}}{r} \operatorname{Re}[E_1^1(r)],$$

$$\omega_y(r) = -\frac{\sqrt{6}}{r} \operatorname{Im}[E_1^1(r)], \qquad \omega_z(r) = -\frac{\sqrt{3}}{r} E_1^0(r). \tag{79}$$

The differential mantle rotation due to lateral viscosity variations has recently been invoked as an explanation for the net rotation of the lithosphere in absolute-motion plate models based on the hotspot frame of reference (Ricard *et al.,* 1991; O'Connell *et al.,* 1991). The hotspot tracks on the Pacific plate are assumed to arise from a net rotation of the lithosphere relative to the underlying mantle in which the hotspots are presumably "anchored." The analysis by Ricard *et al.* (1991) is based on their use of the following expression for the horizontal shear exerted across the lithospheric layer

$$\mathbf{v}_H(r = a) - \mathbf{v}_H(r = r_L) = h\langle \eta^{-1} \rangle \mathbf{t}_H, \tag{80}$$

in which $\mathbf{v}_H(r = a)$ is the horizontal flow velocity at the Earth's solid surface, $\mathbf{v}_H(r = r_L)$ is the horizontal flow velocity at the lithosphere–mantle interface, $h = a - r_L$ is the thickness of the lithospheric layer, $\langle \eta^{-1} \rangle$ is the depth average of the laterally varying reciprocal viscosity in the lithospheric layer, and $\mathbf{t}_H$ is the horizontal shear stress acting at the solid surface. The lithospheric layer containing the lateral viscosity variations is assumed to be 100 km thick in Ricard *et al.* (1991).

Equation (80) is based on the following general expression for the tangential flow-induced stress [see Eq. (V.7) in Appendix V]:

$$\mathbf{t}_H = \eta \left[\nabla_H u_r + r \frac{\partial}{\partial r} \left(\frac{\mathbf{u}_H}{r} \right) \right]. \tag{81}$$

It is clear from a comparison of Eqs. (80) and (81) that Ricard *et al.* assume that the horizontal gradient of radial velocity u_r is negligible compared to the radial gradient of horizontal velocity. The significant error arising from this assumption was previously pointed out in the discussion immediately following Eq. (57). It is also clear that Ricard *et al.* assume, apparently without justification, that the condition

$$\frac{\partial \mathbf{u}_H}{\partial r} \gg \frac{\mathbf{u}_H}{r} \tag{82}$$

obtains throughout the lithospheric layer.

The greatest problem posed by the differential rotation analysis of Ricard *et al.* (1991) arises from their assumption of a nonvanishing tangential stress $\mathbf{t}_H$ at the solid surface. The existence of such a stress arises from the fact that Ricard *et al.* assume that the lithospheric plate velocities are simply imposed as a boundary condition. Clearly, the imposed plate motions are maintained against viscous dissipation by *externally* applied horizontal stresses. This flow calculation is physically unrealistic. In reality there are no imposed external stresses, and the plate motions must arise from internal flow driven by buoyancy forces. Since there can be no external stresses driving the plates, the boundary condition that must be employed with observable plate motions is clearly free-slip and therefore

$$\mathbf{t}_H(r = a) = 0 \Rightarrow \frac{\partial}{\partial r}\left(\frac{\mathbf{u}_H}{r}\right)_{r=a} = 0. \tag{83}$$

It is evident, on the basis of Eq. (83), that the assumption in Eq. (82) is not valid. The application of Eq. (83) to the near-surface net rotation $\boldsymbol{\omega}(r) \times \mathbf{r}$ implies that

$$\left(\frac{d\boldsymbol{\omega}(r)}{dr}\right)_{r=a} = 0. \tag{84}$$

Equation (84) shows that the differential rotation across a thin lithospheric layer is entirely negligible. In other words, the observed net rotation of the lithosphere will be nearly identical to that at the top of the mantle. Finite differential rotation between the surface and the deep mantle requires that the depth interval in which lateral viscosity variations occur be considerably in excess of the thickness of the lithosphere. Such a differential rotation cannot be described by the theory described in this section; it requires a theory that treats the effects of lateral viscosity variations throughout the mantle (see Section 4 below).

3.3. Inverting for Lateral Viscosity Variations

We now show that the definition (56) of the normalized viscosity perturbations implies that

$$\nu_L(\theta, \phi) \approx O(1). \tag{85}$$

The actual viscosity $\eta_L(\theta, \phi)$ must be positive and therefore $\nu_L(\theta, \phi) > -1$. Since the horizontal average of $\nu_L(\theta, \phi)$ is, by definition, equal to zero, the maximum positive values of $\nu_L(\theta, \phi)$ will in general be of order unity. We may illustrate this point by considering the lithosphere. The plate boundaries may be imagined to be very weak and thus $\nu_L(\theta, \phi) \approx -1$ over the small surface area occupied by plate boundaries. The value of $\nu_L(\theta, \phi)$ must therefore be less than $+1$ in the plate interiors to ensure that the horizontal average of $\nu_L(\theta, \phi)$ is identically zero.

The coefficient of the term $(W_0)_\ell^m$ on the left-hand side of Eq. (74) is $O(1)$, and therefore, from the definition of T_ℓ^m in Eq. (65) and from Eq. (85) we must have

$$\frac{\langle \eta_L \rangle}{\eta_M} \varepsilon \approx O(1), \tag{86}$$

to ensure that both sides of Eq. (74) are balanced. The viscous coupling and generation of toroidal flow in the mantle by lateral viscosity variations in the lithosphere thus implies, according to Eq. (86), that the thickness ε of the lithosphere trades off inversely with its relative "stiffness" $\langle \eta_L \rangle / \eta_M$.

We will find it useful to rewrite Eqs. (74) and (65) as

$$-\ell(\ell+1)\left\{(\ell-1)\frac{[B_\ell - (\ell+2)(d/r_L)^{2\ell+1}A_\ell]}{[B_\ell + (\ell-1)(d/r_L)^{2\ell+1}A_\ell]}\frac{\eta_M}{\langle \eta_L \rangle \varepsilon} + K\right\} \times (W_0)_\ell^m = Q_\ell^m, \tag{87}$$

where

$$Q_\ell^m = \frac{1}{4\pi}\iint Y_\ell^{m*}\{\mathbf{\Lambda}\nu_L \cdot [\nabla_1(\Lambda^2 - K)V_0 - K\mathbf{\Lambda}W_0] - \nu_L K\Lambda^2 W_0\} \times \sin\theta \, d\theta \, d\phi. \tag{88}$$

Prior to obtaining an explicit expression for Q_ℓ^m in terms of the spherical harmonic coefficients of ν_L, V_0, and W_0 we point out that for a general field $f(\theta, \phi) = \Sigma f_\ell^m Y_\ell^m$ the following identities hold:

$$\mathbf{\Lambda} f(\theta, \phi) = \sum_{\ell,m} \iota \left[\frac{\hat{\boldsymbol{e}}_{-1}}{\sqrt{2}} a_\ell^{m-1} f_\ell^{m-1} + \hat{\boldsymbol{e}}_0 m f_\ell^m - \frac{\hat{\boldsymbol{e}}_1}{\sqrt{2}} a_{\bar{\ell}}^{-m-1} f_{\bar{\ell}}^{m+1}\right] Y_\ell^m(\theta, \phi), \tag{89}$$

$$\begin{aligned}\nabla_1 f(\theta, \phi) = \sum_{\ell,m}\Bigg[& \frac{\hat{\boldsymbol{e}}_{-1}}{\sqrt{2}}(f_{\ell-1}^{m-1}(1-\delta_{\ell 0})(\ell-1)c_{\ell-1}^{m-1} + f_{\ell+1}^{m-1}(\ell+2)c_{\bar{\ell}}^{-m}) \\ & - \hat{\boldsymbol{e}}_0(f_{\ell-1}^m(1-\delta_{\ell 0})(\ell-1)b_{\ell-1}^m - f_{\ell+1}^m(\ell+2)b_\ell^m) \\ & + \frac{\hat{\boldsymbol{e}}_1}{\sqrt{2}}(f_{\ell-1}^{m+1}(1-\delta_{\ell 0})(\ell-1)c_{\bar{\ell}-1}^{-m-1} \\ & + f_{\ell+1}^{m+1}(\ell+2)c_\ell^m)\Bigg] Y_\ell^m(\theta, \phi),\end{aligned} \tag{90}$$

in which $\iota = \sqrt{-1}$. Equations (89)–(90) follow from Eqs. (I.8) and (I.12) in Appendix I. Expanding all quantities in (88) in terms of spherical harmonics, i.e.,

$$\nu_L = \sum_{\ell,m} (\nu_L)_\ell^m Y_\ell^m, \qquad V_0 = \sum_{\ell,m} (V_0)_\ell^m Y_\ell^m, \qquad W_0 = \sum_{\ell,m} (W_0)_\ell^m Y_\ell^m,$$

and employing results (89)–(90), we may obtain (algebraic details omitted here) the following:

$$\begin{aligned} Q_\ell^{m*} = \sum_{u,v} (\nu_L)_u^v \Bigg\{ & \sum_{n=|\ell-u|}^{\ell+u} \frac{a_u^v}{2} \begin{bmatrix} m & v+1 & i \\ \ell & u & n \end{bmatrix} (K\, a_n^{-i-1} (W_0)_n^{i+1} \\ & + \iota[(V_0)_{n-1}^{i+1}[(n-1)n + K](1-\delta_{n0})(n-1)c_{n-1}^{-i-1} \\ & + (V_0)_{n+1}^{i+1}[(n+1)(n+2) + K](n+2)c_n^i]) \\ & + \begin{bmatrix} m & v & j \\ \ell & u & n \end{bmatrix} (K\, vj(W_0)_n^j + \iota v[(V_0)_{n-1}^j[(n-1)n + K] \\ & \times (1-\delta_{n0})(n-1)b_{n-1}^j - (V_0)_{n+1}^j[(n+1)(n+2) + K] \\ & \times (n+2)b_n^j] + Kn(n+1)(W_0)_n^j) + \frac{a_u^{-v}}{2} \begin{bmatrix} m & v-1 & k \\ \ell & u & n \end{bmatrix} \\ & \times (Ka_n^{k-1}(W_0)_n^{k-1} - \iota[(V_0)_{n-1}^{k-1}[(n-1)n + K] \\ & \times (1-\delta_{n0})(n-1)c_{n-1}^{k-1} + (V_0)_{n+1}^{k-1}[(n+1) \\ & \times (n+2) + K](n+2)c_n^{-k}]) \Bigg\}, \end{aligned} \tag{91}$$

where $\iota = \sqrt{-1}$, $i = -(m + v + 1)$, $j = -(m + v)$, $k = -(m + v - 1)$, and the 2×3 arrays enclosed in square brackets are the spherical harmonic coupling coefficients defined in Eq. (II.1) of Appendix II. The algorithm we employ to evaluate these coefficients is also described in Appendix II. The asterisk over Q_ℓ^m in Eq. (91) denotes complex conjugation.

Equations (87) and (91) provide an explicit description of the coupling between poloidal and toroidal lithospheric flow due to lateral viscosity variations. In particular the selection rule (II.8) in Appendix II implies that the degree s components of the lateral viscosity variations will couple the degree $|\ell - s|$, $|\ell - s| + 2$, $|\ell - s| + 4, \ldots, \ell + s - 2, \ell + s$ components of the toroidal lithospheric flow and the degree $|\ell - s| - 1, |\ell - s| + 1, |\ell - s| + 3, \ldots, \ell + s - 1, \ell + s + 1$ components of the poloidal lithospheric flow to the degree ℓ toroidal flow in the lithosphere and underlying mantle.

Equation (87) constitutes a system of linear equations that may be rewritten as the following matrix equation:

$$\mathbf{w} = \underline{\mathbf{M}}\mathbf{v}, \tag{92}$$

in which $\mathbf{w}$ is a vector consisting of the complex conjugate of the left-hand side of (87) arranged in order of increasing ℓ,m, $\mathbf{v}$ is a vector consisting of the spherical harmonic coefficients $(\nu_L)_u^v$ arranged in order of increasing u,v, and $\underline{\mathbf{M}}$ is a matrix consisting of the terms enclosed in curly brackets in Eq. (91). If we require that the lithospheric flow field correspond to the observed plate velocities, then the vector $\mathbf{w}$ and matrix $\underline{\mathbf{M}}$ are known, and Eq. (92) may be inverted to determine the lateral viscosity variations that are consistent with the observed plate motions. According to Eqs. (48) and (49), we have

$$\begin{aligned}(V_0)_\ell^m &= -\frac{a}{\ell(\ell+1)}(\nabla_H \cdot \mathbf{v})_\ell^m; \\ (W_0)_\ell^m &= -\frac{a}{\ell(\ell+1)}(\hat{\boldsymbol{r}} \cdot \nabla \times \mathbf{v})_\ell^m,\end{aligned} \tag{93}$$

in which $(\nabla_H \cdot \mathbf{v})_\ell^m$ and $(\hat{\boldsymbol{r}} \cdot \nabla \times \mathbf{v})_\ell^m$ are respectively the spherical harmonic coefficients of the horizontal divergence and radial vorticity of the observed tectonic plate velocities.

The interpretation of the lateral viscosity variations yielded by an inversion of (92) will be facilitated by considering a useful approximation to the left-hand side of Eq. (87). As pointed out above, in the derivation of Eq. (71), if the viscosity jump in the two-layer parameterization of mantle viscosity is sufficiently large (i.e., $\gamma \geq 10$), then the left-hand side of (87) simplifies to

$$-\ell(\ell+1)\left\{\frac{[(\ell-1)+(\ell+2)(d/r_L)^{2\ell+1}]}{[1-(d/r_L)^{2\ell+1}]}\frac{\eta_M}{\langle\eta_L\rangle\varepsilon}+K\right\}(W_0)_\ell^m.$$

We may further simplify this expression for the case $d \approx r_L$. Writing $d = r_L(1-\delta)$, where δ is assumed to be small, we then obtain the following approximation to Eq. (87):

$$-F\,\ell(\ell+1)(W_0)_\ell^m \approx Q_\ell^m; \qquad F \equiv \frac{1}{\delta}\frac{\eta_M}{\langle\eta_L\rangle}\frac{1}{\varepsilon}+K. \tag{94}$$

For $d = r_{670}$, the radius corresponding to the bottom of the upper mantle, $\delta = 0.09$. In this case we are at the limits of the validity of expression (94), which becomes increasingly accurate as $\delta \to 0$ (e.g., $\delta \approx 0.01$ when $d = r_{200}$—if we wish to model a 100-km-thick asthenospheric channel). In the inversion experiments described below, the system of equations (92) will be based on the approximation (94) rather than Eq. (87). We may then ensure that the normalized field of lateral viscosity variations we recover will satisfy the viscosity–positivity constraint, $\nu_L(\theta,\phi) > -1$, by choosing the appropriate value for F in (94). We thereby constrain the magnitudes (and tradeoffs) of the various parameters appearing in the definition of F.

An important concern arising from the inversion of (94) is the magnitude of the bias produced by the inevitable truncation of the spherical harmonic expansion of the plate-velocity scalars $W_0(\theta, \phi)$, $V_0(\theta, \phi)$ and of the viscosity $\nu_L(\theta, \phi)$ itself. We will examine this issue by considering inversion experiments in which we choose different levels of truncation in the spherical harmonic expansion of the lateral viscosity variations.

In the first experiment we include the harmonic coefficients of the plate-velocity scalars in (93) up to degree and order 15 and invert (94) for the harmonic coefficients of the lateral viscosity variations up to degree and order 30. This truncation level for the viscosity is based on the selection rules for the coupling coefficients, in Eq. (91), which imply that viscosity variations corresponding to degrees $u > 30$ will not contribute to Q_ℓ^m (assuming that all plate-velocity coefficients vanish for degrees $n > 15$). The system of equations (92) that correspond to these truncation levels thus comprises 255 equations [corresponding to $\ell = 1-15$ in Eq. (94)] and 960 unknowns [corresponding to $u = 1-30$ in Eq. (91)]. We may invert this underdetermined system by seeking the minimum-norm field of lateral viscosity variations which satisfies (92). The harmonic coefficients of this minimum-norm viscosity are thus given by

$$\mathbf{v} = \underline{\mathbf{M}}^T(\underline{\mathbf{M}}\ \underline{\mathbf{M}}^T)^{-1}\mathbf{w}, \tag{95}$$

in which $\underline{\mathbf{M}}$, $\mathbf{v}$, and $\mathbf{w}$ are as defined previously in Eq. (92). We find, essentially by trial and error, that the field of lateral viscosity variations yielded by (95) bears no resemblance to the expected pattern of weak plate boundaries and strong plate interiors unless $K < -30$.

In Fig. 15a we show the lateral viscosity variations $\nu_L(\theta, \phi)$ inferred, according to (95), when $K = -40$. In this map it is immediately clear that the very-low-viscosity regions are almost entirely confined to the plate boundaries and the plate interiors have higher viscosities as expected. When $K = -40$ the inferred lateral viscosity variations satisfy the positivity condition $\nu_L(\theta, \phi) > -1$ when the constant F in (94) has values $F < 28$. The field shown in Fig. 15a assumes $F = 28$. If we assume a lithospheric thickness of 100 km ($\varepsilon = 0.016$) and an upper mantle layer defined by $d = r_{670}$ ($\delta = 0.09$) we then infer, according to (94), that $\langle\eta_L\rangle/\eta_M = 10$. According to the absolute lithospheric viscosity estimates in (51) for $K = -40$, we also infer, for $F = 28$, that $\eta_M \approx 0.8 \times 10^{21}$ Pa s.

The field of lateral viscosity variations yielded by (95), when $K = -60$, is nearly identical to that shown in Fig. 15a, provided that we select $F = 42$ to ensure that $\min[\nu_L] = -1$. In this case we find according to (94) (for $\varepsilon = 0.016$ and $\delta = 0.09$) that $F = 42$ implies $\langle\eta_L\rangle/\eta_M = 7$. The absolute viscosity estimate in (51), for $K = -60$, thus implies that $\eta_M \approx 0.9 \times 10^{21}$ Pa s. These inferences for the absolute value of the upper-mantle viscosity agree closely with those inferred, in Section 2.3, by matching the observed plate motions to the plate-like surface

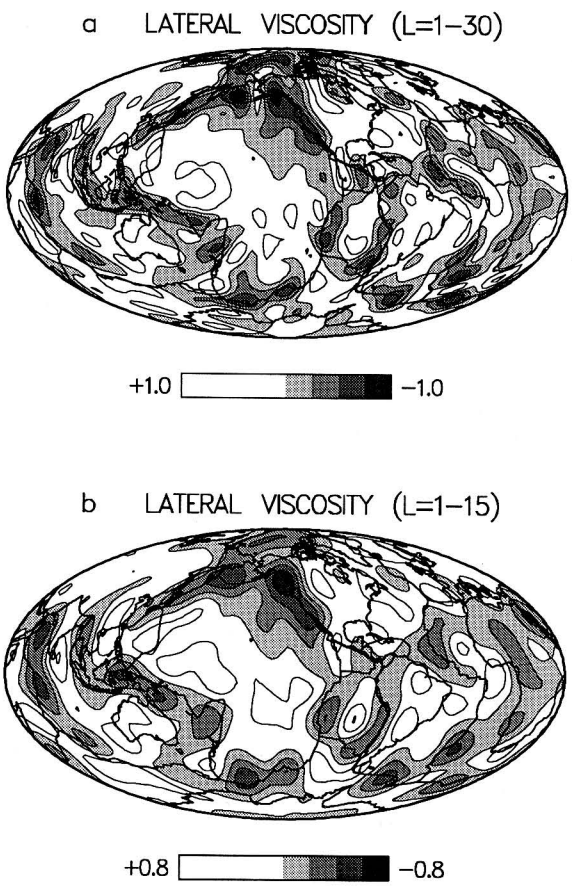

FIG. 15. (a) The field of lateral viscosity variations in the lithosphere [$\nu_L(\theta, \phi)$ defined in Eq. (56)], in the degree range $\ell = 1-30$, obtained from a minimum-norm inversion [see Eq. (95)] of Eq. (94) when $K = -40$. The amplitude of the normalized viscosity variations shown here is fixed by choosing $F = 28$ in Eq. (94). The lateral viscosity variations shown here are constrained by the observed long-wavelength ($\ell = 1-15$) plate divergence and vorticity. (b) The long-wavelength component, synthesized from harmonics in the range $\ell = 1-15$, of the lateral viscosity variations in (a).

flow calculated using the density perturbations derived from seismic models of mantle heterogeneity.

The amplitude spectrum of the lateral viscosity variations in Fig. 15a is shown in Fig. 16b by the square symbols. It is clear that the root-mean-square (rms) amplitude in any harmonic degree decreases sharply beyond degree $\ell = 18$. This is also verified by the map in Fig. 15b in which we show the lateral viscosity variations synthesized from the harmonic coefficients up to degree and order 15. The maps in Figs. 15a and 15b agree very well in their spatial pattern and in their

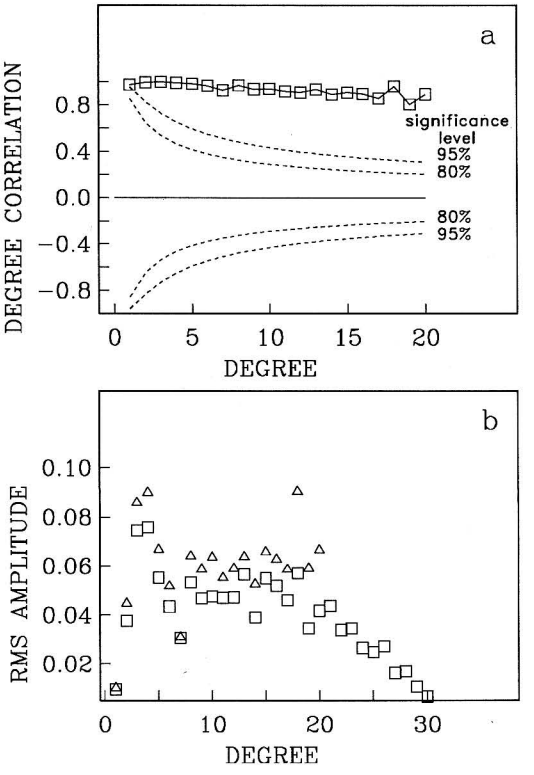

FIG. 16. (a) The cross-correlation, at each degree ℓ, between the field of lithospheric lateral viscosity variations in Fig. 15a and the field of lateral viscosity variations inferred from a separate inversion of Eq. (94) (with $K = -40$) in which the viscosity variations are truncated at (i.e., assumed to be zero beyond) degree 20. (b) The rms amplitude, at each degree ℓ, of the lateral viscosity variations $\nu_L(\theta, \phi)$ in Fig. 15a (□, "$\ell = 1$–30") and the lateral viscosity variations obtained from the truncated degree 20 inversion in (a) (△, "$\ell = 1$–20").

overall amplitude. This suggests that the coupling of the observed plate-velocity scalars synthesized from harmonic coefficients up to degree $\ell = 15$ may be adequately described by a field of lateral viscosity variations up to degree $\ell \approx 18$. We have directly tested this hypothesis by inverting Eq. (94) to determine the field of lateral viscosity variations, up to degree and order 20, which couples the observed plate-velocity scalars described up to degree and order 15. This inversion is again underdetermined, and thus we carry out the minimum-norm inversion described in Eq. (95). We find that when $K = -40$ the condition $\min[\nu_L] = -1$ requires us to select $F = 29$ (in close agreement with that inferred from the $\ell_{\max} = 30$ inversion). The amplitude spectrum of the $\ell_{\max} = 20$ inversion is shown in Fig. 16b by the triangle symbols. In Fig. 16a we show the correlation, at each harmonic

degree, between the lateral viscosity variations obtained from the $\ell_{max} = 20$ and $\ell_{max} = 30$ inversions.

These viscosity inversions have demonstrated that the poloidal and toroidal components of the observed lithospheric plate motions (and the equipartitioning of energy among these two components) may be explained by physically plausible lateral variations of the effective viscosity of the lithosphere. The lateral viscosity variations we infer reveal a clear pattern of weak plate boundaries and strong plate interiors. Although this may have been expected *a priori,* Fig. 15 shows some interesting and unexpected complexities. Although the East Pacific ridge is a region of rapid divergence and high heat flow, it does not appear to be a prominent zone of weakness. Significant reductions of strength are manifested in western North America, the Aleutian arc, and the Pacific–Antarctic ridge. This suggests a combined thermal and nonlinear (strain-induced softening) interpretation of the lateral variations in Fig. 15. Such an interpretation must be viewed with some caution, however, because these viscosity inferences are obtained from a significantly underdetermined inversion procedure. Unfortunately the viscosity inversions described here tells us nothing concerning the possible importance of lateral viscosity variations in the deep mantle. This is the subject to which we turn in the next section.

4. Mantle Dynamics with 3D Viscosity Variations

The equations describing the effects of an arbitrary three-dimensional (3D) viscosity distribution on buoyancy-induced mantle flow are derived in Appendix IV. The two coupled differential equations [Eqs. (IV.10) and (IV.11)], governing the poloidal and toroidal flows, are evidently rather complicated and are not amenable to straightforward mathematical analysis. In this section we shall describe an alternative approach based on a variational formulation of the momentum equation. As suggested in Forte (1992), this variational treatment allows us to explicitly derive the important symmetry relations that govern the relationship between poloidal and toroidal flows and the driving density contrasts. The application of a variational approach to mantle-flow problems was also considered recently by Čadek *et al.* (1993), who suggest the application of an iterative numerical scheme. The formulation that we shall present is noniterative and enables the derivation of an explicit solution for the flow velocities in a spherical shell with heterogeneous viscosity.

4.1. Formulation of the Variational Principle

The hydrodynamic field equations, in Cartesian tensor notation, that describe the conservation of mass, momentum, and the relationship between stress and strain rate are respectively, in the Boussinesq approximation:

$$\partial_k u_k = 0, \tag{96}$$

$$\partial_k T_{ki} + \rho_0 \partial_i \phi_1 + \rho_1 \partial_i \phi_0 = 0, \tag{97}$$

$$T_{ij} = -P_1 \delta_{ij} + 2\eta E_{ij}; \qquad E_{ij} = \tfrac{1}{2}(\partial_i u_j + \partial_j u_i). \tag{98}$$

The various quantities appearing in (96)–(98) are defined in Appendix IV. In Eq. (97) we have already subtracted the hydrostatic background state in which $\partial_i P_0 = \rho_0 \partial_i \phi_0$. Equations (96)–(98) describe a flow field u_i driven by density perturbations ρ_1, which are assumed to be known *a priori* (and thus treated as fixed). This flow is assumed to occur in a medium occupying a volume V and bounded by a surface S. The flow u_i will satisfy the following boundary conditions on S:

$$\hat{n}_i u_i = 0, \tag{99}$$

$$\hat{h}_i \hat{n}_j T_{ji} = 0 \quad \text{on} \quad S_1, \tag{100}$$

$$u_i = c_i \quad \text{on} \quad S_2, \tag{101}$$

where $\hat{n}_i$ is the unit vector that is everywhere normal to S, $\hat{h}_i$ is any unit vector that is tangent to any point on $S (\hat{n}_i \hat{h}_i = 0)$, S_1 is the portion of S on which the free-slip condition (100) applies, S_2 is the remaining portion of S (i.e., $S_2 \equiv S - S_1$) on which a given *tangential* velocity field $c_i (\hat{n}_i c_i = 0)$ is prescribed.

Let us now introduce a kinematically admissible flow perturbation δu_i satisfying Eq. (96), such that the flow field $u_i + \delta u_i$ satisfies the same boundary conditions (99)–(101) [the flow u_i, of course, satisfies Eqs. (96)–(101)]. The inner product of δu_i with Eq. (97) yields

$$\partial_k (T_{ki} \delta u_i) - T_{ki} (\partial_k \delta u_i) + \partial_i (\rho_0 \phi_1 \delta u_i) + \rho_1 \delta u_i \partial_i \phi_0 = 0, \tag{102}$$

in which we have used $\partial_i \delta u_i = 0$. Integrating Eq. (102) over the volume V occupied by the medium, we obtain

$$\int_V [\rho_1 \delta u_i \, \partial_i \phi_0 - T_{ki} \delta E_{ki}] dV + \int_S [\hat{n}_k T_{ki} \delta u_i + \rho_0 \phi_1 \hat{n}_k \delta u_k] \, dS = 0, \tag{103}$$

in which we employed the result $T_{ki} \partial_k \delta u_i = T_{ki} \delta E_{ki}$, which follows from the symmetry of T_{ki}. Both u_i and $u_i + \delta u_i$ satisfy Eq. (99) and thus $\hat{n}_k \delta u_k = 0$ on S. Since u_i and $u_i + \delta u_i$ satisfy Eq. (101), it is clear that the δu_i must vanish on S_2 and, owing to condition (100), $\hat{n}_k T_{ki} \delta u_i$ must vanish on S_1. Clearly the surface integral in (103) must vanish, thus yielding

$$\int_V [2\eta E_{ij} \delta E_{ij} - \rho_1 \partial_i \phi_0 \delta u_i] dV = 0. \tag{104}$$

To obtain (104) we have also used $P_1 \delta_{ki} \delta E_{ki} = P_1 \delta E_{kk} = 0$, owing to (96). As the density perturbations ρ_1 and the reference gravity $\partial_i \phi_0$ are known *a priori* (and are thus treated as constant), we may rewrite (104) as

$$\delta W = 0; \qquad W = \int_V [\eta E_{ij} E_{ij} - \rho_1 u_i \partial_i \phi_0] dV. \tag{105}$$

In writing Eq. (105) we have made the important assumption that $\delta\eta = 0$, which is valid only when the viscosity is not dependent on the flow velocity u_i [i.e., when the rheology is linear and thus characterized by a stress exponent $n = 1$ in Eq. (3)]. The strong temperature dependence of viscosity shown in Eq. (3) implies that the dependence on strain or stress will be relatively weak, and thus Eq. (105) is expected to hold very well in the mantle. It is possible to formulate a hybrid variational principle when the viscosity is stress-dependent; the interested reader may refer to the initial study of Čadek *et al.* (1993).

The quantity W in Eq. (105) is the difference between the rate of viscous dissipation of energy ($\eta E_{ij} E_{ij}$) and the rate of energy released by buoyancy ($\rho_1 u_i \partial_i \phi_0$). We have shown that a flow field satisfies the field equations (96)–(98), and the boundary conditions (99)–(101), if and only if the functional W in (105) is stationary with respect to perturbations of the flow field. We may further show that W is also an absolute minimum for this flow field. Let u_i^0 be the flow which satisfies $\delta W = 0$ in (105) [and thus Eqs. (96)–(101)], and let u_i^1 be any kinematically admissible flow satisfying Eqs. (96), (99), (100), and $u_i^1 = 0$ on S_2. For the flow $u_i = u_i^0 + \varepsilon u_i^1$ the quantity W in (105) may be written as

$$\begin{aligned} W = & \int_V [\eta E_{ij}^0 E_{ij}^0 - \rho_1 u_i^0 \partial_i \phi_0] dV \\ & + \varepsilon \int_V [2\eta E_{ij}^0 E_{ij}^1 - \rho_1 u_i^1 \partial_i \phi_0] dV \\ & + \varepsilon^2 \int_V \eta E_{ij}^1 E_{ij}^1 dV, \end{aligned} \tag{106}$$

where E_{ij}^0 and E_{ij}^1 are the strain-rate tensors that correspond respectively to u_i^0 and u_i^1. According to (106) we may regard W as a function of ε:

$$W(\varepsilon) = W(0) + \left(\frac{dW}{d\varepsilon}\right)_0 \varepsilon + \frac{1}{2}\left(\frac{d^2W}{d\varepsilon^2}\right)_0 \varepsilon^2, \tag{107}$$

where $W(0)$, $(dW/d\varepsilon)_0$, and $(d^2W/d\varepsilon^2)_0$ correspond respectively to the first, second, and third integrals in (106). According to Eq. (105), we have $\delta W = (dW/d\varepsilon)_0 \delta\varepsilon = 0$ and thus $(dW/d\varepsilon)_0 = 0$. Expression (107) thus simplifies to

$$W(\varepsilon) = W(0) + \frac{1}{2}\left(\frac{d^2W}{d\varepsilon^2}\right)_0 \varepsilon^2.$$

Since

$$\left(\frac{d^2W}{d\varepsilon^2}\right)_0 = 2 \int_V \eta E_{ij}^1 E_{ij}^1 dV$$

is a positive–definite quantity, it is clear that $W(0)$ must be the absolute minimum of $W(\varepsilon)$. This minimum principle is immediately recognizable as an extension of the *minimum-dissipation theorem* of Helmholtz (e.g., Batchelor, 1967, pp. 227–228) to fluids with internal buoyancy sources.

4.2. Variational Calculation of Buoyancy-Induced Flow

The application of the variational principle (105) to the problem of viscous flow in a spherical shell is considerably facilitated by the use of generalized spherical harmonic basis functions. A detailed discussion of the use of generalized spherical harmonics, in problems of elastodynamics in spherical geometry, is given by Phinney and Burridge (1973) (hereafter referred to as PB for convenience). The derivations presented below will be extensively based on the covariant differentiation rules described in PB. The principal properties of generalized spherical harmonic basis functions $Y_\ell^{Nm}(\theta, \phi)$ are described in Appendix II, and these properties are extensively exploited in the following derivations.

We begin by expressing $E_{ij}E_{ij}$ in terms of the so-called contravariant canonical components that are described in PB:

$$\begin{aligned} E_{ij}E_{ij} &= C_{i\alpha}C_{j\beta}E^{\alpha\beta}C_{i\gamma}C_{j\delta}E^{\gamma\delta} = e_{\alpha\gamma}e_{\beta\delta}E^{\alpha\beta}E^{\gamma\delta} \\ &= E^{00}E^{00} + 2E^{++}E^{--} + 2E^{+-}E^{+-} - 4E^{0+}E^{0-}, \end{aligned} \tag{108}$$

in which

$$\begin{aligned} E^{\alpha\beta} &= \tfrac{1}{2}[u^{\alpha,\beta} + u^{\beta,\alpha}] \\ &= \frac{1}{2}\sum_{\ell=0}^{\infty}\sum_{m=-\ell}^{\ell}[U_\ell^{(\alpha|\beta)m}(r) + U_\ell^{(\beta|\alpha)m}(r)]Y_\ell^{(\alpha+\beta)m}(\theta, \phi). \end{aligned} \tag{109}$$

Employing the covariant differentiation rules in PB to evaluate the $U_\ell^{(\alpha|\beta)m}(r)$ in (109), we obtain

$$\begin{aligned} E^{00} &= \sum_{\ell,m}(E_1)_\ell^m Y_\ell^{0m}, \qquad E^{+-} = \sum_{\ell,m}(E_2)_\ell^m Y_\ell^{0m}, \qquad E^{0+} = \sum_{\ell,m}(E_3)_\ell^m Y_\ell^{1m}, \\ E^{0-} &= \sum_{\ell,m}(E_4)_\ell^m Y_\ell^{-1m}, \qquad E^{++} = \sum_{\ell,m}(E_5)_\ell^m Y_\ell^{2m}, \qquad E^{--} = \sum_{\ell,m}(E_6)_\ell^m Y_\ell^{-2m}, \end{aligned} \tag{110}$$

where

$$\begin{aligned} (E_1)_\ell^m &= \frac{dU_\ell^{0m}}{dr}, \qquad (E_2)_\ell^m = \frac{\Omega_1^\ell}{2r}[U_\ell^{+m} + U_\ell^{-m}] - \frac{1}{r}U_\ell^{0m}, \\ (E_3)_\ell^m &= \frac{1}{2}\left(\frac{d}{dr} - \frac{1}{r}\right)U_\ell^{+m} + \frac{\Omega_1^\ell}{2r}U_\ell^{0m}, \quad (E_4)_\ell^m = \frac{1}{2}\left(\frac{d}{dr} - \frac{1}{r}\right)U_\ell^{-m} + \frac{\Omega_1^\ell}{2r}U_\ell^{0m}, \\ (E_5)_\ell^m &= \frac{1}{r}\Omega_2^\ell U_\ell^{+m}, \quad (E_6)_\ell^m = \frac{1}{r}\Omega_2^\ell U_\ell^{-m}, \end{aligned} \tag{111}$$

in which $U_\ell^{\alpha m}$ is the radially varying (generalized) spherical harmonic coefficient of the contravariant flow-velocity component u^α,

$$u^\alpha(r,\ \theta,\ \phi) = \sum_{\ell,m} U_\ell^{\alpha m}(r) Y_\ell^{\alpha m}(\theta,\ \phi),$$

and

$$\Omega_1^\ell = \sqrt{\ell(\ell+1)/2}, \qquad \Omega_2^\ell = \sqrt{(\ell-1)(\ell+2)/2}.$$

Substitution of the expressions in (110) into Eq. (108), and the subsequent use of the coupling rule (II.19) in Appendix II, yields the following result:

$$\begin{aligned} E_{ij}E_{ij} = \sum_{\ell,m}\sum_{s,t}\sum_{J=|\ell-s|}^{\ell+s} & [(2\ell+1)(2s+1)(2J+1)]^{1/2}\begin{pmatrix} \ell & s & J \\ m & t & -m-t \end{pmatrix} \\ & \times \left\{ (E_1)_\ell^m (E_1)_s^t \begin{pmatrix} \ell & s & J \\ 0 & 0 & 0 \end{pmatrix} + 2(E_5)_\ell^m (E_6)_s^t \begin{pmatrix} \ell & s & J \\ 2 & -2 & 0 \end{pmatrix} + 2(E_2)_\ell^m (E_2)_s^t \right. \\ & \left. \times \begin{pmatrix} \ell & s & J \\ 0 & 0 & 0 \end{pmatrix} - 4(E_3)_\ell^m (E_4)_s^t \begin{pmatrix} \ell & s & J \\ 1 & -1 & 0 \end{pmatrix} \right\} (Y_J^{0\,-m-t})^*. \end{aligned} \tag{112}$$

We now introduce the following harmonic decomposition of the 3D viscosity distribution:

$$\eta(r,\ \theta,\ \phi) = \sum_{u,v} \eta_u^v(r) Y_u^v(\theta,\ \phi). \tag{113}$$

Combining expressions (112) and (113), we obtain

$$\begin{aligned} \int_V \eta E_{ij}E_{ij}\, dV = \sum_{\ell,m}\sum_{s,t}\sum_{J=|\ell-s|}^{\ell+s} & 4\pi[(2\ell+1)(2s+1)(2J+1)]^{1/2} \\ & \times \begin{pmatrix} \ell & s & J \\ m & t & -m-t \end{pmatrix} \int_b^a \eta_J^{-m-t}(r) \\ & \times \left\{ [(E_1)_\ell^m (E_1)_s^t + 2(E_2)_\ell^m (E_2)_s^t] \begin{pmatrix} \ell & s & J \\ 0 & 0 & 0 \end{pmatrix} + 2(E_5)_\ell^m (E_6)_s^t \right. \\ & \left. \times \begin{pmatrix} \ell & s & J \\ 2 & -2 & 0 \end{pmatrix} - 4(E_3)_\ell^m (E_4)_s^t \begin{pmatrix} \ell & s & J \\ 1 & -1 & 0 \end{pmatrix} \right\} r^2\, dr, \end{aligned} \tag{114}$$

in which $r = b$ defines the inner surface of the shell and $r = a$ defines the outer surface of the shell.

We now evaluate the buoyancy integral in (105):

$$\int_V \rho_1 u_i \partial_i \phi_0\, dV = -\int_V \rho_1 u_r g_0\, dV, \tag{115}$$

in which $g_0(r)$ is the radial gravitational acceleration. The radial flow u_r is identi-

cal to the contravariant flow component u^0, and we therefore obtain from (115) the following:

$$\int_V \rho_1 u_i \partial_i \phi_0 \, dV = -\sum_{\ell,m} 4\pi \int_b^a (\rho_1)_\ell^{m*} U_\ell^{0m} g_0 r^2 \, dr, \tag{116}$$

in which $(\rho_1)_\ell^m$ is the radially varying spherical harmonic coefficient of the density perturbation field $\rho_1(r, \theta, \phi)$.

The solenoidal velocity field **u,** which satisfies Eq. (96), may be written as (Backus, 1958):

$$\mathbf{u} = \nabla \times \Lambda p + \Lambda q, \tag{117}$$

where $p(r, \theta, \phi)$, $q(r, \theta, \phi)$ are respectively the poloidal and toroidal flow scalars. The contravariant flow components $u^\alpha(r, \theta, \phi)$ may be obtained from (117) using

$$u^\alpha = C_{\alpha i}^\dagger \, u_i, \tag{118}$$

where $C_{\alpha i}^\dagger$ is the unitary (complex rotation) matrix defined in PB. Combining (117) and (118), we may show that

$$\begin{aligned} U_\ell^{0m}(r) &= -\frac{2(\Omega_1^\ell)^2}{r} p_\ell^m(r), \\ U_\ell^{-m}(r) &= -\Omega_1^\ell \left(\frac{1}{r} \frac{d}{dr} [r p_\ell^m(r)] + \iota q_\ell^m(r) \right), \\ U_\ell^{+m}(r) &= -\Omega_1^\ell \left(\frac{1}{r} \frac{d}{dr} [r p_\ell^m(r)] - \iota q_\ell^m(r) \right), \end{aligned} \tag{119}$$

in which $\iota = \sqrt{-1}$ and $p_\ell^m(r)$, $q_\ell^m(r)$ are respectively the spherical harmonic coefficients of the poloidal and toroidal flow scalars.

On the basis of expression (119) we now obtain the explicit poloidal–toroidal dependence of the terms in (111) that appear in the viscous dissipation integral (114):

$$\begin{aligned} (E_1)_\ell^m(r) &= -\frac{2(\Omega_1^\ell)^2}{r} \left[\frac{dp_\ell^m(r)}{dr} - \frac{1}{r} p_\ell^m(r) \right], \qquad (E_2)_\ell^m(r) = \frac{1}{2} (E_1)_\ell^m(r), \\ (E_3)_\ell^m(r) &= -\frac{\Omega_1^\ell}{2} \left[\frac{d^2 p_\ell^m(r)}{dr^2} + \frac{2(\Omega_2^\ell)^2}{r^2} p_\ell^m(r) \right] + \iota \frac{\Omega_1^\ell}{2} \left[\frac{dq_\ell^m(r)}{dr} - \frac{q_\ell^m(r)}{r} \right], \\ (E_4)_\ell^m(r) &= -\frac{\Omega_1^\ell}{2} \left[\frac{d^2 p_\ell^m(r)}{dr^2} + \frac{2(\Omega_2^\ell)^2}{r^2} p_\ell^m(r) \right] - \iota \frac{\Omega_1^\ell}{2} \left[\frac{dq_\ell^m}{dr} - \frac{q_\ell^m(r)}{r} \right], \\ (E_5)_\ell^m(r) &= -\frac{(\Omega_1^\ell)(\Omega_2^\ell)}{r} \left[\frac{dp_\ell^m(r)}{dr} + \frac{p_\ell^m(r)}{r} - \iota q_\ell^m(r) \right], \\ (E_6)_\ell^m(r) &= -\frac{(\Omega_1^\ell)(\Omega_2^\ell)}{r} \left[\frac{dp_\ell^m(r)}{dr} + \frac{p_\ell^m(r)}{r} + \iota q_\ell^m(r) \right]. \end{aligned} \tag{120}$$

Substitution of (120) into (114) yields

$$\int_V \eta E_{ij}E_{ij}\, dV = 4\pi \sum_{\ell,m}\sum_{s,t}\sum_{J=|\ell-s|}^{\ell+s} [(2\ell+1)(2s+1)(2J+1)]^{1/2}$$
$$\times \begin{pmatrix} \ell & s & J \\ m & t & -m-t \end{pmatrix} \int_b^a \eta_J^{-m-t}(r) \left\{ \begin{pmatrix} \ell & s & J \\ 0 & 0 & 0 \end{pmatrix} \frac{6(\Omega_1^\ell)^2(\Omega_1^s)^2}{r^2} \right.$$
$$\times \left[\frac{dp_\ell^m}{dr} - \frac{p_\ell^m}{r}\right]\left[\frac{dp_s^t}{dr} - \frac{p_s^t}{r}\right] + \begin{pmatrix} \ell & s & J \\ 2 & -2 & 0 \end{pmatrix} \frac{2\Omega_1^\ell\Omega_2^\ell\Omega_1^s\Omega_2^s}{r^2}$$
$$\times \left[\frac{dp_\ell^m}{dr} + \frac{p_\ell^m}{r} - \iota q_\ell^m\right]\left[\frac{dp_s^t}{dr} + \frac{p_s^t}{r} + \iota q_s^t\right] - \begin{pmatrix} \ell & s & J \\ 1 & -1 & 0 \end{pmatrix}$$
$$\times\ \Omega_1^\ell\Omega_1^s\left[\frac{d^2p_\ell^m}{dr^2} + \frac{2(\Omega_2^\ell)^2}{r^2}\, p_\ell^m - \iota r \frac{d}{dr}\left(\frac{q_\ell^m}{r}\right)\right]$$
$$\left.\times \left[\frac{d^2p_s^t}{dr^2} + \frac{2(\Omega_2^s)^2}{r^2}\, p_s^t + \iota r \frac{d}{dr}\left(\frac{q_s^t}{r}\right)\right]\right\} r^2\, dr. \tag{121}$$

The substitution of (119) into (116) also yields

$$\int_V \rho_1 u_i \partial_i \phi_0\, dV = 4\pi \sum_{\ell,m} 2(\Omega_1^\ell)^2 \int_b^a \frac{(\rho_1)_\ell^{m*}}{r}\, p_\ell^m\, g_0 r^2\, dr. \tag{122}$$

The variational principle in (105) requires that we minimize the functional W with respect to the flow field $\mathbf{u}$. To accomplish this minimization, in a manner that directly provides the flow solution, we expand the poloidal and toroidal flow coefficients in terms of radial basis functions:

$$p_\ell^m(r) = \sum_{n=1}^{N} {}_np_\ell^m f_n(r)$$
$$q_\ell^m(r) = \sum_{n=1}^{N} {}_nq_\ell^m g_n(r). \tag{123}$$

The radial basis functions $f_n(r)$ and $g_n(r)$ must satisfy the boundary conditions (99)–(101). When the expressions in (123) are substituted in Eqs. (121) and (122), the function W in (105) will then vary according to the values of the coefficients ${}_np_\ell^m$ and ${}_nq_\ell^m$. The particular values of these coefficients that minimize W will define the flow solution. When W is a minimum, the following conditions must necessarily be satisfied:

$$\frac{\partial W}{\partial({}_np_s^t)} = \frac{\partial}{\partial({}_np_s^t)} \int_V [\eta E_{ij}E_{ij} - \rho_1 u_i \partial_i \phi_0]\, dV = 0, \tag{124}$$

$$\frac{\partial W}{\partial({}_n q_s^t)} = \frac{\partial}{\partial({}_n q_s^t)} \int_V \eta E_{ij} E_{ij}\, dV = 0. \tag{125}$$

The set of coefficients ${}_n p_s^t$ and ${}_n q_s^t$ that satisfy (124) and (125) define the flow solution we seek.

The substitution of expression (123) into (121) and (122), and the evaluation of (124), yields (omitting algebraic details) the following:

$$\sum_k \sum_{\ell,m} I_1(k,\ \ell,\ m;\ n,\ s,\ t)\ {}_k p_\ell^m + \sum_k \sum_{\ell,m} J_2(k,\ \ell,\ m;\ n,\ s,\ t)\ {}_k q_\ell^m = \frac{2(\Omega_1^s)^2}{\eta_0} \int_b^a g_0 f_n \frac{(\rho_1)_s^{t*}}{r}\, r^2\, dr, \tag{126}$$

in which

$$\begin{aligned} I_1(k,\ \ell,\ m;\ n,\ s,\ t) = {} & \sum_{J=|\ell-s|}^{\ell+s} [(2\ell+1)(2s+1)(2J+1)]^{1/2} \\ & \times \begin{pmatrix} \ell & s & J \\ m & t & -m-t \end{pmatrix} \int_b^a \frac{\eta_J^{-m-t}}{\eta_0} \left[\begin{pmatrix} \ell & s & J \\ 0 & 0 & 0 \end{pmatrix} \frac{12(\Omega_1^\ell)^2(\Omega_1^s)^2}{r^2} \right. \\ & \times \left[\frac{df_k}{dr} - \frac{f_k}{r}\right]\left[\frac{df_n}{dr} - \frac{f_n}{r}\right] + \frac{(1+(-1)^{\ell+s+J})}{2} \left\{ \begin{pmatrix} \ell & s & J \\ 2 & -2 & 0 \end{pmatrix} \right. \\ & \times \frac{4\Omega_1^\ell \Omega_2^\ell \Omega_1^s \Omega_2^s}{r^2} \left[\frac{df_k}{dr} + \frac{f_k}{r}\right]\left[\frac{df_n}{dr} + \frac{f_n}{r}\right] - \begin{pmatrix} \ell & s & J \\ 1 & -1 & 0 \end{pmatrix} \\ & \left. \left. \left. \times 2\Omega_1^\ell \Omega_1^s \left[\frac{d^2 f_k}{dr^2} + \frac{2(\Omega_2^\ell)^2}{r^2} f_k\right]\left[\frac{d^2 f_n}{dr^2} + \frac{2(\Omega_2^s)^2}{r^2} f_n\right] \right\} \right] r^2\, dr, \end{aligned} \tag{127}$$

$$\begin{aligned} J_2(k,\ \ell,\ m;\ n,\ s,\ t) = {} & -\iota \sum_{J=|\ell-s|}^{\ell+s} [(2\ell+1)(2s+1)(2J+1)]^{1/2} \\ & \times \begin{pmatrix} \ell & s & J \\ m & t & -m-t \end{pmatrix} \frac{(1-(-1)^{\ell+s+J})}{2} \int_b^a \frac{\eta_J^{-m-t}}{\eta_0} \\ & \times \left\{ \begin{pmatrix} \ell & s & J \\ 2 & -2 & 0 \end{pmatrix} \frac{4\Omega_1^\ell \Omega_2^\ell \Omega_1^s \Omega_2^s}{r^2} g_k \left[\frac{df_n}{dr} + \frac{f_n}{r}\right] \right. \\ & - \begin{pmatrix} \ell & s & J \\ 1 & -1 & 0 \end{pmatrix} 2\Omega_1^\ell \Omega_1^s \left[r \frac{d}{dr}\left(\frac{g_k}{r}\right)\right] \\ & \left. \times \left[\frac{d^2 f_n}{dr^2} + \frac{2(\Omega_2^s)^2}{r^2} f_n\right] \right\} r^2\, dr, \end{aligned} \tag{128}$$

where η_0 is simply a reference viscosity employed to normalize the viscosity dis-

tribution. The symmetry of the first Wigner symbol in the integrand of (127) [see Eq. (II.25) in Appendix II], and the presence of the factor $[1 + (-1)^{\ell+s+J}]$, implies that the sum in (127) extends only over the values $J = |\ell - s|, |\ell - s| + 2, \ldots, \ell + s - 2, \ell + s$. Similarly, the factor $[1 - (-1)^{\ell+s+J}]$ in (128) implies that the sum extends only over the values $J = |\ell - s| + 1, |\ell - s| + 3, \ldots, \ell + s - 3, \ell + s - 1$.

The substitution of (123) into Eq. (121), and the evaluation of (125), yields (again, omitting algebraic details) the following:

$$\sum_k \sum_{\ell,m} J_1(k, \ell, m;\ n, s, t)\ {}_k q_\ell^m = \sum_k \sum_{\ell,m} I_2(k, \ell, m;\ n, s, t)\ {}_k p_\ell^m, \tag{129}$$

in which

$$\begin{aligned} J_1(k, \ell, m;\ n, s, t) = \sum_{J=|\ell-s|}^{\ell+s} & [(2\ell + 1)(2s + 1)(2J + 1)]^{1/2} \begin{pmatrix} \ell & s & J \\ m & t & -m - t \end{pmatrix} \\ & \times \frac{(1 + (-1)^{\ell+s+J})}{2} \int_b^a \frac{\eta_J^{-m-t}}{\eta_0} \left\{ \begin{pmatrix} \ell & s & J \\ 2 & -2 & 0 \end{pmatrix} \right. \\ & \times \frac{4\Omega_1^\ell \Omega_2^\ell \Omega_1^s \Omega_2^s}{r^2} g_k g_n - \begin{pmatrix} \ell & s & J \\ 1 & -1 & 0 \end{pmatrix} 2\Omega_1^\ell \Omega_1^s \\ & \times \left. \left[r \frac{d}{dr} \left(\frac{g_k}{r} \right) \right] \left[r \frac{d}{dr} \left(\frac{g_n}{r} \right) \right] \right\} r^2\ dr, \end{aligned} \tag{130}$$

$$\begin{aligned} I_2(k, \ell, m;\ n, s, t) = & -\iota \sum_{J=|\ell-s|}^{\ell+s} [(2\ell + 1)(2s + 1)(2J + 1)]^{1/2} \\ & \times \begin{pmatrix} \ell & s & J \\ m & t & -m - t \end{pmatrix} \frac{(1 - (-1)^{\ell+s+J})}{2} \int_b^a \frac{\eta_J^{-m-t}}{\eta_0} \\ & \times \left\{ \begin{pmatrix} \ell & s & J \\ 2 & -2 & 0 \end{pmatrix} \frac{4\Omega_1^\ell \Omega_2^\ell \Omega_1^s \Omega_2^s}{r^2} \left[\frac{df_k}{dr} + \frac{f_k}{r} \right] g_n \right. \\ & - \begin{pmatrix} \ell & s & J \\ 1 & -1 & 0 \end{pmatrix} 2\Omega_1^\ell \Omega_1^s \left[\frac{d^2 f_k}{dr^2} + \frac{2(\Omega_2^\ell)^2}{r^2} f_k \right] \\ & \times \left. \left[r \frac{d}{dr} \left(\frac{g_n}{r} \right) \right] \right\} r^2\ dr. \end{aligned} \tag{131}$$

The presence of the factor $[1 + (-1)^{\ell+s+J}]$ in (130) implies that the sum extends only over the values $J = |\ell - s|, |\ell - s| + 2, \ldots, \ell + s - 2, \ell + s$. Similarly, the presence of the factor $[1 - (-1)^{\ell+s+J}]$ in (131) implies that the sum extends only over the values $J = |\ell - s| + 1, |\ell - s| + 3, \ldots, \ell + s - 3, \ell + s - 1$.

Equations (126) and (129) constitute a coupled system of *linear* equations for the flow variables ${}_kp_\ell^m$ and ${}_kq_\ell^m$. This linearity ensures that the usual principle of superposition remains valid [i.e., if $\mathbf{u}_1(r, \theta, \phi)$ is excited by density perturbation $\delta\rho_1(r, \theta, \phi)$ and $\mathbf{u}_2(r, \theta, \phi)$ is excited by density perturbation $\delta\rho_2(r, \theta, \phi)$, then $\mathbf{u}_1 + \mathbf{u}_2$ will be excited by $\delta\rho_1 + \delta\rho_2$]. This linearity thus implies that the concept of Green functions (e.g. Forte and Peltier, 1987) will also be valid in a spherical fluid shell with a given 3D distribution of viscosity.

Equation (126) describes the flow that is directly excited by buoyancy forces, and this equation corresponds to the differential equation (IV.10) derived in Appendix IV. In Eq. (126) we observe that buoyancy forces will, in general, directly excite a *toroidal* flow field. This, of course, will not be true in a mantle with spherically symmetric viscosity, and indeed one may readily verify that $J_2(k, \ell, m; n, s, t) = 0$ when $\eta(r, \theta, \phi) = \eta_0^0(r)$. On the basis of the spherical harmonic coupling relations contained in expressions (127) and (128), we may observe that a degree s field of density perturbations will directly excite the following flow components:

$$
(\rho_1)_s^t \Rightarrow \begin{array}{lllll}
p_s^t, & \text{via} & \eta_o^o(r); & & \\
p_{s-1}^{t-m}, & p_{s+1}^{t-m}, & \text{and} & q_s^{t-m}, & \text{via } \eta_1^m(r); \\
\cdot & & & & \\
\cdot & & & & \\
\cdot & & & & \\
p_{|\ell-s|}^{t-m}, & p_{|\ell-s|+2}^{t-m}, \ldots, & p_{\ell+s-2}^{t-m}, & p_{\ell+s}^{t-m}, & \text{and} \\
q_{|\ell-s|+1}^{t-m}, & q_{|\ell-s|+3}^{t-m}, \ldots, & q_{\ell+s-3}^{t-m}, & q_{\ell+s-1}^{t-m}, & \text{via } \eta_\ell^m(r)
\end{array} \tag{132}
$$

Equation (126) also describes the viscous coupling of the buoyancy-induced flow in (132) to other flow components not directly coupled to buoyancy sources. We may understand the nature of this viscous coupling with the following example. Let us assume for simplicity that the only component of density heterogeneity is given by degree s and order t, as in (132). Equation (132) is valid for all degrees, including $s \pm 1$, $s \pm 2$, $s \pm 3, \ldots$, for which the density heterogeneity is assumed to be zero. We thus see that a η_1^m viscosity structure will lead to the coupling of $p_{s\pm2}^{t-m}$, $p_{s\pm3}^{t-m}, \ldots$, poloidal flow components to the components p_{s-1}^{t-m}, p_s^t, p_{s+1}^{t-m}, in (132). Even the apparently simple interaction of $(\rho_1)_s^t$ density heterogeneity with η_1^m lateral viscosity variations will generate poloidal flow components corresponding to all harmonic degrees. In the particular case of an η_1^m lateral viscosity structure we expect that the flow corresponding to p_s^t and the nearest-neighbor terms p_{s-1}^{t-m}, p_{s+1}^{t-m}, q_s^{t-m} will be strongest.

The poloidal and toroidal flow components excited by buoyancy forces in Eq. (126) are not independent. Equation (129) describes the coupling that must exist between the poloidal flow components and the toroidal flow components;

this equation corresponds directly to differential Equation (IV.11) derived in Appendix IV. On the basis of the spherical harmonic coupling implicit in expressions (130) and (131) we may verify that the toroidal flow components will be coupled to poloidal flow as follows:

$$\begin{aligned} & p_s^{t-m} \rightarrow \quad q_{s-1}^{t-m}, \quad q_{s+1}^{t-m}, \quad \text{via} \quad \eta_1^m(r); \\ & \cdot \\ & \cdot \\ & \cdot \\ & p_{|\ell-s|+1}^{t-m}, \quad p_{|\ell-s|+3}^{t-m}, \quad \ldots, \quad p_{\ell+s-3}^{t-m}, \quad p_{\ell+s-1}^{t-m} \rightarrow \\ & q_{|\ell-s|}^{t-m}, \quad q_{|\ell-s|+2}^{t-m}, \quad \ldots, \quad q_{\ell+s-2}^{t-m}, \quad q_{\ell+s}^{t-m}, \quad \text{via} \quad \eta_\ell^m(r). \end{aligned} \tag{133}$$

4.3. Generalized Green Functions

In the previous section we noted that the flow equations (126) and (129) are linear in the flow variables, thus ensuring the validity of the linear superposition principle. The concept of the Green function may therefore be generalized to a fluid shell with lateral viscosity variations. We begin our derivation of generalized Green functions by rewriting Eqs. (126) and (129) as follows:

$$\sum_{k,\ell,m} I_1(k,\ \ell,\ m;\ n,\ s,\ -t)\ {}_k p_\ell^m + \sum_{k,\ell,m} J_2(k,\ \ell,\ m;\ n,\ s,\ -t)\ {}_k q_\ell^m$$

$$= \frac{2(\Omega_1^s)^2}{\eta_0}(-1)^t \int_b^a g_0 f_n \frac{(\rho_1)_s^t}{r} r^2\ dr, \tag{134}$$

$$\sum_{k,\ell,m} J_1(k,\ \ell,\ m;\ n,\ s,\ -t)\ {}_k q_\ell^m = \sum_{k,\ell,m} I_2(k,\ \ell,\ m;\ n,\ s,\ -t)\ {}_k p_\ell^m. \tag{135}$$

We now rewrite (134) and (135) as

$$\sum_{k,\ell,m} A_{nst}^{k\ell m}\ {}_k p_\ell^m + \sum_{k,\ell,m} B_{nst}^{k\ell m}\ {}_k q_\ell^m = L_{nst}, \tag{136}$$

$$\sum_{k,\ell,m} C_{nst}^{k\ell m}\ {}_k q_\ell^m = \sum_{k,\ell,m} D_{nst}^{k\ell m}\ {}_k p_\ell^m, \tag{137}$$

in which

$$\begin{aligned} A_{nst}^{k\ell m} &= I_1(k,\ \ell,\ m;\ n,\ s,\ -t), \qquad B_{nst}^{k\ell m} = J_2(k,\ \ell,\ m;\ n,\ s,\ -t), \\ L_{nst} &= \frac{2(\Omega_1^s)^2}{\eta_0}(-1)^t \int_b^a g_0 f_n \frac{(\rho_1)_s^t}{r} r^2\ dr, \\ C_{nst}^{k\ell m} &= J_1(k,\ \ell,\ m;\ n,\ s,\ -t), \qquad D_{nst}^{k\ell m} = I_2(k,\ \ell,\ m;\ n,\ s,\ -t). \end{aligned} \tag{138}$$

It is clear that Eqs. (136) and (137) constitute a coupled set of matrix equations in

which the rows of the individual matrices, given in (138), are defined by letting (k, ℓ, m) vary, for a given (n, s, t), and the columns are defined by letting (n, s, t) vary for a fixed (k, ℓ, m).

The solution of Eqs. (136) and (137) may be formally written as

$$ {}_k p_\ell^m = \sum_{n,s,t} P_{k\ell m}^{nst} L_{nst}, \tag{139} $$

$$ {}_k q_\ell^m = \sum_{n,s,t} Q_{k\ell m}^{nst} L_{nst}, \tag{140} $$

where the matrix elements $P_{k\ell m}^{nst}$ in (139) are obtained from

$$ \underline{\mathbf{P}} = [\underline{\mathbf{A}} + \underline{\mathbf{B}}\,\underline{\mathbf{C}}^{-1}\,\underline{\mathbf{D}}]^{-1}, \tag{141} $$

and the matrix elements $Q_{k\ell m}^{nst}$ in (140) are obtained from

$$ \underline{\mathbf{Q}} = \underline{\mathbf{C}}^{-1}\,\underline{\mathbf{D}}\,\underline{\mathbf{P}}. \tag{142} $$

Combining the expression for L_{nst}, in (138), with expression (123) and (139) and (140), we obtain

$$ p_\ell^m(r) = \frac{g_0}{\eta_0} \int_b^a \sum_{s,t} \left[\sum_{k,n} f_k(r) P_{k\ell m}^{nst} f_n(r') 2(\Omega_1^s)^2 (-1)^t r'^2 \right] \frac{(\rho_1)_s^t(r')}{r'}\, dr', \tag{143} $$

$$ q_\ell^m(r) = \frac{g_0}{\eta_0} \int_b^a \sum_{s,t} \left[\sum_{k,n} g_k(r) Q_{k\ell m}^{nst} f_n(r') 2(\Omega_1^s)^2 (-1)^t r'^2 \right] \frac{(\rho_1)_s^t(r')}{r'}\, dr'. \tag{144} $$

Expressions analogous to (143) and (144) were obtained in the derivation of poloidal flow Green functions, for a spherically symmetric mantle, by Forte and Peltier (1987):

$$ p_\ell^m(r) = \frac{g_0}{\eta_0} \int_b^a p_\ell(r, r') \frac{(\rho_1)_\ell^m(r')}{r'}\, dr', \tag{145} $$

in which $p_\ell(r, r')$ is the poloidal flow Green function. The definition of the generalized Green functions, which describe the excitation of flow by buoyancy forces in a fluid shell with lateral viscosity variations, is immediately evident from a comparison of (145) with (143) and (144):

$$ P_{\ell m}^{st}(r, r') = \sum_{k,n} f_k(r) P_{k\ell m}^{nst} f_n(r') 2(\Omega_1^s)^2 (-1)^t r'^2, \tag{146} $$

$$ Q_{\ell m}^{st}(r, r') = \sum_{k,n} g_k(r) Q_{k\ell m}^{nst} f_n(r') 2(\Omega_1^s)^2 (-1)^t r'^2, \tag{147} $$

in which $P_{\ell m}^{st}(r, r')$ and $Q_{\ell m}^{st}(r, r')$ are respectively the poloidal and toroidal Green functions.

We have so far avoided making an explicit choice for the radial basis functions $f_k(r)$ and $g_k(r)$ used to describe the poloidal and toroidal flow scalars, respectively.

Any choice for these basis functions, provided it satisfies the boundary conditions (99)–(101), will be acceptable. In the case of free-slip, zero radial velocity, boundary conditions at $r = a, b$, the poloidal and toroidal flow scalars must satisfy

$$\begin{aligned} p_\ell^m(r) &= 0 = \frac{d^2 p_\ell^m(r)}{dr^2}, \\ \frac{d}{dr}\left(\frac{q_\ell^m(r)}{r}\right) &= 0, \quad \text{at} \quad r = a, b. \end{aligned} \tag{148}$$

Perhaps the simplest and most easily employed set of radial basis functions that satisfy (148) are the following:

$$\begin{aligned} f_k(r) &= \sin\left[k\pi\left(\frac{r-a}{a-b}\right)\right], \\ g_k(r) &= r\cos\left[k\pi\left(\frac{r-a}{a-b}\right)\right]. \end{aligned} \tag{149}$$

A relatively straightforward illustration of the utility of the radial basis functions in (149) is provided by considering the horizontal divergence $(\nabla_H \cdot \mathbf{u})(r = a)$ of surface flow in an isoviscous fluid shell. According to Eq. (A13) in Forte and Peltier (1987) we have

$$(\nabla_H \cdot \mathbf{u})_\ell^m(r = a) = \frac{\ell(\ell+1)}{a}\left[\frac{d}{dr} p_\ell^m(r)\right]_{r=a}. \tag{150}$$

On the basis of expressions (143) and (146), we thus obtain

$$(\nabla_H \cdot \mathbf{u})_\ell^m(r = a) = \frac{g_0}{\eta_0}\int_b^a \sum_{s,t} S_{\ell m}^{st}(r')(\rho_1)_s^t(r')\, dr', \tag{151}$$

in which the generalized horizontal divergence kernel $S_{\ell m}^{st}(r')$ is given by

$$S_{\ell m}^{st}(r') = \frac{\ell(\ell+1)}{a}\sum_{k,n}^{N}\left[\frac{df_k(r)}{dr}\right]_{r=a} P_{k\ell m}^{nst} f_n(r') 2(\Omega_1^s)^2(-1)^t r'. \tag{152}$$

In a fluid shell with spherically symmetric viscosity the terms $P_{k\ell m}^{nst}$ will vanish for all $\ell \neq s$ and $m \neq t$. In an isoviscous fluid shell, the exact expression for the horizontal divergence kernel $S_\ell(r')$, derived in Appendix A in Forte and Peltier (1987), is as follows:

$$\begin{aligned} S_\ell(r') = {} & \frac{\ell(\ell+1)}{2(2\ell+1)} \\ & \times \left[\left(\frac{a}{r'}\right)^\ell \frac{1-(r'/b)^{2\ell+3}}{1-(a/b)^{2\ell+3}} - \left(\frac{a}{r'}\right)^{\ell-2} \frac{1-(r'/b)^{2\ell-1}}{1-(a/b)^{2\ell-1}}\right]. \end{aligned} \tag{153}$$

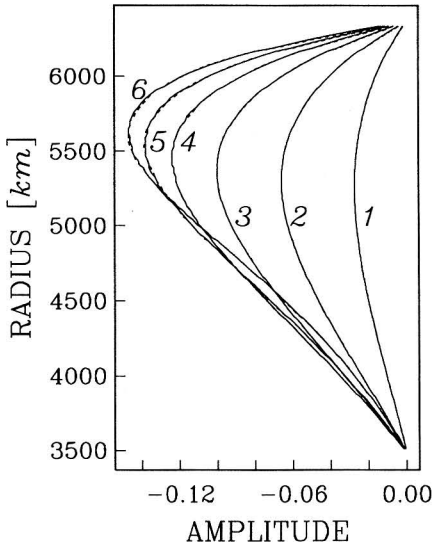

FIG. 17. Horizontal divergence kernels for an isoviscous mantle. The degree ℓ defining each kernel is indicated by the adjacent number. The solid lines are the kernels calculated with the exact theory embodied in Eq. (153). The dashed lines are the kernels calculated on the basis of the variational principle and are defined by Eq. (152), in which $N = 10$. The dashed and solid lines are essentially overlapping, indicating the accuracy of the variational procedure.

In Fig. 17 we show a selection of divergence kernels given by the exact expression (153), in solid lines, along with the kernels provided by expression (152), with $N = 10$ and $f_k(r)$ in (149), shown by dashed lines. The kernels obtained with radial basis $f_k(r)$ in (149) are virtually identical to the exact ones. On the basis of this excellent performance we shall truncate the sums over k and n in (143) and (144) at $k = n = 10$, for all the calculations that follow.

4.4. Horizontal Divergence and Radial Vorticity of Buoyancy-Induced Surface Flow

To investigate the effects of lateral viscosity variations in a fluid shell (e.g., the Earth's mantle) we shall once again express the viscosity variations according to Eq. (56), that is,

$$\eta(r, \theta, \phi) = \eta_0^0(r)[1 + \nu(r, \theta, \phi)], \tag{154}$$

in which $\eta_0^0(r)$ is the spherical average of the field $\eta(r, \theta, \phi)$ at any radius r and $\nu(r, \theta, \phi)$ describes the lateral variations of viscosity relative to this horizontal average (this implies that the $\ell = 0$, $m = 0$ spherical harmonic component of $\nu(r, \theta, \phi)$ vanishes). The parameterization in (154) allows us to describe extreme lateral variations of viscosity with relatively small amplitude variations in

$\nu(r, \theta, \phi)$. By letting $\nu(r, \theta, \phi)$ approach values arbitrarily close to -1 we may easily describe viscosity reductions spanning several orders of magnitude.

The first example illustrating the effects of lateral viscosity variation will be based on the degree 1 field of lateral variations $\nu(r, \theta, \phi)$, obtained by scaling the depth-integrated degree 1 shear–velocity heterogeneity $\delta v_s / v_s$ in model SH8/WM13 of Woodward *et al.* (1993):

$$\nu(\theta, \phi) = f_x \sum_{m=-1}^{1} \left[\int_b^a \left(\frac{\delta v_s}{v_s} \right)_1^m r^2 \, dr \right] Y_1^m(\theta, \phi), \tag{155}$$

in which the scaling factor f_x is selected so that

$$\min[\nu] = -x \tag{156}$$

where $x > 0$. We emphasize that the degree 1 field given by Eq. (155) does not vary with radius. In Fig. 18 we show the degree 1 viscosity variation $\nu(\theta, \phi)$ when $f_x = f_{0.9}$ (i.e., $\min[\nu] = -0.9$). The region of minimum viscosity is centered near the Pacific–Antarctic spreading ridge, which, in model SH8/WM13, is a region of strongly reduced shear velocity extending throughout the underlying upper mantle. The choice $x = 0.9$ implies that, at any depth, the viscosity $\eta(r, \theta, \phi)$ will vary from a minimum value of 0.1 $\eta_0^0(r)$ to a maximum value 1.9 $\eta_0^0(r)$ (i.e., a factor of 19 lateral variation).

We now consider the horizontal divergence and radial vorticity of the surface flow generated in the presence of the degree 1 lateral viscosity variations in Fig. 18. The general expression for the horizontal divergence was given by Eqs. (151)–(152). The radial vorticity $(\hat{\boldsymbol{r}} \cdot \boldsymbol{\nabla} \times \mathbf{u})_t^m(r = a)$ is given by

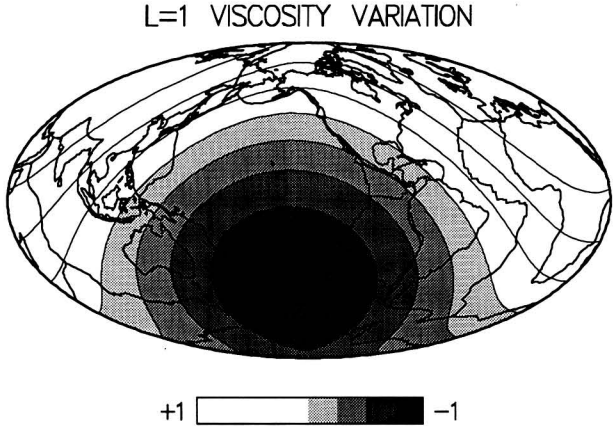

FIG. 18. The degree 1 field of normalized lateral variations of viscosity [i.e., $\nu(\theta, \phi)$ in Eq. (154)], obtained from the depth-integrated degree 1 shear–velocity heterogeneity in model SH8/WM13 according to Eq. (155). The factor f_x in Eq. (155) is chosen such that the minimum value of the field is -0.9. The maximum value of this field is then $+0.9$.

$$(\hat{\mathbf{r}} \cdot \nabla \times \mathbf{u})^m_\ell(r = a) = -\frac{\ell(\ell + 1)}{a} q^m_\ell(r = a). \tag{157}$$

Combining (144) and (157), we therefore obtain

$$(\hat{\mathbf{r}} \cdot \nabla \times \mathbf{u})^m_\ell(r = a) = \frac{g_0}{\eta_0} \int_b^a \sum_{s,t} R^{st}_{\ell m}(r')(\rho_1)^t_s(r')dr', \tag{158}$$

in which the radial vorticity kernel $R^{st}_{\ell m}(r')$ is given by

$$R^{st}_{\ell m}(r') = -\frac{\ell(\ell + 1)}{a} \sum_{k,n} g_k(r = a) Q^{nst}_{k\ell m} f_n(r') 2(\Omega^s_1)^2(-1)^t r'. \tag{159}$$

A consideration of some of the divergence and vorticity kernels will explicitly demonstrate the flow coupling due to the $\ell = 1$ viscosity variations in (155). We assume, for simplicity, that $\eta^0_0(r) \equiv \eta_0$ (i.e., constant). In Fig. 19 we show the divergence kernels for $\ell = 1 - 6$, corresponding to a Re[$Y^1_1(\theta, \phi)$] density load

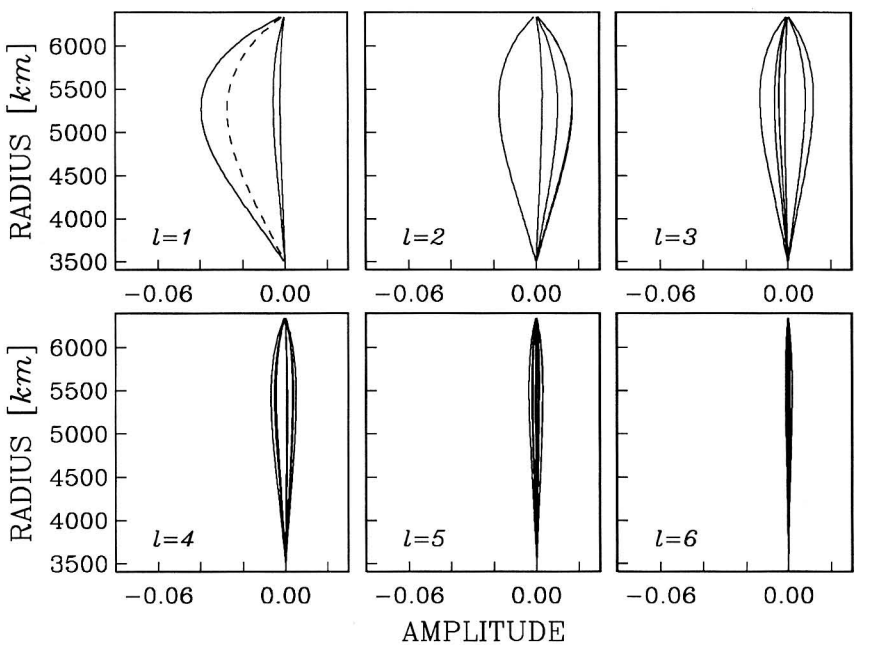

FIG. 19. The horizontal divergence kernels $S^v_{\ell m}(r')$, defined in Eq. (152) with $N = 10$, corresponding to a Re[$Y^1_1(\theta, \phi)$] density load (i.e., for $s = 1$, $t = 1$). The 3D viscosity distribution is given by the degree 1 field of lateral viscosity variations $\nu(\theta, \phi)$ in Fig. 18 and a spherically symmetric viscosity $\eta^0_0(r)/\eta_0 = 1$, such that $\eta(r, \theta, \phi)/\eta_0 = 1 + \nu(\theta, \phi)$. In each of the panels are the $2\ell + 1$ divergence kernels corresponding to the real and imaginary parts of $S^v_{\ell m}(r')$ for $m = 0, 1, \ldots, \ell$. The dashed line in the panel labeled "$\ell = 1$" is the single non-zero-divergence kernel for the spherically symmetric viscosity distribution $\eta(r, \theta, \phi)/\eta_0 = 1$ [in this case, $S^v_{\ell m}(r') = 0$ unless $(\ell, m) = (s, t)$].

(i.e., $s = 1$, $t = 1$). According to (132) we expect significant flow at degrees 1 and 2 that is directly driven by this density load. This is indeed the case in Fig. 19. We also observe that the divergence at $\ell = 3$ is also significant. This degree 3 field is produced by viscous coupling to the buoyancy-driven $\ell = 1$ flow. The degree 4 divergence is produced by viscous coupling to the degree 2 flow, which is itself maintained by viscous coupling to the degree 1 buoyancy forces, and thus is much weaker than the degree 3 flow. Viscous coupling also yields a degree 5 divergence (coupled to degree 3 flow), a degree 6 divergence (coupled to degree 4 flow), and so on. Clearly, the strength of viscous coupling is strongly diminished beyond degree 3, owing to the very limited spectral range of the lateral viscosity field (only degree 1 in this example).

In Fig. 20 we have the radial vorticity kernels, for $\ell = 1-6$, corresponding to the $\mathrm{Re}[Y_1^1(\theta, \phi)]$ density load. According to (132), we expect a viscous coupling of the degree 1 buoyancy to degree 1 toroidal flow, and this is clearly evident in Fig. 20. The degree 2 vorticity is produced by viscous coupling to the degree 1 buoyancy-induced poloidal flow according to Eq. (133). The degree 3 vorticity is generated by viscous coupling to degree 2 and 3 poloidal flows according to

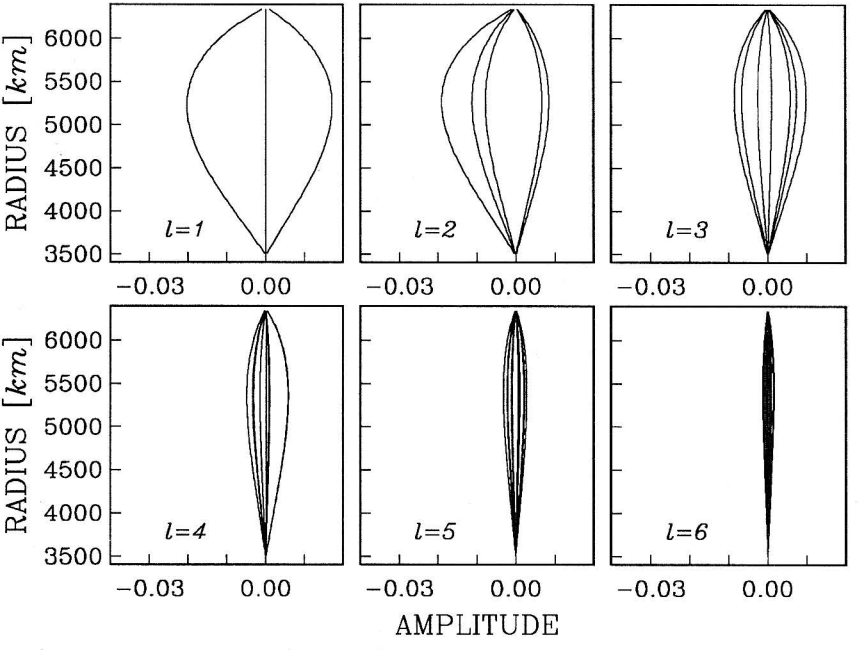

FIG. 20. The radial vorticity kernels $R^v_{\ell m}(r')$, defined in Eq. (10) with $N = 10$, corresponding to a $\mathrm{Re}[Y_1^1(\theta, \phi)]$ density load (i.e., for $s = 1$, $t = 1$). The 3D viscosity distribution is the same as in Fig. 19. In each panel are the $2\ell + 1$ vorticity kernels corresponding to the real and imaginary parts of $R^v_{\ell m}(r')$ for $m = 0, 1, \ldots, \ell$. Observe that the vorticity kernel $\mathrm{Re}[R^1_1(r')]$ is identically zero.

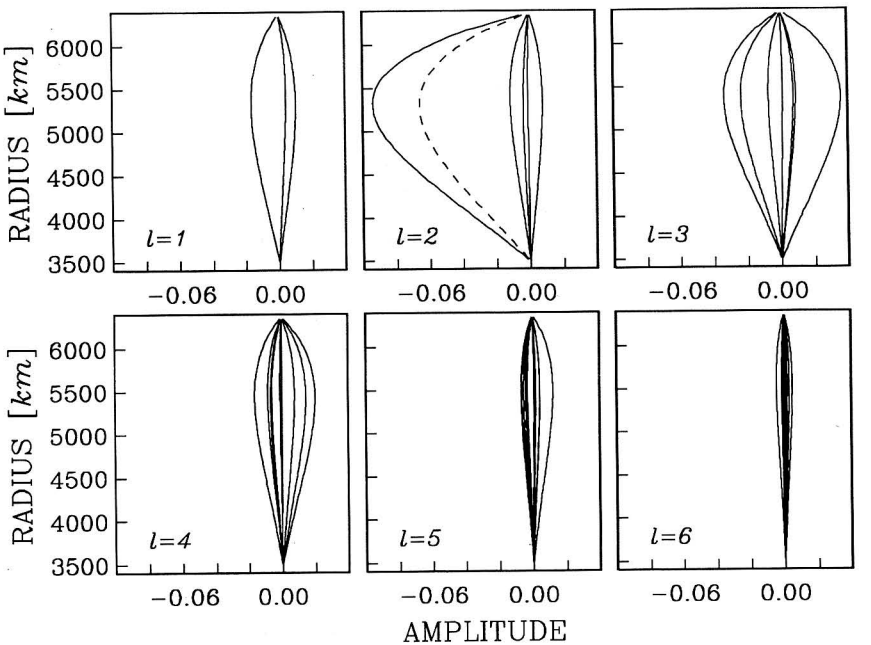

FIG. 21. The horizontal divergence kernels $S^{u}_{\ell m}(r')$, defined in Eq. (152) with $N = 10$, corresponding to an $\mathrm{Im}[Y^2_2(\theta, \phi)]$ density load [i.e., for $s = 2$, $t = 2$]. The 3D viscosity distribution is the same as in Fig. 19. In each panel are the $2\ell + 1$ divergence kernels corresponding to the real and imaginary parts of $S^{u}_{\ell m}(r')$ for $m = 0, 1, \ldots, \ell$. The dashed line in the panel labeled "$\ell = 2$" is the single non-zero-divergence kernel for the spherically symmetric viscosity distribution $\eta(r, \theta, \phi)/\eta_0 = 1$ (i.e., for $\ell = 2$, $m = 2$).

(133). The degree 4 vorticity is generated by viscous coupling to degree 3 and 4 poloidal flows, and so on. Clearly, as in the case of the divergence field, viscous coupling yields rapidly diminishing vorticity beyond degree 3 because of the limited spectral range of the lateral viscosity variations.

As a further illustration of the mechanism of coupling, we show in Fig. 21 the divergence kernels corresponding to the interaction of an $\mathrm{Im}[Y^2_2(\theta, \phi)]$ density load with the degree 1 viscosity variations. According to (132), we expect dominant flow at $\ell = 2$ and significant flow at $\ell = 1,3$ arising from the viscous coupling to the degree 2 buoyancy forces. These expectations are verified in Fig. 21. The degree 4 divergence in Fig. 21 arises through viscous coupling to the degree 2 flow. The degree 5 and 6 divergences are respectively coupled to the degree 3 and 4 flows and, since they are already "twice removed" from the primary buoyancy force, their amplitudes are now significantly weaker than the divergence at $\ell \leq 4$. According to (132), we also expect significant buoyancy-driven degree 2 toroidal flow and this is verified by the vorticity kernels shown in Fig. 22. The degree 1 and 3 vorticities are generated by viscous coupling to the degree 2

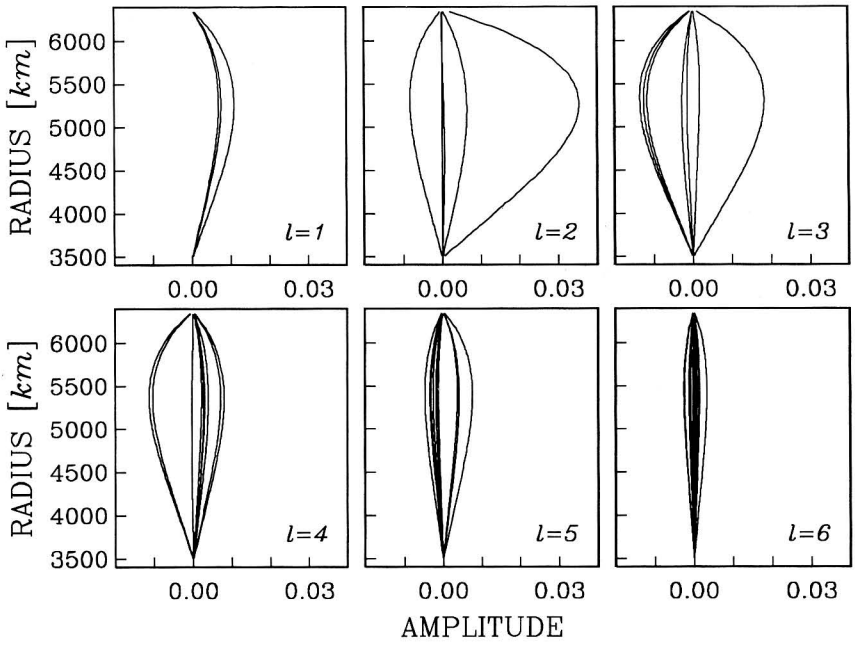

FIG. 22. The radial vorticity kernels $R^{sl}_{\ell m}(r')$, defined in Eq. (159) with $N = 10$, corresponding to an $\mathrm{Im}[Y^2_{\frac{2}{2}}(\theta, \phi)]$ density load [i.e., for $s = 2$, $t = 2$]. The 3D viscosity distribution is the same as in Fig. 19. In each of the panels are the $2\ell + 1$ vorticity kernels corresponding to the real and imaginary parts of $R^{sl}_{\ell m}(r')$ for $m = 0, 1, \ldots, \ell$. Observe that the vorticity kernel $\mathrm{Im}[R^{22}_{22}(r')]$ is identically zero.

buoyancy-driven poloidal flow, according to (133). The degree 4 vorticity is viscously coupled to degree 3 poloidal flow and the degree 2 toroidal flow, according to (133). Again we see that the strength of viscous coupling to the higher degree ($\ell > 4$) flows is considerably weaker than for the $\ell \leq 4$ toroidal flows.

We now present predictions of buoyancy-induced surface flow, based on the degree $\ell = 1,2$ field of density perturbations derived from model SH8/WM13 (Woodward *et al.*, 1993) and the $\delta \ln \rho / \delta \ln v_s$ scaling factor in Fig. 6b. In Fig. 23a we show the predicted $\ell = 1,2$ surface divergence for an isoviscous mantle [$\eta^0_0(r) = \eta_0 = 10^{21}$ Pa s]. In Fig. 23b we show the surface divergence (for $\ell = 1-6$), produced when the $\ell = 1,2$ density perturbations interact with the depth-invariant degree 1 field of lateral viscosity variations $\eta(\theta, \phi) = \eta_0[1 + \nu(\theta, \phi)]$, where $\nu(\theta, \phi)$ is shown in Fig. 18. Comparison of Figs. 23a and 23b shows that the flow field distortion produced by the lateral viscosity variations is quite extensive. The region of much "softer" mantle, underlying the Pacific–Antarctic ridge, has strongly intensified the local vertical flow while significantly reducing its strength elsewhere. The dominant strength of the downwellings, and the relatively more diffuse upwellings, in Fig. 23a is now reversed in Fig. 23b, where the single

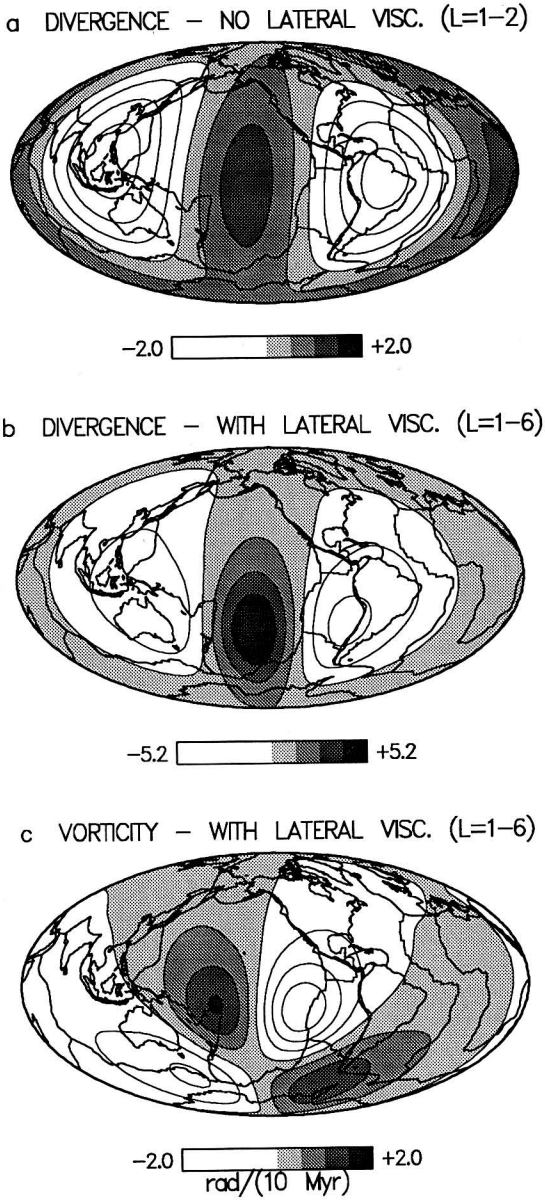

FIG. 23. (a) The degree $\ell = 1-2$ surface divergence in an isoviscous mantle [i.e., $\eta(r, \theta, \phi)/\eta_0 = 1$], calculated according to Eq. (151) with $N = 10$, due to the degrees 1–2 density perturbations derived from model SH8/WM13. The $\delta \ln \rho/\delta \ln v_s$ conversion factor is that shown in Fig. 6. (b) The degree $\ell = 1-6$ surface divergence in a mantle with 3D viscosity $\eta(r, \theta, \phi)/\eta_0 = 1 + \nu(\theta, \phi)$, where $\nu(\theta, \phi)$ is the degree 1 viscosity variation in Fig. 18, calculated according to Eq. (151) with $N = 10$. The density perturbations are again obtained from the degree 1–2 heterogeneity in SH8/WM13, with $\delta \ln \rho/\delta \ln v_s$ from Fig. 6. (c) The degree $\ell = 1-6$ surface radial vorticity, with 3D viscosity as in (b), calculated according to Eq. (158) with $N = 10$. The density perturbations employed are as in (a) and (b). In all cases the reference viscosity value is $\eta_0 = 10^{21}$ Pa s. The units on all scale bars are rad/(10 Myr).

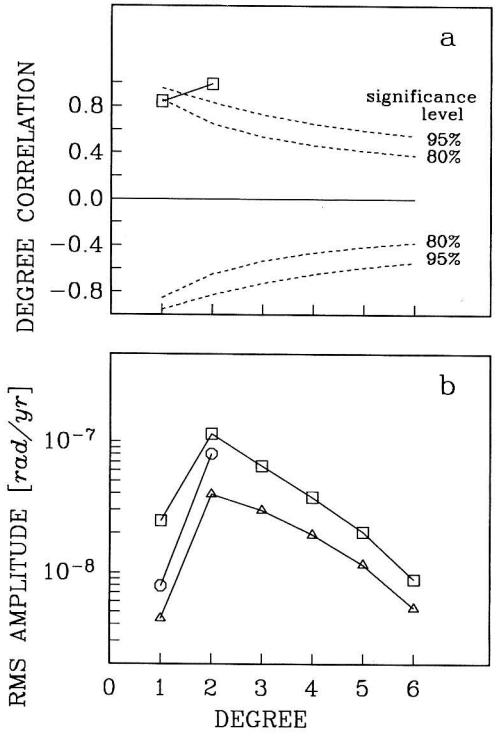

FIG. 24. (a) The cross-correlation, at each degree ℓ, between predicted divergence in Fig. 23a and that in Fig. 23b. (b) The rms amplitude, at each degree ℓ, of the predicted divergence in Fig. 23a (○, divergence, no lateral viscosity), the predicted divergence in Fig. 23b (□, divergence, with lateral viscosity), the predicted radial vorticity in Fig. 23c (△, vorticity, with lateral viscosity).

upwelling is clearly stronger than the adjacent downwellings. In Fig. 23c we show the corresponding radial vorticity field (for $\ell = 1-6$). The regions of peak vorticity are situated in the zones of nearly zero surface divergence that define the transition from upwelling to downwelling. A quantitative summary of the surface flow predictions is presented in Fig. 24.

The degree $\ell = 1$ field of lateral viscosity variations in Fig. 18 is clearly an overly simplified representation of the actual lateral variations of strength in the Earth's mantle. In Fig. 25 we present a more realistic representation of lateral viscosity variations obtained, as in (155), from the depth-integrated $\ell = 1-5$ shear velocity heterogeneity in model SH8/WM13:

$$\nu(\theta, \phi) = f_x \sum_{\ell=1}^{5} \sum_{m=-\ell}^{\ell} \left[\int_b^a \left(\frac{\delta v_s}{v_s} \right)_\ell^m r^2 \, dr \right] Y_\ell^m(\theta, \phi). \qquad (160)$$

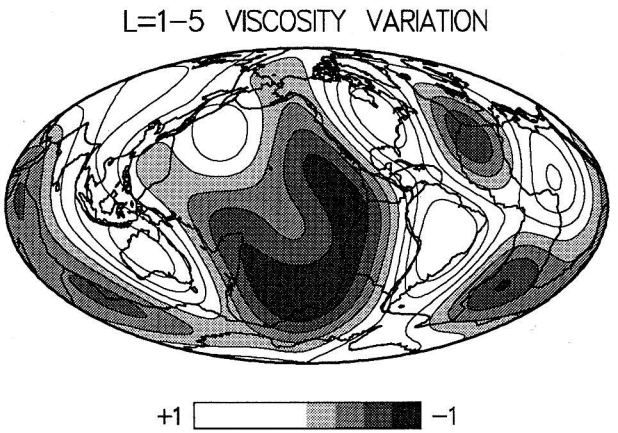

FIG. 25. The degree 1–5 field of normalized lateral variations of viscosity [i.e., $\nu(\theta, \phi)$ in Eq. (154)], obtained from the depth integrated degree 1–5 shear–velocity heterogeneity in model SH8/WM13 according to Eq. (160). The factor f_x in Eq. (160) is chosen such that the minimum value of the field shown here is -0.99. The maximum value is $+1.18$.

In Fig. 25 we have chosen $x = 0.99$, such that min $[\nu] = -0.99$. The maximum value of $\nu(\theta, \phi)$ is 1.18 and consequently the viscosity variations in Fig. 25 imply that, at any depth, $\eta(r, \theta, \phi)$ will vary from a minimum of 0.01 $\eta_0^0(r)$ to a maximum of 2.18 $\eta_0^0(r)$ (i.e., by a factor of 218 laterally).

We shall again consider the buoyancy-induced surface flow generated by the interaction of the $\ell = 1-2$ density perturbations with the field of viscosity variations in Fig. 25. The predicted $\ell = 1-2$ divergence for an isoviscous mantle, with $\eta_0^0(r) = \eta_0 = 10^{21}$ Pa s, is shown again in Fig. 26a. In Fig. 26b we show the $\ell = 1-6$ surface divergence produced in the presence of the depth-invariant viscosity structure $\eta(\theta, \phi) = \eta_0[1 + \nu(\theta, \phi)]$, where $\nu(\theta, \phi)$ is shown in Fig. 25. A comparison of Figs. 23b and 26b shows that the peak value of the divergence in the latter case is significantly smaller than in the former case. This may appear somewhat puzzling, given that the field of viscosity variations employed in Fig. 26b varies laterally by a factor 218, whereas in Fig. 23b the viscosity varied laterally by a factor of 19 only. This behavior may be understood by noting that the regular geometry of the degree 1 field of viscosity variations in Fig. 18, relative to the geometry of the mantle buoyancy sources, is ideally placed for strongly focusing the central Pacific upwelling. The relatively irregular and broken pattern of mantle "softening" in Fig. 25 is not as effectively situated, relative to the mantle buoyancy sources, and thus is less efficient at amplifying the surface flow. In Fig. 26c we show the $\ell = 1-6$ radial vorticity field generated in the presence of the lateral viscosity variations in Fig. 25.

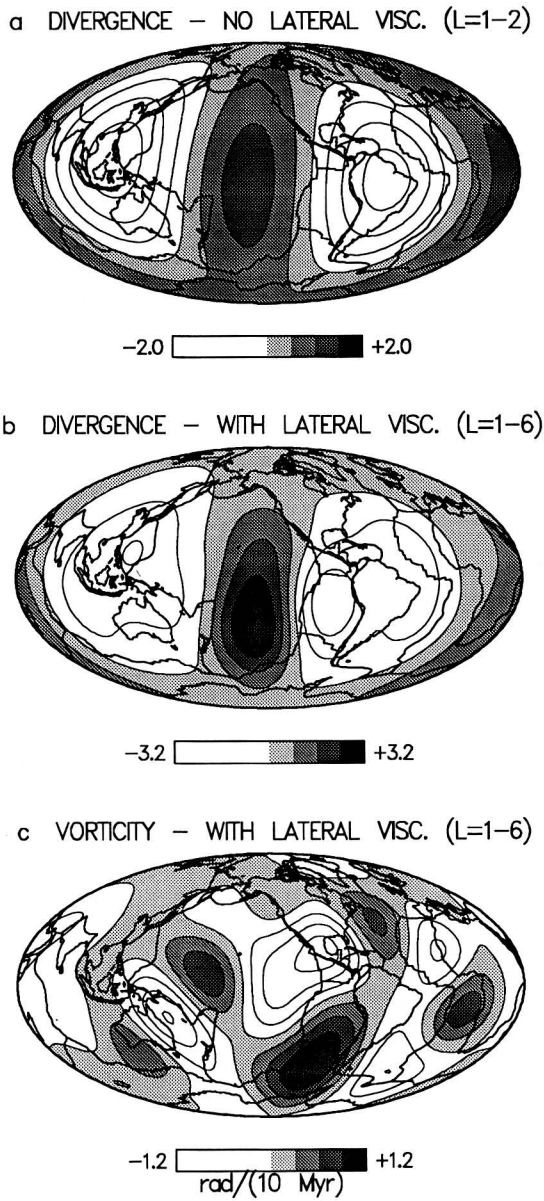

FIG. 26. (a) The degree $\ell = 1-2$ surface divergence in an isoviscous mantle [i.e., $\eta(r, \theta, \phi)/\eta_0 = 1$], calculated according to Eq. (151) with $N = 10$, due to the degree 1–2 density perturbations derived from model SH8/WM13 (using $\delta \ln \rho/\delta \ln v_s$ in Fig. 6). (b) The degree $\ell = 1-6$ surface divergence in a mantle with 3D viscosity $\eta(r, \theta, \phi)/\eta_0 = 1 + \nu(\theta, \phi)$, where $\nu(\theta, \phi)$ is the degree 1–5 viscosity variation in Fig. 25, calculated according to Eq. (151) with $N = 10$. The density perturbations are as in (a). (c) The degree $\ell = 1-6$ surface radial vorticity, with 3D viscosity distribution and density perturbations as in (b), calculated according to Eq. (158) with $N = 10$. In all cases the reference viscosity value is $\eta_0 = 10^{21}$ Pa s. The units on all scale bars are rad/(10 Myr).

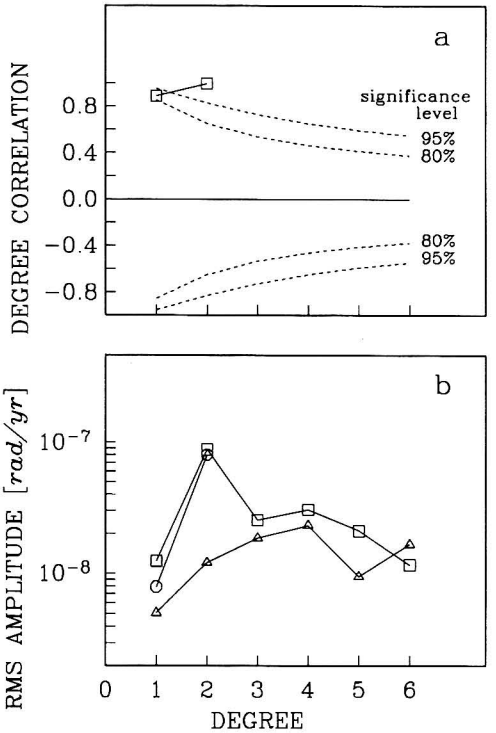

FIG. 27. (a) The cross-correlation, at each degree ℓ, between the predicted divergence fields in Figs. 26a and 26b. (b) The rms amplitude, at each degree ℓ, of the predicted divergence in Fig. 26a (○, divergence, no lateral viscosity), the predicted divergence in Fig. 26b (□, divergence, with lateral viscosity), the predicted vorticity in Fig. 26c (△, vorticity, with lateral viscosity).

A quantitative summary of the buoyancy-induced surface flows in Fig. 26 is presented in Fig. 27. A comparison with Fig. 24 shows clearly that the introduction of shorter-wavelength components in the field of lateral viscosity variations yields a divergence and vorticity spectrum that is "flatter" and thus more closely resembles the observed spectrum in Fig. 4. The effect of higher-degree components in the field of lateral viscosity variations is most dramatic in the case of the radial vorticity field, which possesses a distinctly "red" spectrum in Fig. 24 and a rather "blue" spectrum in Fig. 27.

We have observed that a more realistic field of lateral viscosity variations, as in Fig. 25, acts as a "filter" that may suppress the surface expression of buoyancy-induced flow in the mantle. This behavior was evident from the comparison of Figs. 23b and 26b. The extent to which the viscosity "filters" the mantle flow field depends on the relative alignment of the mantle buoyancy sources and the zones

of weakness and strength in the mantle. This behavior is clearly analogous to the filtering affect of the surface plates, discussed in Section 2 and demonstrated in Fig. 8. We note that the analogy between plates and lateral viscosity variations was indeed confirmed in Section 3.

4.5. Dynamic Surface Topography

In the previous section we observed that lateral viscosity variations in the mantle may have a great impact on the amplitude and spatial pattern of buoyancy-induced flow. We shall now consider to what extent such viscosity variations will affect the flow-induced boundary deflections. The result of this analysis is of great importance because the gravitational field perturbations (e.g., the nonhydrostatic geoid) are known to be very sensitive to the mutually canceling gravitational contributions from flow-induced boundary deflections and the internal buoyancy sources (e.g., Richards and Hager, 1984; Ricard *et al.*, 1984; Forte and Peltier, 1987). It is therefore important to derive flow models that provide realistic (i.e., include all relevant physical effects) boundary deflections.

We shall begin by deriving explicit expressions for the boundary deflections in terms of the buoyancy-induced flow in a laterally heterogeneous fluid shell. We consider first the case of the outer boundary at $r = a$ that separates the overlying inviscid fluid (e.g., the global ocean layer) from the underlying viscous medium (e.g., the mantle). The matching of normal stresses across the undulating outer surface yields [see Eq. (V.8) in Appendix V] the following expression:

$$g_0[\rho_0^+ - \rho_0^-]\delta a = -P_1(a^-) + 2\eta(a^-)\left(\frac{\partial u_r}{\partial r}\right)_{a-} + \rho_0^+\phi_1(a), \quad (161)$$

in which $\delta a(\theta, \phi)$ is the undulation of the boundary relative to its reference location at $r = a$, $\rho_0^+ = \rho_0(a^+)$, $\rho_0^- = \rho_0(a^-)$, and $\rho_0^+\phi_1(a) = P_1(a^+)$ is the nonhydrostatic pressure field in the overlying inviscid fluid arising from self-gravitation. The principal obstacle to be overcome, in the use of Eq. (161), is to obtain an expression for the nonhydrostatic pressure $P_1(a^-)$ in a fluid with lateral viscosity variations. The usual procedure (e.g., Forte and Peltier, 1987) is to consider the horizontal component of the conservation of momentum equation [i.e., Eq. (IV.8) in Appendix IV]. In Appendix VI we present a mathematically efficient derivation of the nonhydrostatic pressure using generalized spherical harmonics and the concept of covariant differentiation, described in Phinney and Burridge (1973). We thus find (see Appendix VI for details) that the spherical harmonic coefficients of the flow-induced surface topography δa_ℓ^m are given by

$$\delta a_\ell^m = \frac{(-1)^m}{g_0(\rho_0^- - \rho_0^+)} \sum_{s,t} \left[6(\Omega_1^s)^2 \left(\frac{1}{r} \frac{dp_s^t}{dr} \right)_{r=a^-} \sum_{J=|\ell-s|,2}^{\ell+s} P_0^J(\ell, m, s, t)\eta_J^{m-t} \right.$$

$$+ \frac{2\Omega_2^s \Omega_1^s \Omega_2^\ell}{\Omega_1^\ell} \left\{ \left(\frac{1}{r} \frac{dp_s^t}{dr} \right)_{r=a^-} \sum_{J=|\ell-s|,2}^{\ell+s} P_2^J(\ell, m, s, t)\eta_J^{m-t} + \iota \left(\frac{q_s^t}{r} \right)_{r=a^-} \right.$$

$$\times \sum_{J=|\ell-s|+1,2}^{\ell+s-1} P_2^J(\ell, m, s, t)\eta_J^{m-t} \Big\} + \frac{\Omega_1^s}{\Omega_1^\ell} \left\{ \left(r \frac{d^3 p_s^t}{dr^3} + \frac{2(\Omega_2^s)^2}{r} \frac{dp_s^t}{dr} \right)_{r=a^-} \right.$$

$$\times \sum_{J=|\ell-s|,2}^{\ell+s} P_1^J(\ell, m, s, t)\eta_J^{m-t} + \iota \left(r \frac{d^2 q_s^t}{dr^2} \right)_{r=a^-}$$

$$\left. \left. \times \sum_{J=|\ell-s|+1,2}^{\ell+s-1} P_1^J(\ell, m, s, t)\eta_J^{m-t} \right\} \right] + \frac{(\phi_1)_\ell^m(a)}{g_0}, \tag{162}$$

in which

$$P_k^J(\ell, m, s, t) = [(2\ell + 1)(2s + 1)(2J + 1)]^{1/2}$$

$$\times \begin{pmatrix} \ell & s & J \\ k & -k & 0 \end{pmatrix} \begin{pmatrix} \ell & s & J \\ -m & t & m - t \end{pmatrix},$$

and the notation $\Sigma_{J=j,2}$ indicates summation over $J = j, j + 2, j + 4, \ldots$. The radial derivatives of the poloidal and toroidal flow scalars in (162) are readily calculated from Eqs. (143), (144), and (149).

The continuity of normal stresses across the lower bounding surface yields, in analogy with Eq. (161), the following expression:

$$g_0[\rho_0^- - \rho_0^+]\delta b = -P_1(b^+) + 2\eta(b^+) \left(\frac{\partial u_r}{\partial r} \right)_{b+} + \rho_0^- \phi_1(b), \tag{163}$$

in which $\delta b(\theta, \phi)$ is the undulation of the lower boundary relative to its undisturbed position at $r = b$, $\rho_0^+ = \rho_0(b^+)$, $\rho_0^- = \rho_0(b^-)$, and $\rho_0^- \phi_1(b) = P_1(b^-)$ is the nonhydrostatic stress field in the underlying inviscid fluid (e.g., the outer core). In analogy with Eq. (162) we then have

$$\delta b_\ell^m = \frac{(-1)^m}{g_0(\rho_0^+ - \rho_0^-)} \sum_{s,t} X_{st}^{\ell m}(b^+) + \frac{(\phi_1)_\ell^m(b)}{g_0}, \tag{164}$$

in which $X_{st}^{\ell m}(b^+)$ is directly obtained by evaluating those terms in Eq. (162) enclosed by square brackets at $r = b^+$ rather than $r = a^-$.

A striking aspect of Eq. (162) is the presence of terms that correspond to toroidal flow. This may seem somewhat surprising, given that toroidal flow does not involve any radial mass flux. The toroidal-flow contribution to surface topography arises from its effect on dynamic pressure P_1, as shown in Eq. (VI.7) in Appendix VI.

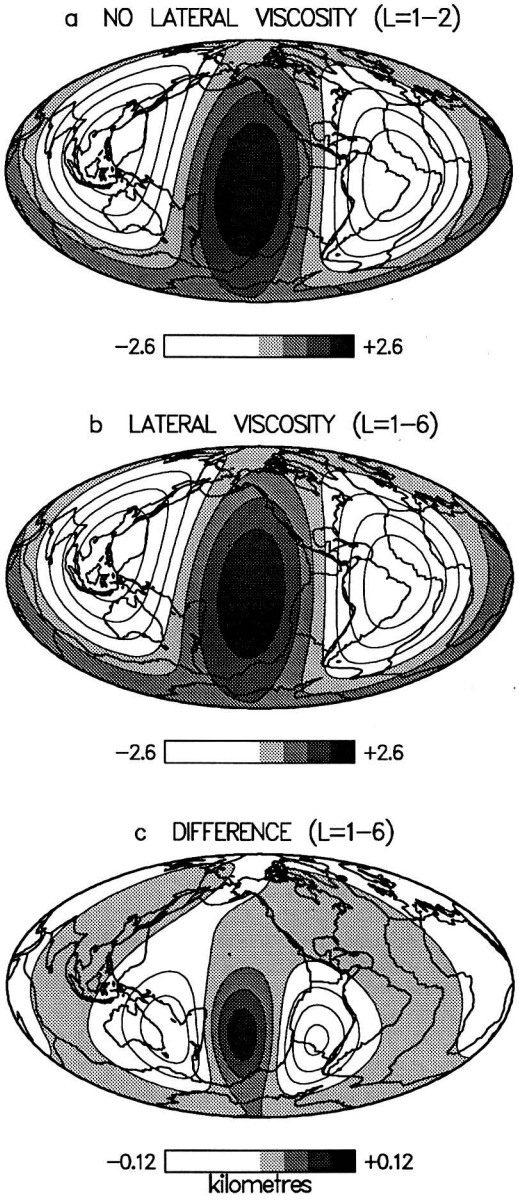

FIG. 28. (a) The degree $\ell = 1-2$ dynamic surface topography in an isoviscous mantle [i.e., $\eta(r, \theta, \phi)/\eta_0 = 1$], calculated according to Eq. (162), due to the degree 1–2 density perturbations derived from model SH8/WM13 (using $\delta \ln \rho/\delta \ln v_s$ in Fig. 6). (b) The degree $\ell = 1-6$ dynamic surface topography in a mantle with 3D viscosity $\eta(r, \theta, \phi)/\eta_0 = 1 + \nu(\theta, \phi)$, where $\nu(\theta, \phi)$ is the degree 1 viscosity variation in Fig. 18, calculated according to Eq. (162). The density perturbations are as in (a). (c) The topography difference, in the range $\ell = 1-6$, obtained by subtracting the topography in (b) from the topography in (a). The units on all scale bars are kilometers.

In the following illustrations of flow-induced surface topography we shall again employ the degree 1–2 field of density perturbations derived from model SH8/WM13 (Woodward *et al.*, 1993) and $\delta \ln \rho / \delta \ln v_s$ in Fig. 6b. The two fields of lateral viscosity variation we shall consider were defined in Eqs. (155) and (160), the former with $x = 0.9$ (thus implying a factor of 19 horizontal variation) and the latter with $x = 0.99$ (implying a factor of 218 horizontal variation). The degree 1 field of lateral viscosity variations is shown in Fig. 18, and the degree 1–5 field of viscosity variations is shown in Fig. 25.

The flow-induced surface topography at $r = a$, for an isoviscous mantle ($\eta_0^0(r) = \eta_0$), is shown in Fig. 28a, in which we observe the clearly dominant degree 2 pattern. The degree 1–6 dynamic topography, which is produced in the presence of the degree 1 field of lateral viscosity variations (again with $\eta_0^0(r) = \eta_0$), is shown in Fig. 28b. It is obvious that the topography in Figs. 28a and 28b are virtually identical, and the relative difference, obtained by subtracting the latter from the former, is indeed quite small as Fig. 28c shows. A quantitative summary of the dynamic topography predictions is presented in Fig. 29. The difference, due

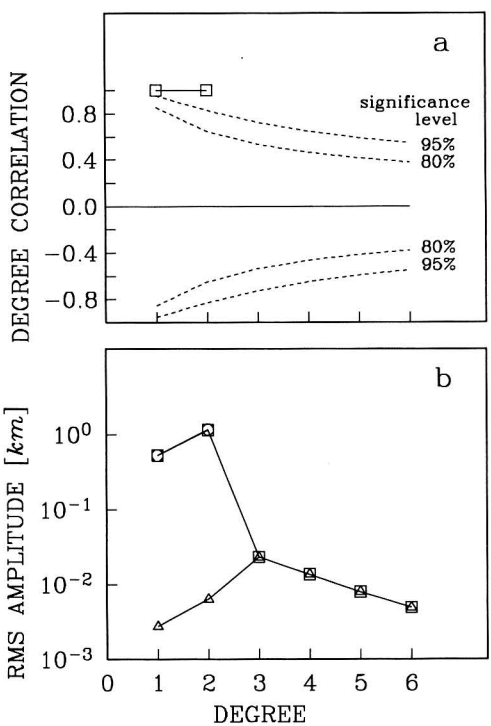

FIG. 29. (a) The cross-correlation, at each degree ℓ, between the predicted topography fields in Figs. 28a and 28b. (b) The rms amplitude, at each degree ℓ, of the predicted dynamic topography in Fig. 28a (○, no lateral viscosity), the predicted dynamic topography in Fig. 28b (□, with lateral viscosity), the topography difference in Fig. 28c (△, difference).

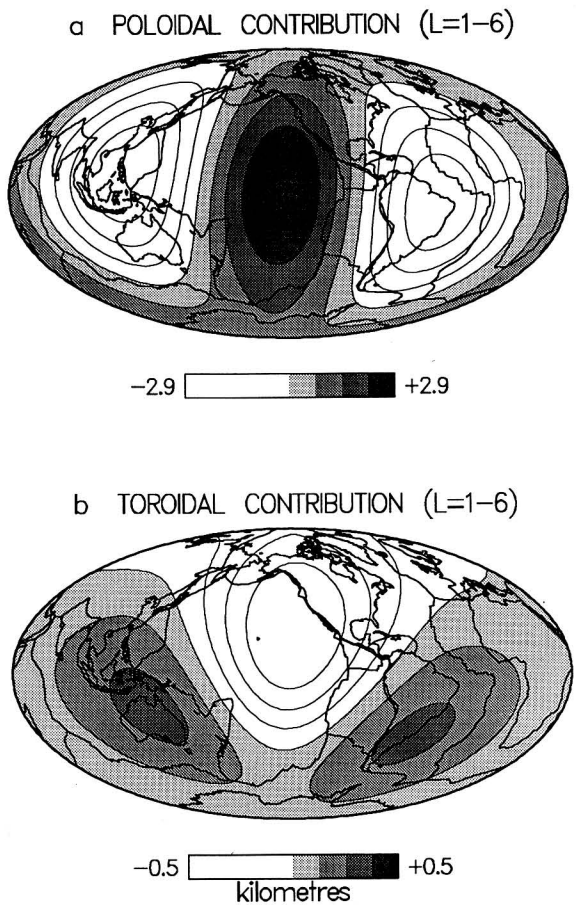

FIG. 30. (a) The degree $\ell = 1-6$ contribution to the dynamic surface topography in Fig. 28b due only to the poloidal mantle flow [calculated by setting $q'_s = 0$ in Eq. (162)]. (b) The degree $\ell = 1-6$ toroidal flow contribution to the dynamic topography in Fig. 28b [calculated by setting $p'_s = 0$ in Eq. (162)]. The superposition of the separate topography contributions in (a) and (b) yields the complete topography shown in Fig. 28b. The units on all scale bars are kilometers.

to the introduction of the degree 1 viscosity variations, is dominated by a degree 3 component with a relative amplitude that is quite small.

In Fig. 30 we consider the separate poloidal and toroidal flow contributions to dynamic topography shown in Fig. 28b. The poloidal contribution is almost a factor of 6 greater than the toroidal contribution. It is, however, clear that had we mistakenly assumed that the toroidal contribution was entirely negligible, then the difference between the topography predictions (with and without lateral viscosity

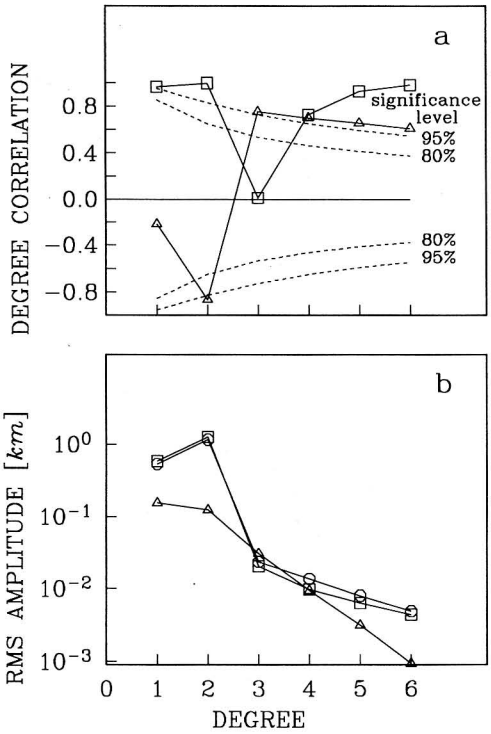

FIG. 31. (a) The cross-correlation, at each degree ℓ, between the dynamic surface topography in Fig. 28b and the poloidal flow contribution in Fig. 30a (□, total poloidal) and the toroidal flow contribution in Fig. 30b (△, total toroidal). (b) The rms amplitude, at each degree ℓ, of the predicted dynamic topography in Fig. 28b (○, total), the separate poloidal flow contribution in Fig. 30a (□, poloidal contribution), the separate toroidal flow contribution in Fig. 30b (△, toroidal contribution).

variations) would have been much larger. A quantitative analysis of the poloidal and toroidal topography contributions is provided in Fig. 31.

The dynamic surface topography produced in the presence of the degree 1–5 field of viscosity variations (again with $\eta_0^0(r) = \eta_0$) is shown in Fig. 32b, along with the isoviscous prediction in Fig. 32a. Here we again have a clear manifestation of the strong insensitivity of dynamic topography to the effects of lateral viscosity variations. The difference between the predictions (with and without lateral viscosity variations) is shown in Fig. 32c. We point out that, although the amplitude of the viscosity variations in the case of Fig. 32b are more than 10 times greater than in the case of Fig. 28b, the relative difference in Fig. 28c increases only slightly from about 5% to 8% in Fig. 32c. A quantitative summary of the topography predictions in Fig. 32 may be found in Fig. 33. It is worth noting that the introduction of shorter-wavelength viscosity variations yields a difference

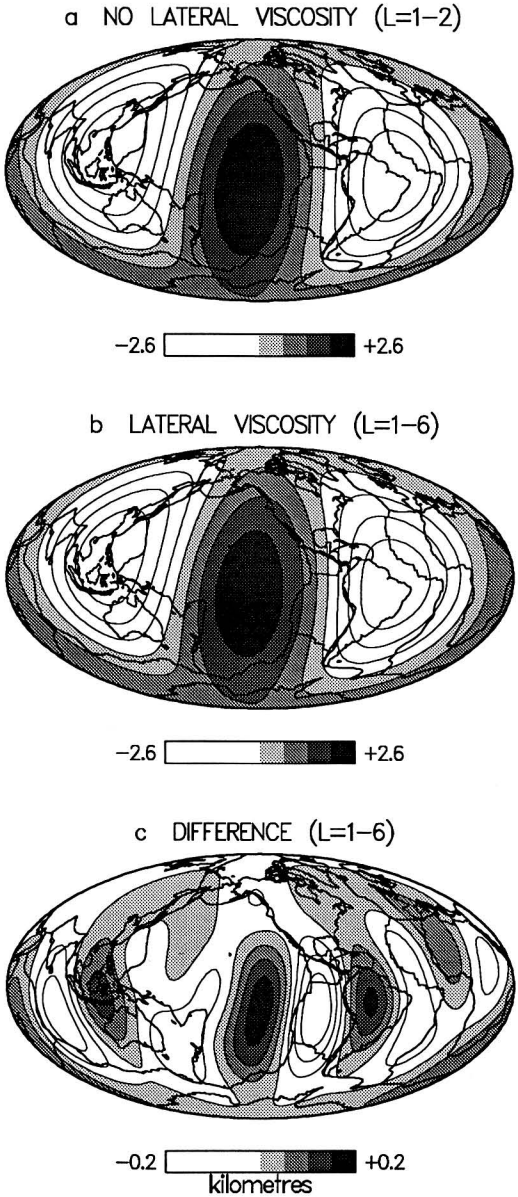

FIG. 32. (a) The degree $\ell = 1-2$ dynamic surface topography in an isoviscous mantle [i.e., $\eta(r, \theta, \phi)/\eta_0 = 1$], calculated according to Eq. (162), due to the degree 1–2 density perturbations derived from model SH8/WM13 [using $\delta \ln \rho/\delta \ln v_s$ in Fig. 6]. (b) The degree $\ell = 1-6$ dynamic surface topography in a mantle with 3D viscosity $\eta(r, \theta, \phi)/\eta_0 = 1 + \nu(\theta, \phi)$, where $\nu(\theta, \phi)$ is the degree 1–5 viscosity variation in Fig. 25, calculated according to Eq. (162). The density perturbations are as in (a). (c) The topography difference, in the range $\ell = 1-6$, obtained by subtracting the topography in (b) from the topography in (a). The units on all scale bars are kilometers.

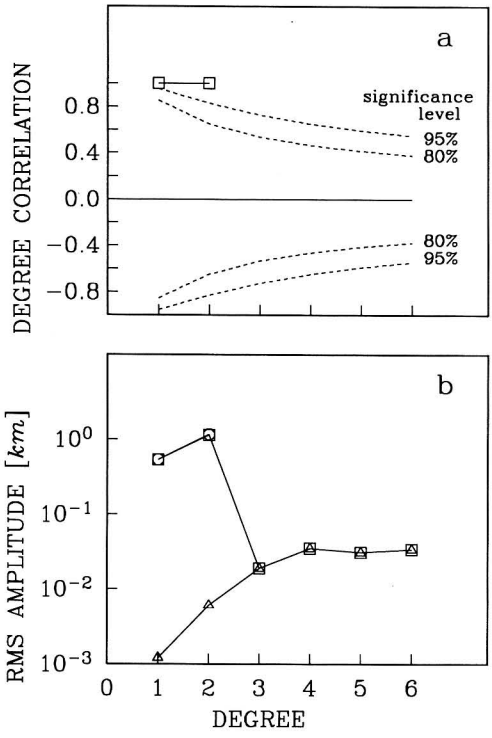

FIG. 33. (a) The cross-correlation, at each degree ℓ, between the dynamic surface topography predictions in Figs. 32a and 32b. (b) The rms amplitude, at each degree ℓ, of the predicted dynamic topography in Fig. 32a (○, no lateral viscosity), the predicted dynamic topography in Fig. 32b (□, with lateral viscosity), the topography difference in Fig. 32c (△, difference).

spectrum that is clearly "blue" and quite different from that displayed in Fig. 29. In Fig. 34 we show the separate poloidal and toroidal flow contributions to the dynamic topography. A comparison of Figs. 30 and 34 shows that the introduction of shorter-wavelength viscosity variations has evidently led to a strong reduction of the toroidal flow contribution while the poloidal flow contribution is relatively unchanged.

We have so far considered only viscosity distributions with a spherically symmetric component that is independent of depth [i.e., $\eta_0^0(r) = \eta_0$]. We now consider the extent to which a depth variation of the horizontally averaged viscosity, when coupled with the depth-invariant lateral viscosity variations in Eq. (160), will affect the dynamic surface topography. We shall consider the following smooth depth increase of the spherically symmetric viscosity:

$$\eta_0^0(r) = \eta_0 \left(\frac{a}{r}\right)^{10}. \tag{165}$$

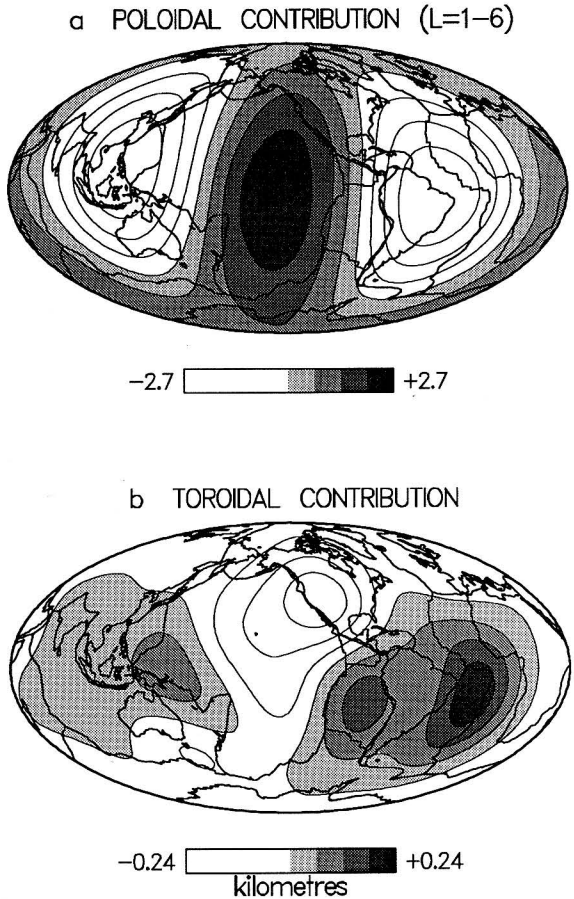

FIG. 34. (a) The degree $\ell = 1-6$ poloidal flow contribution to the dynamic surface topography in Fig. 32b [calculated by setting $q_s^\ell = 0$ in Eq. (162)]. (b) The degree $\ell = 1-6$ toroidal-flow contribution to the dynamic surface topography in Fig. 32b [calculated by setting $p_s^\ell = 0$ in Eq. (162)]. The superposition of the separate topography contributions in (a) and (b) yields the complete topography shown in Fig. 32b. The units on all scale bars are kilometers.

The choice of 10 for the exponent in (165) implies the following depth increases: $\eta_0^0(r_{670})/\eta_0^0(a) \approx 3$, $\eta_0^0(r_{1200})/\eta_0^0(\mathrm{a}) \approx 8$, and $\eta_0^0(r_{\mathrm{CMB}})/\eta_0^0(a) \approx 421$. In Fig. 35a we show the degree 1–2 dynamic surface topography produced in the absence of lateral viscosity variations. A comparison with the isoviscous prediction in Fig. 32a shows that the depth increase of viscosity in (165) leads to a nearly 50% reduction in the amplitude of the surface topography. The flow-induced surface topography generated in the presence of the degree 1–5 viscosity variations is shown in Fig. 35b, and the difference, relative to Fig. 35a, is shown in Fig. 35c. It

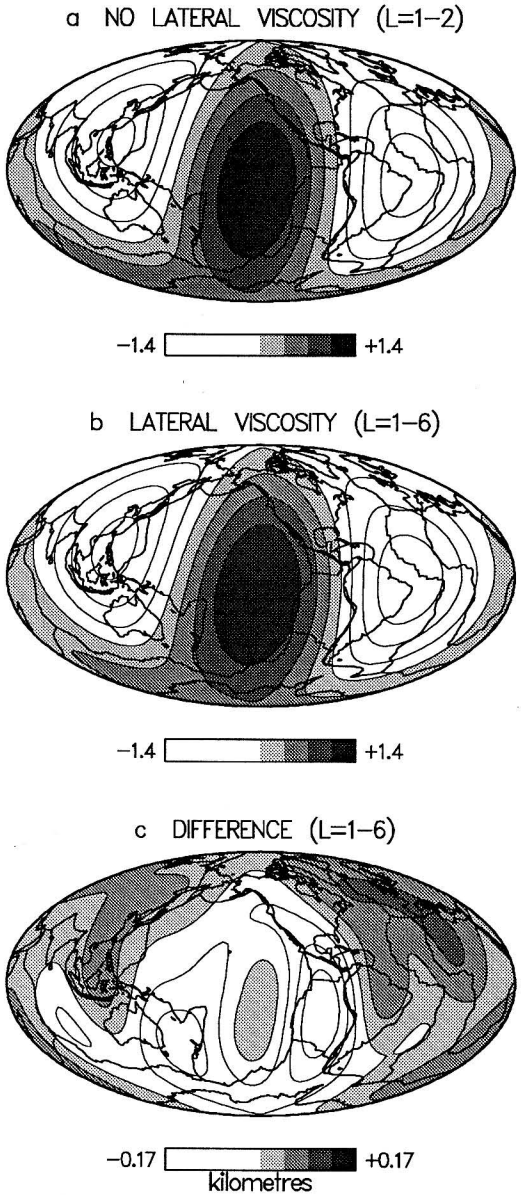

FIG. 35. (a) The degree $\ell = 1-2$ dynamic surface topography in a spherically symmetric mantle with depth-varying viscosity $\eta(r, \theta, \phi)/\eta_0 = (a/r)^{10}$, calculated according to Eq. (162). The degree 1–2 density perturbations employed here are derived from model SH8/WM13 [using $\delta \ln \rho/\delta \ln v_s$ in Fig. 6]. (b) The degree $\ell = 1-6$ dynamic surface topography in a mantle with 3D viscosity $\eta(r, \theta, \phi)/\eta_0 = (a/r)^{10}[1 + \nu(\theta, \phi)]$, where $\nu(\theta, \phi)$ in the degree 1–5 viscosity variation in Fig. 25, calculated according to Eq. (162). The density perturbations are as in (a). (c) The topography difference, in the range $\ell = 1-6$, obtained by subtracting the topography in (b) from the topography in (a). The units on all scale bars are kilometers.

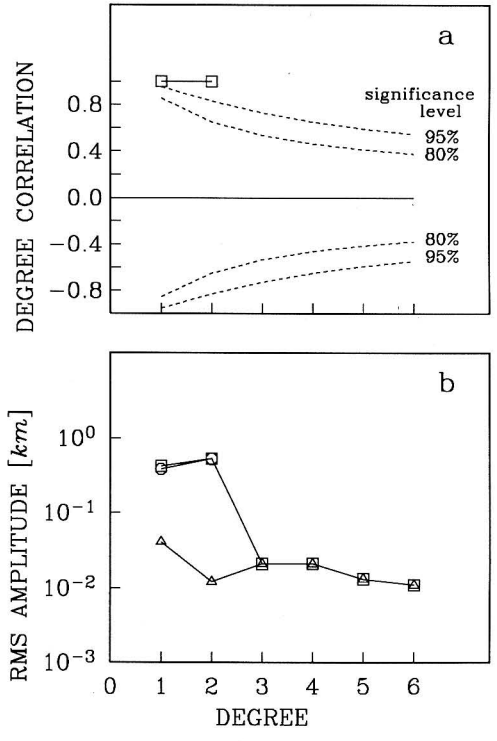

FIG. 36. (a) The cross-correlation, at each degree ℓ, between the dynamic surface topography predictions in Figs. 35a and 35b. (b) The rms amplitude, at each degree ℓ, of the predicted dynamic topography in Fig. 35a (○, no lateral viscosity), the predicted dynamic topography in Fig. 35b (□, with lateral viscosity), the topography difference in Fig. 35c (△, difference).

is important to note that, although the amplitude of the dynamic topography is strongly reduced by depth increases of viscosity, the amplitude of the difference between the predictions (with and without lateral viscosity variations) is almost unchanged. Thus the 8% relative difference in Fig. 32c is increased slightly to 12% in Fig. 35c. In Fig. 36 we provide a quantitative summary of the topography calculations in Fig. 35. We note, in comparison to Fig. 33, that the amplitude of the degree $\ell = 1,2$ differences has substantially increased.

The separate poloidal and toroidal flow contributions to the dynamic surface topography are shown in Fig. 37. Since poloidal flow involves the vertical transport of mass we expect that depth increases of viscosity should more strongly reduce the poloidal contribution to surface topography than the toroidal contribution. This is indeed verified by comparing Figs. 37 and 34.

We have observed that the dynamic topography appears to be remarkably insensitive to even very-large-amplitude horizontal variations of viscosity. This insen-

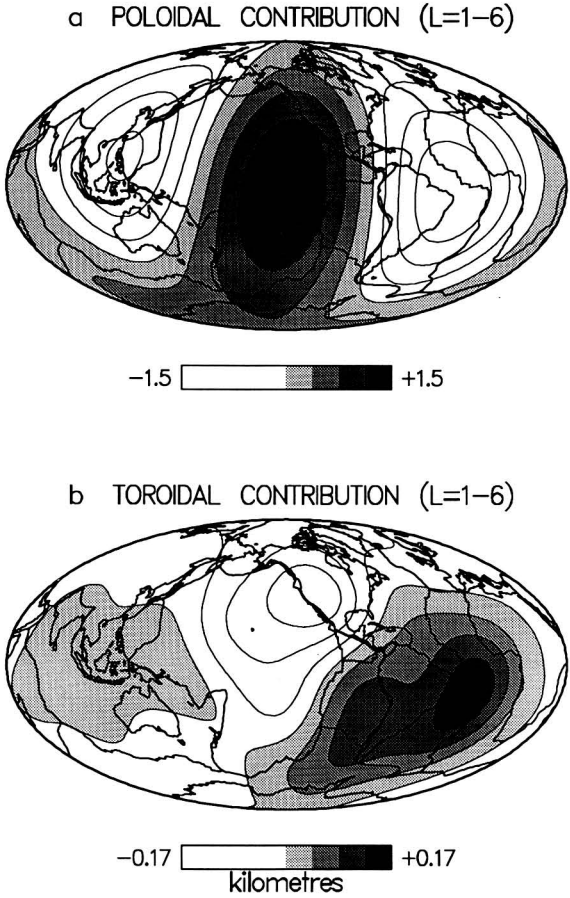

FIG. 37. (a) The degree $\ell = 1-6$ poloidal flow contribution to the dynamic surface topography in Fig. 35b [calculated by setting $q_s^\ell = 0$ in Eq. (162)]. (b) The degree $\ell = 1-6$ toroidal flow contribution to the dynamic surface topography in Fig. 35b [calculated by setting $p_s^\ell = 0$ in Eq. (162)]. The superposition of the separate topography contributions in (a) and (b) yields the complete topography shown in Fig. 35b. The units on all scale bars are kilometers.

sitivity is markedly different from the strong sensitivity of the flow field to lateral viscosity variations (see, e.g., Fig. 26). We may understand this insensitivity of the dynamic topography with the following argument. The buoyancy-induced flow field scales inversely with viscosity, and therefore regions of reduced viscosity correspond to increased flow velocities and vice versa. The normal stresses that deflect the boundaries scale as the product of viscosity and the flow field, and this leads to an effective "cancellation" of the viscosity effect. In regions of increased viscosity the normal stresses would be increased for a given flow, but the

actual flow must itself be reduced in these regions, and consequently the normal stress (and hence the dynamic topography) is relatively unaltered by the lateral viscosity variation. We may also observe this effective cancellation in direct quantitative terms. As shown in (132), degree 1 viscosity variations directly lead to the generation of additional degree $\ell - 1, \ell + 1$ poloidal flow and degree ℓ toroidal flow, by degree ℓ density perturbations. On the other hand, the expression for dynamic topography in (162) implies that the degree 1 viscosity variations will couple the degree $\ell - 1, \ell + 1$ poloidal flows and degree ℓ toroidal flow to degree ℓ topography. Clearly, then, the effective "splitting" of the flow field by lateral viscosity variations is nullified when the "split" flow components are recombined to generate surface deflections.

4.6. Nonhydrostatic Geoid

The gravitational potential perturbations which arise over a convecting mantle are the sum of the potential perturbations due to the internal density perturbations which drive the flow and the potential perturbations due to the flow-induced boundary deflections (e.g., Pekeris, 1935; Richards and Hager, 1984; Ricard *et al.*, 1984; Forte and Peltier, 1987). The surface gravity perturbations are largely controlled by the mutually canceling gravitational contributions from the flow-induced surface topography (at $r = a$) and the internal density anomalies. In the previous section we have observed that while the *depth* variation of mantle viscosity has a strong impact on the amplitude, and hence the gravity effect, of the surface undulations, the presence of very strong *lateral* variations of viscosity has a much smaller impact on the amplitude and pattern of the surface topography. We therefore expect that the nonhydrostatic geoid will show a similar insensitivity to the presence of lateral viscosity variations, and hence be dominantly sensitive only to *radial* viscosity variations. In the following we demonstrate this explicitly. In Appendix VII we provide explicit expressions for the nonhydrostatic geoid in a self-gravitating mantle.

In Fig. 38a we show the $\ell = 2-3$ nonhydrostatic geoid prediction for an isoviscous mantle ($\eta_0^0(r) = \eta_0$), employing the $\ell = 2-3$ density heterogeneity derived from model SH8/WM13 and $\delta \ln \rho / \delta \ln v_s$ in Fig. 6b. The degree 1–6 nonhydrostatic geoid, produced when the $\ell = 2-3$ density anomalies interact with the degree 1–5 viscosity variations in Fig. 25, again with $\eta_0^0(r) = \eta_0$, is shown in Fig. 38b. Apart from a small reduction in the amplitude of the geoid highs in the South Pacific and in southern Africa, Fig. 38b is nearly identical to the isoviscous prediction in Fig. 38a. A map of the difference between these two predictions is presented in Fig. 38c, where we observe that the peak difference is localized in the South Pacific. The rms amplitude of the difference field is 12 m, compared to the rms amplitude of 100 m in Fig. 38a (i.e., the relative effect of the lateral viscosity variations is only 12%). We note that the difference field in Fig. 38c is

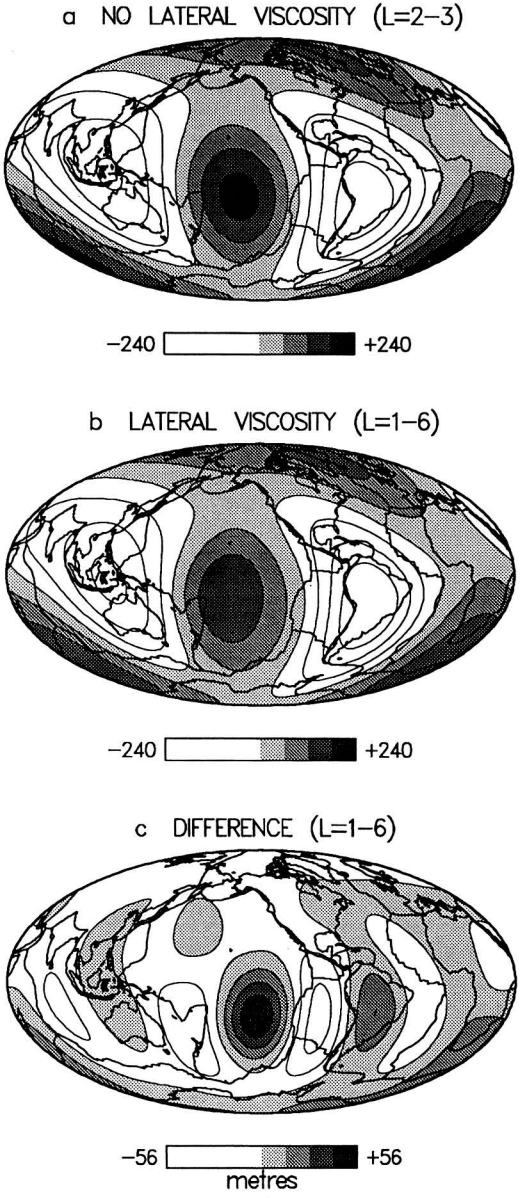

FIG. 38. (a) The degree $\ell = 2-3$ nonhydrostatic geoid prediction for an isoviscous mantle [i.e., $\eta(r, \theta, \phi)/\eta_0 = 1$], calculated on the basis of the degree 2–3 density perturbations derived from model SH8/WM13 [using $\delta \ln \rho/\delta \ln v_s$ in Fig. 6]. (b) The degree $\ell = 1-6$ nonhydrostatic geoid prediction for a mantle with 3D viscosity $\eta(r, \theta, \phi)/\eta_0 = 1 + \nu(\theta, \phi)$, where $\nu(\theta, \phi)$ is the degree 1–5 viscosity variation in Fig. 25. The density perturbations are as in (a). (c) The geoid difference, in the range $\ell = 1-6$, obtained by subtracting the geoid in (b) from that in (a). The units on all scale bars are meters.

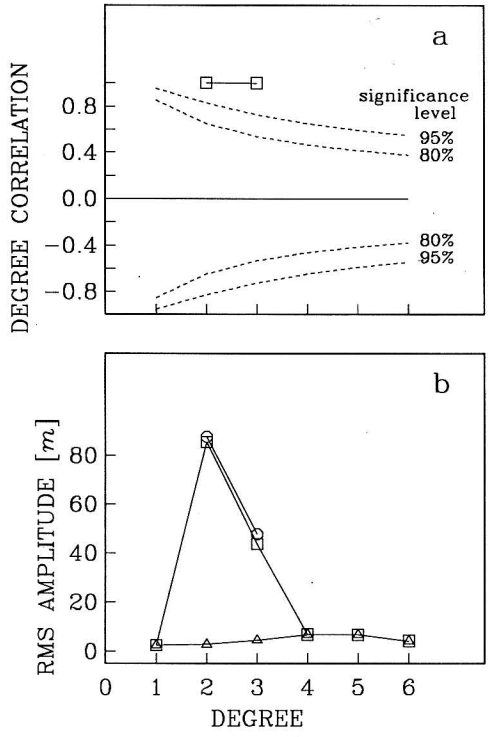

FIG. 39. (a) The cross-correlation, at each degree ℓ, between the nonhydrostatic geoid predictions in Figs. 38a and 38b. (b) The rms amplitude, at each degree ℓ, of the predicted geoid in Fig. 38a (○, no lateral viscosity), the predicted geoid in Fig. 38b (□, with lateral viscosity), the geoid difference in Fig. 38c (△, difference).

largely reflective of the small effect of the lateral viscosity variations on the flow-induced surface topography (see Fig. 32c). A detailed summary of the geoid predictions in Fig. 38 is provided in Fig. 39.

In Fig. 40a we now show the $\ell = 2-3$ nonhydrostatic geoid prediction for a laterally homogeneous viscosity with a depth variation $\eta_0(a/r)^{10}$ given in Eq. (165). This geoid prediction has reversed sign relative to the isoviscous prediction in Fig. 38a because the strong increase of viscosity with depth has strongly reduced the amplitude of the surface topography (compare Figs. 32a and 35a), thus allowing the internal density perturbations to dominate the geoid signal. The degree 1–6 geoid prediction, calculated when the degree 1–5 viscosity variations are introduced [with $\eta_0^0(r) = \eta_0(a/r)^{10}$], is shown in Fig. 40b. Again we observe that the effect of very large lateral variations of viscosity is small, and this is confirmed by the small amplitude of the difference field in Fig. 40c. The

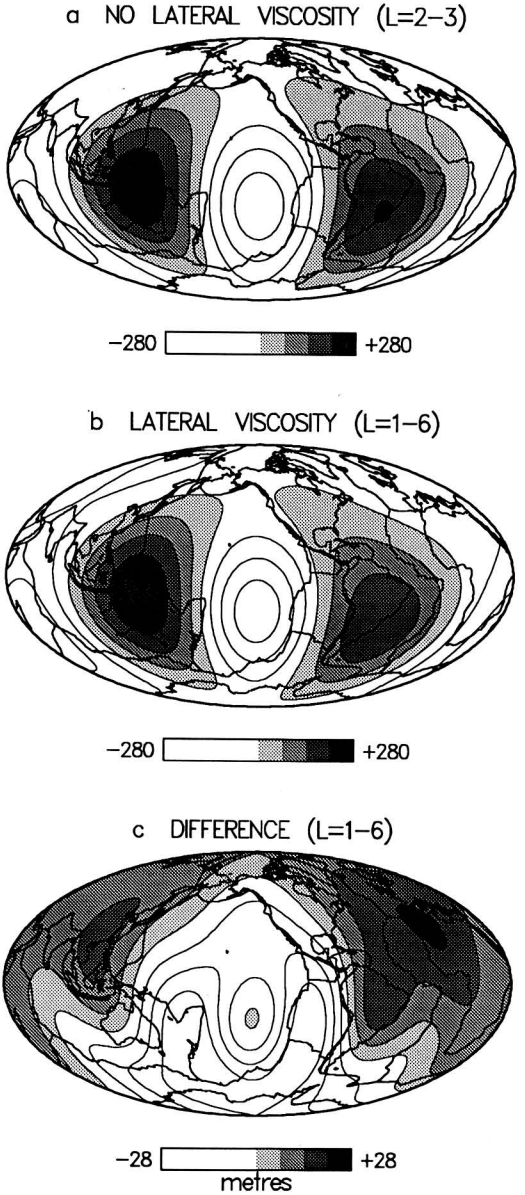

FIG. 40. (a) The degree $\ell = 2-3$ nonhydrostatic geoid prediction for a spherically symmetric mantle with depth-varying viscosity $\eta(r, \theta, \phi)/\eta_0 = (a/r)^{10}$, calculated on the basis of the degree 2–3 density perturbations derived from model SH8/WM13 (using $\delta \ln \rho/\delta \ln v_s$ in Fig. 6). (b) The degree $\ell = 1-6$ nonhydrostatic geoid prediction for a mantle with 3D viscosity $\eta(r, \theta, \phi)/\eta_0 = (a/r)^{10}[1 + \nu(\theta, \phi)]$, where $\nu(\theta, \phi)$ is the degree 1–5 viscosity variation in Fig. 25. The density perturbations are as in (a). (c) The geoid difference, in the range $\ell = 1-6$, obtained by subtracting the geoid in (b) from that in (a). The units on all scale bars are meters.

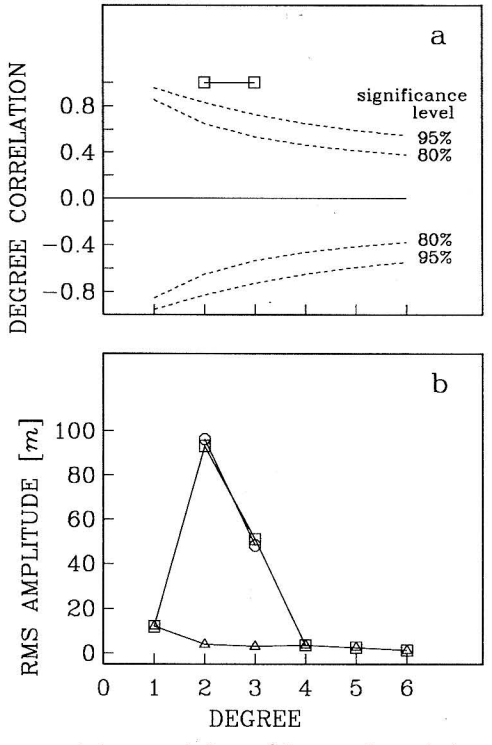

FIG. 41. (a) The cross-correlation, at each degree ℓ, between the nonhydrostatic geoid predictions in Figs. 40a and 40b. (b) The rms amplitude, at each degree ℓ, of the predicted geoid in Fig. 40a (○, no lateral viscosity), the predicted geoid in Fig. 40b (□, with lateral viscosity), the geoid difference in Fig. 40c (△, difference).

rms amplitude of this difference field is 14 m, compared to the rms amplitude of 108 m in Fig. 40a (i.e. a relative difference of only 13%). We again note that the difference field in Fig. 40c is a reflection of the small effect of lateral viscosity variations on the flow-induced surface topography (see Fig. 35c). A quantitative summary of the geoid predictions in Fig. 40 is provided in Fig. 41.

When considering the conclusions obtained in this section, and in Section 4.5, it is worth recalling that all our demonstrations have employed idealized *depth-independent* lateral viscosity variations. It is our expectation that the imposition of the large-amplitude lateral variations in Fig. 23, at all depths in the mantle, probably overestimates the large-scale variations that actually exist, especially in the deep mantle (e.g., Zhang and Christensen, 1993). The final confirmation of our conclusions will be possible when we can reliably map the amplitude of lateral viscosity variations throughout the mantle. Encouraging progress is now being made thanks to recent high-pressure melting experiments (Zerr and Boehler,

1993) and also as a result of recent inferences of lateral variations of seismic Q in the deep mantle (Romanowicz and LeStunff, 1993).

4.7. Differential Rotation in the Mantle

In Section 3.2 we pointed out that a degree 1 toroidal flow field in the mantle implies that any infinitesimally thick spherical shell at radius r will rotate, as a rigid body, with angular velocity given by Eq. (79). In a mantle with spherically symmetric viscosity (and free-slip boundary conditions) the angular velocity is constant with depth, and thus the entire mantle rotates as a rigid body. This rigid-body rotation is a degenerate solution of the governing flow equations, and it may be eliminated by transferring to a new frame of reference. This degeneracy is also removed by introducing lateral viscosity variations. We have seen that lateral viscosity variations, distributed throughout the mantle, may produce buoyancy-induced toroidal flow with magnitude comparable to the poloidal flow. In particular, the degree 1 toroidal flow will imply a depth-varying net rotation within the mantle. As emphasized in Section 3.2, this differential rotation of the mantle will be significant only if the lateral viscosity variations are distributed over a sufficiently large depth interval.

The most visible manifestation of net rotation within the mantle is provided by the degree 1 toroidal-flow component of the tectonic plate motions. In Fig. 42a we show the degree 1 radial vorticity derived from the Minster and Jordan (1978) absolute plate-motion model (AM1-2) based on the hotspot reference frame. This figure clearly illustrates the dominant east–west lithosphere rotation. In Fig. 42b we show the degree 1 component of the buoyancy-induced radial vorticity field in Fig. 26c. The predicted net rotation of the lithosphere in Fig. 42b agrees rather well with the observed net-rotation of the plates in Fig. 42a. This agreement suggests that the hotspot reference frame may indeed be dynamically plausible since it yields absolute plate motions (i.e. net rotation) that are readily explained by the interaction of large-scale buoyancy-induced flow with large-scale lateral viscosity variations (e.g., in Fig. 25).

The explicit expressions for flow throughout the mantle, given by Eq. (123), allow us to readily describe the depth-varying net rotation in the mantle. The degree 1 toroidal mantle flow, given by Eq. (144), arising from the interaction of degree 1–2 density perturbations with degree 1–5 viscosity variations (Fig. 25) is illustrated in Fig. 43. The depth variation of the net-rotation vector components $\omega_x(r)$, $\omega_y(r)$, $\omega_z(r)$ is calculated on the basis of expression (79). The surface rotation $\omega_x(r = a)$, $\omega_y(r = a)$, $\omega_z(r = a)$ is of course identical to the degree 1 toroidal flow in Fig. 42b. It is clear from Fig. 43 that there is essentially no differential rotation between the lithosphere and adjacent underlying mantle, as we pointed out in Section 3.2. The net rotation within the mantle changes significantly below a depth of about 1400 km. Near a depth of 1700 km the net rotation vanishes and

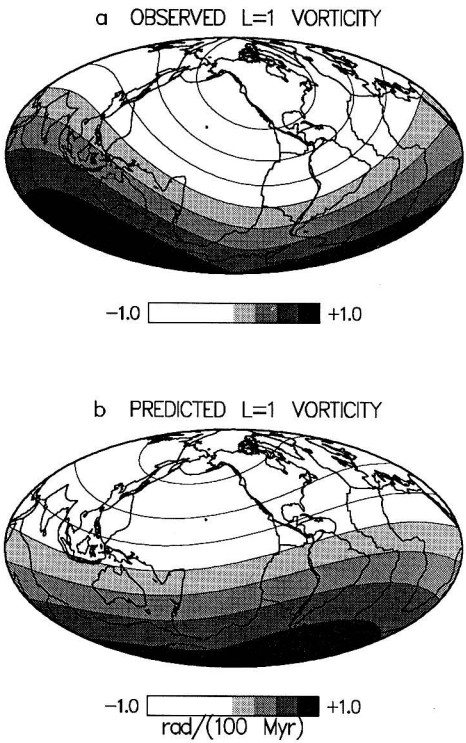

FIG. 42. (a) The degree $\ell = 1$ radial vorticity of the tectonic plate velocities (Forte and Peltier, 1987) derived from absolute-motion model AM1–2 of Minster and Jordan (1978), which is based on the hotspot reference frame. (b) The degree $\ell = 1$ component of the predicted buoyancy-induced surface radial vorticity shown in Fig. 26c. The units on all scale bars are rad/(100 Myr).

changes sign, resulting in striking contra-rotation of the lower 1000 km of the mantle relative to the top 1000 km of the mantle. We also note that net rotation in the mantle appears to be dominantly in the $\hat{z}$ direction (i.e., along the Earth's rotation axis).

It is interesting to note that the net rotation in the mantle, arising from the degree 1 toroidal flow, also carries a nonvanishing angular momentum. The contribution to the Earth's angular momentum, from flow in the mantle, is given by the general expression

$$\mathbf{L}_{\text{mantle flow}} = \int_V \mathbf{r} \times \mathbf{v}\, \rho\, dV, \tag{166}$$

in which $\mathbf{v}$ is the mantle flow velocity and V denotes integration over the volume of the mantle. It may be shown that the angular momentum in Eq. (166) will vanish for all poloidal flows and all toroidal flows, except for the degree 1 toroidal flow [we assume that the density distribution is essentially spherically symmetric:

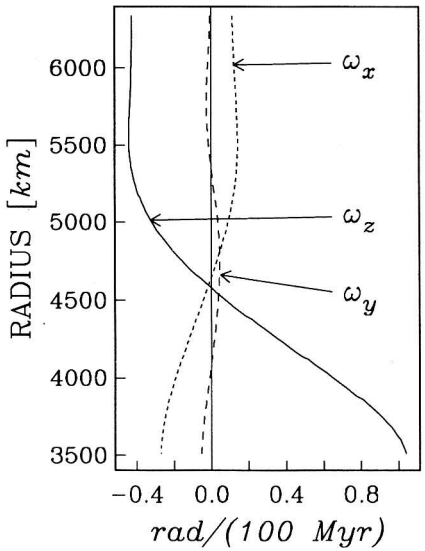

FIG. 43. The depth variation of the net rotation in the mantle, corresponding to the degree $\ell = 1$ toroidal flow in the mantle, as given by Eq. (79). The degree 1 toroidal flow, calculated according to Eq. (144), is due to the interaction of degree 1–2 density perturbations [derived from model SH8/WM13 using $\delta \ln \rho/\delta \ln v_s$ in Fig. 6] with the 3D viscosity $\eta(r, \theta, \phi)/\eta_0 = 1 + \nu(\theta, \phi)$, where $\nu(\theta, \phi)$ is the degree 1–5 viscosity variation in Fig. 25. The reference viscosity value is $\eta_0 = 10^{21}$ Pa s.

$\rho = \rho_0(r)$]. The angular momentum associated with the degree 1 toroidal flow may be shown to be (algebraic details omitted here):

$$\mathbf{L}_{\text{mantle flow}} = \frac{8\pi}{3} \int_b^a \rho_0(r)[\omega_x(r)\hat{\mathbf{x}} + \omega_y(r)\hat{\mathbf{y}} + \omega_z(r)\hat{\mathbf{z}}]r^4 \, dr. \tag{167}$$

Equation (167) provides the basis for the following definition of the "effective" average rotation rate of the mantle:

$$\langle \omega_i \rangle = \frac{\int_b^a \rho_0(r)\omega_i(r)r^4 dr}{\int_b^a \rho_0(r)r^4 dr}. \tag{168}$$

On the basis of the rotation rates in Fig. 43, we thus obtain

$$\langle \omega_x \rangle = \frac{0.15 \text{ rad}}{100 \text{ Myr}}, \qquad \langle \omega_y \rangle = \frac{-0.004 \text{ rad}}{100 \text{ Myr}},$$

$$\langle \omega_z \rangle = \frac{-0.52 \text{ rad}}{100 \text{ Myr}}.$$

5. Conclusion

In this chapter we have considered three different approaches to the treatment of the effects of lateral viscosity variations in the Earth's mantle. The first and simplest approach is based on the assumption that the tectonic plates are the most extreme, and hence, only important manifestation of lateral rheology variations. It is therefore possible to characterize the effect of surface plates only in terms of their geometry and thus circumvent on explicit treatment of lateral viscosity variations. The requirement that instantaneous plate motions be described by rigid-body rotations imposes a partitioning of the internal density perturbations $\delta\rho(r, \theta, \phi)$ into two orthogonal components; $\delta\rho = \delta\hat{\rho} + \delta\bar{\rho}$. The component $\delta\hat{\rho}(r, \theta, \phi)$ produces mantle flow whose surface pattern exactly corresponds to a permitted combination of rigid-body rotation of the individual plates. The component $\delta\bar{\rho}(r, \theta, \phi)$ instead produces surface flow that is completely inconsistent with rigid-body rotations of the plates and therefore "sees" a no-slip surface boundary (i.e., the plates are "locked" and immobile). We emphasized that this partitioning of internal buoyancy sources renders the interpretation of observed plate motions completely nonunique. Clearly, the observed plate motions reflect only the buoyancy-induced flow arising from $\delta\hat{\rho}$ and tell us nothing about the internal flow excited by $\delta\bar{\rho}$. An important illustration of the consequences of this nonuniqueness was provided in Fig. 14, where we showed that plate motions, arising from buoyancy sources only beneath midoceanic ridges or only confined to regions beneath subduction zones, provide equally good matches to the observed plate motions. This geometric treatment of the surface plates also provided us with an explicit expression [Eqs. (34)–(35)] for the coupling of the poloidal and toroidal components of the plate motions. This relationship demonstrates that the equipartitioning of kinetic energy between poloidal and toroidal plate velocities depends on the plate geometries.

Although this geometric treatment of surface plates is attractive, owing to its ease of implementation, it entirely ignores the flow dynamics and the rheological properties of the lithosphere. A lithospheric plate cannot be wholly rigid, as assumed in the geometric treatment, and it must become progressively more deformable (i.e., less viscous on average) with increasing depth. In addition, the zones of weakness at plate boundaries must have some finite horizontal extent rather than being mathematically infinitesimal as is implicit in the geometric treatment.

If we assume that the lateral variations of viscosity in the sublithospheric mantle are negligible compared to those in the lithosphere, it is then possible to formulate an inverse problem for the lateral variations of viscosity in the lithosphere that are consistent with the observed tectonic plate velocities. The inferred viscosity variations in the lithosphere (Fig. 15) clearly show an overall pattern of weak plate boundaries and strong plate interiors. Our inferences suggest, however, that not

all plate boundaries are equally weak and that a purely thermal interpretation may not be valid. The East Pacific rise is a zone of rapid divergence with very high surface heat flux, and therefore we might expect that it would be a prominent low-viscosity region. Similarly, the subduction zones in the northwest Pacific are presumably colder than average and therefore should be stiffer than average (again, assuming a purely thermal origin for viscosity variations). Instead we observed that the lithosphere is softer than average in the subduction zones and that the most prominent zone of weakness appears to be on the plate boundary in western North America. This suggests that nonlinear effects (i.e., strain-induced softening) are important for understanding lateral variations of viscosity in the lithosphere.

The lateral variations of effective viscosity may indeed be strongest in the lithosphere but the global-scale models of seismic velocity heterogeneity in the mantle suggest that very-long-wavelength variations of viscosity will be significant throughout the mantle. We have shown that a physically elegant, and mathematically efficient, procedure for modeling the effects of 3D viscosity variations in spherical fluid shells is provided by a variational treatment of the momentum conservation equation. This variational treatment is based on the result (proved in Section 4.1) that the difference between the rate of viscous dissipation of energy and the rate of energy released by buoyancy is an absolute minimum. This minimum principle yields a quasianalytic formulation of buoyancy-induced flow that explicitly describes the coupling of both poloidal and toroidal flows to internal density perturbations by lateral viscosity variations. We have employed this variational formulation to show that long-wavelength lateral viscosity variations in the mantle have a strong effect on the buoyancy-induced flow field. Toroidal flow is excited with a strength that is less than, but comparable to, the poloidal flow. We find that the net rotation of the lithosphere, given by absolute plate-motion models employing the hotspot reference frame, is readily explained by the interaction of very-long-wavelength buoyancy-induced flow with lateral viscosity variations that are correlated to the seismically inferred mantle heterogeneity.

An important outcome of our investigation of the effects of 3D viscosity heterogeneity is the observation that lateral viscosity variations have a rather small effect on flow-induced boundary topography and hence the nonhydrostatic geoid. We find that even if the viscosity varies laterally by two orders of magnitude, the relative difference between the geoid predicted with and without these lateral viscosity variations is only of order 12%. We conclude from this that the nonhydrostatic geoid is overwhelmingly sensitive to *radial* viscosity variations and is much less sensitive to lateral viscosity variations. This result is very important because it suggests that previous geoid-derived inferences of radial viscosity variation in the mantle, based on the seismically inferred density models, will not be biased by the neglect of lateral viscosity variations. A 12% error is essentially negligible, when compared to the much larger uncertainties in the current seismic inferences of 3D mantle heterogeneity.

ACKNOWLEDGMENTS

This work represents the result of a long-term research effort spanning the period 1989–1992. A.M.F. is grateful for the financial support provided by a Canadian NSERC postdoctoral fellowship and for the continued support through NSERC grant A9627 to W.R.P. Support at Harvard University has been provided by NSF grants EAR90-05013 and EAR92-05390. We thank two anonymous reviewers for constructive comments and suggestions. A.M.F. also wishes to thank Adam Dziewonski, Rick O'Connell, Robert Woodward, and Wei-jia Su for useful discussions.

APPENDIX I.
HORIZONTAL GRADIENTS OF SPHERICAL HARMONIC FUNCTIONS

We derive here explicit expressions for the following horizontal gradients of the scalar spherical harmonic functions $Y_\ell^m(\theta, \phi)$:

$$\nabla_1 Y_\ell^m(\theta, \phi) = \hat{\boldsymbol{\theta}} \frac{\partial}{\partial \theta} Y_\ell^m(\theta, \phi) + \hat{\boldsymbol{\phi}} \frac{1}{\sin \theta} \frac{\partial}{\partial \phi} Y_\ell^m(\theta, \phi) \tag{I.1}$$

$$\Lambda Y_\ell^m(\theta, \phi) \equiv \hat{\boldsymbol{r}} \times \nabla_1 Y_\ell^m(\theta, \phi)$$

$$= -\hat{\boldsymbol{\theta}} \frac{1}{\sin \theta} \frac{\partial}{\partial \phi} Y_\ell^m(\theta, \phi) + \hat{\boldsymbol{\phi}} \frac{\partial}{\partial \phi} Y_\ell^m(\theta, \phi) \tag{I.2}$$

The operations ∇_1 (i.e., horizontal gradient on a unit sphere) and Λ [$-\iota \Lambda$ is the quantum-mechanical angular momentum operator (e.g. Backus, 1958)] appear repeatedly in formulations of elasticity and hydrodynamic theory in spherical geometry. Rather unwieldy expressions for (I.1) and (I.2) may be found in Morse and Feshbach (1953, p. 1899). We shall find it most useful to obtain expressions for (I.1) and (I.2) in terms of a special combination of fixed Cartesian basis vectors. The expressions derived below will be employed often in the main text and in the following Appendixes.

From Edmonds (1960, Eq. [5.9.17]) we obtain the result

$$\nabla_1 Y_\ell^m = \ell \sqrt{\frac{\ell + 1}{2\ell + 1}} \mathbf{Y}_{\ell\ell+1}^m + (\ell + 1) \sqrt{\frac{\ell}{2\ell + 1}} \mathbf{Y}_{\ell\ell-1}^m, \tag{I.3}$$

in which we have two special cases of general vector spherical harmonics (Edmonds, 1960, Eq. [5.9.10]) which we write as

$$\mathbf{Y}_{\ell n}^m = \sum_{q=-1}^{1} Y_n^{m-q}(n\ m - q;\ 1\ q \mid \ell m) \hat{\boldsymbol{e}}_q, \tag{I.4}$$

in which $\hat{\boldsymbol{e}}_q$ are the unit polarization vectors (Edmonds, 1960, Eq. [5.9.4]) defined as

$$\hat{\boldsymbol{e}}_{+1} = -\frac{1}{\sqrt{2}}(\hat{\boldsymbol{x}} + \imath\hat{\boldsymbol{y}}), \qquad \hat{\boldsymbol{e}}_{0} = \hat{\boldsymbol{z}}, \qquad \hat{\boldsymbol{e}}_{-1} = \frac{1}{\sqrt{2}}(\hat{\boldsymbol{x}} - \imath\hat{\boldsymbol{y}}), \tag{I.5}$$

where $\imath = \sqrt{-1}$, $\hat{\boldsymbol{x}}, \hat{\boldsymbol{y}}, \hat{\boldsymbol{z}}$ are the unit basis vectors in a rectangular Cartesian frame of reference, and the $(n\ m - q;\ 1\ q \mid \ell m)$ are the Clebsch-Gordon coefficients that define the coupling between degree $\ell=1$ and degree $\ell=n$. Using (I.4) we then have that

$$\begin{aligned}\mathbf{Y}^{m}_{\ell\ell+1} = {} & Y^{m+1}_{\ell+1}(\ell + 1\ m + 1;\ 1\ -\ 1 \mid \ell m)\hat{\boldsymbol{e}}_{-1} \\ & + Y^{m}_{\ell+1}(\ell + 1\ m;\ 1\ 0 \mid \ell m)\hat{\boldsymbol{e}}_{0} \\ & + Y^{m-1}_{\ell+1}(\ell + 1\ m - 1;\ 1\ 1 \mid \ell m)\hat{\boldsymbol{e}}_{1},\end{aligned} \tag{I.6}$$

and

$$\begin{aligned}\mathbf{Y}^{m}_{\ell\ell-1} = {} & Y^{m+1}_{\ell-1}(\ell - 1\ m + 1;\ 1\ -\ 1 \mid \ell m)\hat{\boldsymbol{e}}_{-1} \\ & + Y^{m}_{\ell-1}(\ell - 1\ m;\ 1\ 0 \mid \ell m)\hat{\boldsymbol{e}}_{0} \\ & + Y^{m-1}_{\ell-1}(\ell - 1\ m - 1;\ 1\ 1 \mid \ell m)\hat{\boldsymbol{e}}_{1},\end{aligned} \tag{I.7}$$

Explicit expressions for the Clebsch–Gordon coefficients in (I.6) and (I.7) may be found in Condon and Shortley (1963, p. 76). Inserting (I.6) and (I.7) into (I.3) we obtain

$$\begin{aligned}\boldsymbol{\nabla}_1 Y^{m}_{\ell} = {} & \frac{\hat{\boldsymbol{e}}_{-1}}{\sqrt{2}}(\ell c^{m}_{\ell} Y^{m+1}_{\ell+1} + (\ell + 1)c^{-m-1}_{\ell-1} Y^{m+1}_{\ell-1}) \\ & - \hat{\boldsymbol{e}}_{0}(\ell b^{m}_{\ell} Y^{m}_{\ell+1} - (\ell + 1)b^{m}_{\ell-1} Y^{m}_{\ell-1}) \\ & + \frac{\hat{\boldsymbol{e}}_{1}}{\sqrt{2}}(\ell c^{-m}_{\ell} Y^{m-1}_{\ell+1} + (\ell + 1)c^{m-1}_{\ell-1} Y^{m-1}_{\ell-1}),\end{aligned} \tag{I.8}$$

where

$$c^{m}_{\ell} = \left[\frac{(\ell + m + 2)(\ell + m + 1)}{(2\ell + 1)(2\ell + 3)}\right]^{1/2} \quad \text{and}$$

$$b^{m}_{\ell} = \left[\frac{(\ell - m + 1)(\ell + m + 1)}{(2\ell + 1)(2\ell + 3)}\right]^{1/2}. \tag{I.9}$$

Since $\boldsymbol{\Lambda} = \imath\mathbf{L}$, where $\mathbf{L}$ is the quantum-mechanical angular momentum operator, we then obtain from Edmonds (1960, Eq. [5.9.14]) the result

$$\boldsymbol{\Lambda}\ \mathbf{Y}^{m}_{\ell} = \imath\sqrt{\ell(\ell + 1)}\ \mathbf{Y}^{m}_{\ell\ell}. \tag{I.10}$$

Employing (I.4), we write (I.10) as

$$\begin{aligned}\mathbf{\Lambda} Y_\ell^m = \iota\sqrt{\ell(\ell+1)}\,[&Y_\ell^{m+1}(\ell m+1;\,1\,-1\mid \ell m)\hat{\boldsymbol{e}}_{-1}\\ &+ Y_\ell^m(\ell m;\,1\,0\mid \ell m)\hat{\boldsymbol{e}}_0 + Y_\ell^{m-1}(\ell m-1;\,1\,1\mid \ell m)\hat{\boldsymbol{e}}_1].\end{aligned} \tag{I.11}$$

Explicit expressions for the Clebsch-Gordon coefficients in (I.11) may again be found in Condon and Shortley (1963, p. 76) and we finally write (I.11) as

$$\mathbf{\Lambda} Y_\ell^m = \iota\left[\frac{\hat{\boldsymbol{e}}_{-1}}{\sqrt{2}}\,a_\ell^m Y_\ell^{m+1} + \hat{\boldsymbol{e}}_0 m Y_\ell^m - \frac{\hat{\boldsymbol{e}}_1}{\sqrt{2}}\,a_\ell^{-m} Y_\ell^{m-1}\right], \tag{I.12}$$

where

$$a_\ell^m = [(\ell - m)\,(\ell + m + 1)]^{1/2}. \tag{I.13}$$

For completeness we also derive the expression for $\hat{\boldsymbol{r}}\,Y_\ell^m(\theta,\phi)$ [equivalent to the vector harmonic $\mathbf{P}_{mn}(\theta,\phi)$ in Morse and Feshbach (1953, p. 1898)] where $\hat{\boldsymbol{r}}$ is the unit vector along the radius. From Edmonds (1960, Eq. [5.9.16]) we have

$$\hat{\boldsymbol{r}}\,Y_\ell^m = -\sqrt{\frac{\ell+1}{2\ell+1}}\,\mathbf{Y}_{\ell\ell+1}^m + \sqrt{\frac{\ell}{2\ell+1}}\,\mathbf{Y}_{\ell\ell-1}^m. \tag{I.14}$$

Using (I.6) and (I.7), and following the derivation which led to (I.8), we obtain

$$\begin{aligned}\hat{\boldsymbol{r}}\,Y_\ell^m = &-\frac{\hat{\boldsymbol{e}}_{-1}}{\sqrt{2}}\,(-c_\ell^m Y_{\ell+1}^{m+1} + c_{\ell-1}^{-m-1} Y_{\ell-1}^{m+1})\\ &+ \hat{\boldsymbol{e}}_0(b_\ell^m Y_{\ell+1}^m + b_{\ell-1}^m Y_{\ell-1}^m)\\ &+ \frac{\hat{\boldsymbol{e}}_1}{\sqrt{2}}\,(-c_\ell^{-m} Y_{\ell+1}^{m-1} + c_{\ell-1}^{m-1} Y_{\ell-1}^{m-1})\end{aligned} \tag{I.15}$$

The complex basis vectors $\hat{\boldsymbol{e}}_q$ in (I.8), (I.12) and (I.15) have the following useful orthogonality property (Edmonds, 1960, Eq. [5.9.7]):

$$\hat{\boldsymbol{e}}_q^* \cdot \hat{\boldsymbol{e}}_{q'} = \delta_{qq'}, \tag{I.16}$$

where the asterisk denotes complex conjugation.

Expressions (I.8) and (I.12) are particularly useful when $\mathbf{\nabla}_1 Y_\ell^m$ and $\mathbf{\Lambda} Y_\ell^m$ are integrated or differentiated over a spatial domain because the basis vectors $\hat{\boldsymbol{e}}_q$ are constant and therefore unaffected by these operations.

APPENDIX II. Spherical Harmonic Coupling Rules

We shall summarize here the principal results, concerning the coupling of two scalar spherical harmonics, which will be often employed in the main text. We

shall also describe a technique, based on the elegant formalism of LeBlanc (1986, 1987), which permits the direct and rapid numerical computation of any given spherical harmonic coupling coefficient.

From the classical theory of angular momentum coupling in quantum mechanics we have the following basic result (e.g., Edmonds, 1960, Eq. [4.6.5]):

$$Y_{\ell_1}^{m_1}(\theta, \phi) Y_{\ell_2}^{m_2}(\theta, \phi) = \sum_{\ell=|\ell_1-\ell_2|}^{\ell_1+\ell_2} \begin{bmatrix} m_1 & m_2 & m \\ \ell_1 & \ell_2 & \ell \end{bmatrix} Y_\ell^m(\theta, \phi)^*, \tag{II.1}$$

where

$$\begin{bmatrix} m_1 & m_2 & m \\ \ell_1 & \ell_2 & \ell \end{bmatrix} = [(2\ell_1 + 1)(2\ell_2 + 1)(2\ell + 1)]^{1/2} \begin{pmatrix} \ell_1 & \ell_2 & \ell \\ 0 & 0 & 0 \end{pmatrix} \begin{pmatrix} \ell_1 & \ell_2 & \ell \\ m_1 & m_2 & m \end{pmatrix}, \tag{II.2}$$

and the asterisk denotes complex conjugation. The symbols in parentheses in (II.2) are the 3-j symbols of Wigner, which are described extensively in Edmonds (1960, pp. 45–50). The expressions in (II.1) and (II.2) differ slightly from that in Edmonds because the spherical harmonic basis functions we employ (here and throughout this chapter) are normalized such that

$$\frac{1}{4\pi} \int_0^{2\pi} \int_0^{\pi} Y_{\ell_1}^{m_1}(\theta, \phi) Y_{\ell_2}^{m_2}(\theta, \phi)^* \sin\theta \, d\theta \, d\phi = \delta_{\ell_1,\ell_2} \delta_{m_1,m_2}. \tag{II.3}$$

The spherical harmonics we employ are therefore obtained from the Y_ℓ^m defined in Eq. [2.5.29] of Edmonds (1960) by setting $4\pi \to 1$.

The coupling coefficient in (II.2) may also be expressed in terms of the Clebsch–Gordon coefficients as follows:

$$\begin{bmatrix} m_1 & m_2 & m \\ \ell_1 & \ell_2 & \ell \end{bmatrix} = (-1)^m \left[\frac{(2\ell_1 + 1)(2\ell_2 + 1)}{(2\ell + 1)} \right]^{1/2} \times (\ell_1 0; \ell_2 0 | \ell 0)(\ell_1 m_1; \ell_2 m_2 | \ell m_1 + m_2). \tag{II.4}$$

The coupling coefficients in (II.2) will be identically zero unless the following conditions are satisfied:

$$|m_1| \leq \ell_1; \ |m_2| \leq \ell_2; \ |m| \leq \ell \tag{II.5}$$

$$m_1 + m_2 + m = 0, \tag{II.6}$$

$$|\ell_1 - \ell_2| \leq \ell \leq \ell_1 + \ell_2, \tag{II.7}$$

$$\ell_1 + \ell_2 + \ell \equiv \text{even}. \tag{II.8}$$

The condition (II.8) ensures that the sum in (II.1) is actually restricted to $\ell = \ell_1 + \ell_2, \ell_1 + \ell_2 - 2, \ell_1 + \ell_2 - 4, \ldots, |\ell_1 - \ell_2|$.

A useful illustration of Eq. (II.1) is provided by the simple example in which we couple Y_ℓ^m and Y_1^m ($m = 0, \pm 1$). According to (II.1), we write

$$Y_{\ell_1}^{m_1}(\theta, \phi) Y_1^{m_2}(\theta, \phi) = \sum_{\ell=\ell_1-1}^{\ell_1+1} \begin{bmatrix} m_1 & m_2 & -m_1 - m_2 \\ \ell_1 & 1 & \ell \end{bmatrix} Y_\ell^{-m_1-m_2}(\theta, \phi)^* \tag{II.9}$$

If we employ expression (II.4) and the Clebsch–Gordon coefficients $(\ell_1 m_1; 1 m_2 | \ell m_1 + m_2)$ tabulated in Condon and Shortley (1963, p. 76), we have

$$\begin{aligned} Y_{\ell_1}^{m_1} Y_1^0 &= \begin{bmatrix} m_1 & 0 & -m_1 \\ \ell_1 & 1 & \ell_1 - 1 \end{bmatrix} Y_{\ell_1-1}^{-m_1}{}^* + \begin{bmatrix} m_1 & 0 & -m_1 \\ \ell_1 & 1 & \ell_1 + 1 \end{bmatrix} Y_{\ell_1+1}^{-m_1}{}^* \\ &= \sqrt{3}\, b_{\ell_1-1}^{m_1} Y_{\ell_1-1}^{m_1} + \sqrt{3}\, b_{\ell_1}^{m_1} Y_{\ell_1+1}^{m_1}, \end{aligned} \tag{II.10}$$

$$\begin{aligned} Y_{\ell_1}^{m_1}\, Y_1^1 &= \begin{bmatrix} m_1 & 1 & -m_1 - 1 \\ \ell_1 & 1 & \ell_1 - 1 \end{bmatrix} Y_{\ell_1-1}^{-m_1-1}{}^* + \begin{bmatrix} m_1 & 1 & -m_1 - 1 \\ \ell_1 & 1 & \ell_1 + 1 \end{bmatrix} Y_{\ell_1+1}^{-m_1-1}{}^* \\ &= -\sqrt{\tfrac{3}{2}}\, c_{\ell_1-1}^{-m_1-1} Y_{\ell_1-1}^{m_1+1} + \sqrt{\tfrac{3}{2}}\, c_{\ell_1}^{m_1} Y_{\ell_1+1}^{m_1+1}, \end{aligned} \tag{II.11}$$

$$\begin{aligned} Y_{\ell_1}^{m_1} Y_1^{-1} &= \begin{bmatrix} m_1 & -1 & -m_1 + 1 \\ \ell_1 & 1 & \ell_1 - 1 \end{bmatrix} Y_{\ell_1-1}^{-m_1+1}{}^* \\ &\quad + \begin{bmatrix} m_1 & -1 & -m_1 + 1 \\ \ell_1 & 1 & \ell_1 + 1 \end{bmatrix} Y_{\ell_1+1}^{-m_1+1}{}^* \\ &= -\sqrt{\tfrac{3}{2}}\, c_{\ell_1-1}^{m_1-1} Y_{\ell_1-1}^{m_1-1} + \sqrt{\tfrac{3}{2}} c_{\ell_1}^{-m_1} Y_{\ell_1+1}^{m_1-1}, \end{aligned} \tag{II.12}$$

in which the quantities b_ℓ^m and c_ℓ^m are defined in Eq. (I.9) of Appendix I. Results (II.10)–(II.12) are quite useful and they are employed in Appendix III.

In Section 4 of the chapter we make extensive use of the generalized scalar spherical harmonics, introduced in the geophysical literature by Phinney and Burridge (1973). We shall therefore summarize the symmetry properties and coupling relations needed in Section 4. The generalized associated Legendre functions $P_\ell^{Nm}(\theta)$ in Phinney and Burridge (1973) are identical to the matrix elements of finite rotation $d_{Nm}^{(\ell)}(\theta)$ in Edmonds (1960, pp. 55–58). The generalized spherical harmonic functions

$$\tilde{Y}_\ell^{Nm}(\theta, \phi) \equiv d_{Nm}^{(\ell)}(\theta) e^{\mathrm{i}m\phi} \tag{II.13}$$

are related to the complete rotation-matrix elements $D_{Nm}^{(\ell)}(\phi, \theta, \gamma)$ in Edmonds (1960, Eq. [4.1.10]) as follows:

$$\tilde{Y}_\ell^{Nm}(\theta, \phi) = D_{Nm}^{(\ell)}(\phi, \theta, 0). \tag{II.14}$$

From the properties of $d_{Nm}^{(\ell)}(\theta)$ (see Eqs. [4.1.25], [4.2.6], and [2.5.29] in Edmonds) we may readily verify that

$$\tilde{Y}_\ell^{0m}(\theta, \phi) = \frac{1}{\sqrt{2\ell + 1}} Y_\ell^m(\theta, \phi), \tag{II.15}$$

where the Y_ℓ^m in (II.15) are the usual scalar spherical harmonics in (II.3). Owing to the result (II.15), we shall find it useful to employ the modified generalized spherical harmonics Y_ℓ^{Nm}, which are defined as

$$\begin{aligned} Y_\ell^{Nm}(\theta, \phi) &\equiv \sqrt{2\ell + 1}\ \tilde{Y}_\ell^{Nm}(\theta, \phi) \\ &= \sqrt{2\ell + 1}\ D_{Nm}^{(\ell)}(\phi, \theta, 0). \end{aligned} \tag{II.16}$$

This definition ensures that Y_ℓ^{Nm} reduces, when $N = 0$, to the usual Y_ℓ^m. In addition, this definition also leads to the following simplified orthonormality relation (obtained by employing (II.16) in Eq. [4.6.1] of Edmonds):

$$\frac{1}{4\pi} \int_0^{2\pi} \int_0^{\pi} Y_{\ell_1}^{Nm_1}(\theta, \phi)^*\ Y_{\ell_2}^{Nm_2}(\theta, \phi) \sin\theta\, d\theta\, d\phi = \delta_{\ell_1,\ell_2}\delta_{m_1,m_2}. \tag{II.17}$$

From the symmetry relations of the functions $D_{Nm}^{(\ell)}$ in (II.16) we have [Eq. [4.2.7] in Edmonds (1960)] the following useful result:

$$Y_\ell^{Nm}(\theta, \phi)^* = (-1)^{N+m} Y_\ell^{-N-m}(\theta, \phi). \tag{II.18}$$

If we now employ the definition of the Y_ℓ^{Nm}, in (II.16), in Eq. [4.3.2] of Edmonds, we then obtain the following important generalized coupling relation:

$$\begin{aligned} Y_{\ell_1}^{N_1 m_1}(\theta, \phi) Y_{\ell_2}^{N_2 m_2}(\theta, \phi) = \sum_{\ell=|\ell_1-\ell_2|}^{\ell_1+\ell_2} &[(2\ell_1 + 1)(2\ell_2 + 1)(2\ell + 1)]^{1/2} \\ &\times \begin{pmatrix} \ell_1 & \ell_2 & \ell \\ N_1 & N_2 & N \end{pmatrix} \begin{pmatrix} \ell_1 & \ell_2 & \ell \\ m_1 & m_2 & m \end{pmatrix} Y_\ell^{Nm}(\theta, \phi)^*. \end{aligned} \tag{II.19}$$

The Wigner 3-j symbols in (II.19) will be identically zero unless the following conditions are satisfied:

$$|m_1| \leq \ell_1;\ |m_2| \leq \ell_2;\ |m| \leq \ell, \tag{II.20}$$

$$|N_1| \leq \ell_1;\ |N_2| \leq \ell_2;\ |N| \leq \ell, \tag{II.21}$$

$$m_1 + m_2 + m = 0, \tag{II.22}$$

$$N_1 + N_2 + N = 0, \tag{II.23}$$

$$|\ell_1 - \ell_2| \leq \ell \leq \ell_1 + \ell_2. \tag{II.24}$$

It is worth emphasizing that condition (II.8) does not apply to (II.19) and thus the sum over ℓ must include all integer values between the limits specified in

(II.24). The Wigner 3-j symbols in (II.2) and (II.19) have two important symmetries [Eqs. [3.7.5] and [3.7.6] in Edmonds (1960)], which are exploited in Section 4:

$$\begin{pmatrix} \ell_1 & \ell_2 & \ell_3 \\ m_1 & m_2 & m_3 \end{pmatrix} = (-1)^{\ell_1+\ell_2+\ell_3}\begin{pmatrix} \ell_1 & \ell_2 & \ell_3 \\ -m_1 & -m_2 & -m_3 \end{pmatrix}, \tag{II.25}$$

$$(-1)^{\ell_1+\ell_2+\ell_3}\begin{pmatrix} \ell_1 & \ell_2 & \ell_3 \\ m_1 & m_2 & m_3 \end{pmatrix} = \begin{pmatrix} \ell_2 & \ell_1 & \ell_3 \\ m_2 & m_1 & m_3 \end{pmatrix} = \cdots = \begin{pmatrix} \ell_3 & \ell_2 & \ell_1 \\ m_3 & m_2 & m_1 \end{pmatrix}. \tag{II.26}$$

Relation (II.26) is simply an expression of the result that an *odd* number of permutations of the columns is equivalent to multiplication by $(-1)^{\ell_1+\ell_2+\ell_3}$.

The practical application of the theory developed in Sections 3 and 4 obviously depends on the ability to rapidly and accurately calculate the value of any given Wigner 3-j symbol. We shall now describe an efficient computational scheme we have implemented, based on the elegant group-theoretical formulation developed by LeBlanc (1986, 1987). LeBlanc has shown that any Wigner 3-j symbol, and its associated Clebsch–Gordon coefficient, may be directly evaluated using the following closed-form expression:

$$\begin{aligned} \begin{pmatrix} \ell_1 & \ell_2 & \ell_3 \\ m_1 & m_2 & m_3 \end{pmatrix} &= \frac{(-1)^{\ell_1-\ell_2-m_3}}{(2\ell_3+1)^{1/2}}\,(\ell_1 m_1;\ \ell_2 m_2 | \ell_3\ -\ m_3) \\ &= (-1)^{k_2-s_3}\left[\frac{1}{(J+1)!}\,\frac{k_1!k_2!}{k_3!}\,\frac{s_3!d_3!}{s_1!d_1!s_2!d_2!}\right]^{1/2} \\ &\quad \times F_{k_3}(s_1,d_2;\ s_2,d_1), \end{aligned} \tag{II.27}$$

in which

$$\begin{aligned} J &= \ell_1 + \ell_2 + \ell_3, \\ k_i &= J - 2\ell_i, \\ s_i &= \ell_i + m_i, \qquad (1 \leqslant i \leqslant 3) \\ d_i &= \ell_i - m_i, \\ m_2 &+ m_2 + m_3 = 0, \end{aligned} \tag{II.28}$$

and where the functional $F_{k_3}(\cdots)$ has a binomial-type expansion:

$$F_{k_3}(s_1,\ d_2;\ s_2,\ d_1) = \sum_{i=0}^{k_3} (-1)^i \binom{k_3}{i} [s_1]_{k_3-i}[d_2]_{k_3-i}[s_2]_i[d_1]_i, \tag{II.29}$$

in which $[x]_i = (x)(x-1)(x-2)\cdots(x-i+1)$ is a lowering factorial with

$[x]_0 \equiv 1$. The algebraically transparent expressions (II.27)–(II.29) should be contrasted with the corresponding expression in Eq. [3.6.11] of Edmonds (1960), which involves a complicated sum over an unspecified range. Expressions (II.27)–(II.29) may be directly implemented, in a straightforward manner, with only a few lines of computer code. The resulting numerical scheme, which directly generates the value of any given Wigner 3-j symbol, is found to be very efficient and stable. The efficiency of this scheme may be significantly improved by taking maximum advantage of the symmetry properties [i.e., Eqs. (II.25) and (II.26)] of the Wigner 3-j symbols.

As discussed in LeBlanc (1986), the Wigner 3-j symbol possesses all the symmetries of its Regge symbol counterpart defined by

$$\begin{pmatrix} \ell_1 & \ell_2 & \ell_3 \\ m_1 & m_2 & m_3 \end{pmatrix} = \begin{bmatrix} s_1 & s_2 & s_3 \\ d_1 & d_2 & d_3 \\ k_1 & k_2 & k_3 \end{bmatrix}. \tag{II.30}$$

The Regge symbol in (II.30) is invariant under all even permutations of its rows and columns, is invariant under transposition, and is multiplied by $(-1)^J$ for all odd permutations of its rows and columns. Such symmetries include the important relations (II.25) and (II.26). We may search the Regge symbol in (II.30) for the element with the smallest value and, by row and/or column interchanges, we translate this element to the bottom right corner initially occupied by k_3. With each row and/or column interchange we multiply by $(-1)^J$, and we also redefine the values of all the symbols d_i, s_i, and k_i in (II.27). By this procedure we obtain the smallest possible value for the upper summation limit in (II.29) and thus reduce the computational effort. Expression (II.27) now provides us with a very efficient method for calculating individual Wigner 3-j symbols and we therefore avoid the usual methods based on the recursion relations provided, for example, in Edmonds (1960).

APPENDIX III. Analytic Harmonic Decomposition of Horizontal Divergence and Radial Vorticity

We derive here analytic expressions for the spherical harmonic coefficients of the horizontal divergence and radial vorticity of the surface velocity field of N rigid plates. The starting point for the derivation is the set of equations (7), (9), (11), and (12), in Section 2.1 of the main text.

Introducing the spherical polar representation of the Cartesian coordinates x_i in Eqs. (7) and (9), we have

$$x_1 = a \sin\theta \cos\phi,\ x_2 = a \sin\theta \sin\phi,\ x_3 = a \cos\theta. \tag{III.1}$$

Employing (III.1) in Eqs. (7) and (9) yields the following result:

$$\Omega_i = \frac{a}{\sqrt{3}} [\omega^i_+ Y^1_1(\theta, \phi) + \omega^i_0 Y^0_1(\theta, \phi) + \omega^i_- Y^{-1}_1(\theta, \phi)], \tag{III.2}$$

where

$$\begin{aligned} \omega^i_+ &= \frac{1}{\sqrt{2}} [-(\omega^i_1 - \omega^N_1) + \iota(\omega^i_2 - \omega^N_2)] \\ \omega^i_0 &= \omega^i_3 - \omega^N_3 \\ \omega^i_- &= \frac{1}{\sqrt{2}} [(\omega^i_1 - \omega^N_1) + \iota(\omega^i_2 - \omega^N_2)], \end{aligned} \tag{III.3}$$

and

$$\Omega^N = \frac{a}{\sqrt{3}} [\omega^N_+ Y^1_1(\theta, \phi) + \omega^N_0 Y^0_1(\theta, \phi) + \omega^N_- Y^{-1}_1(\theta, \phi)], \tag{III.4}$$

where

$$\omega^N_+ = \frac{1}{\sqrt{2}} (-\omega^N_1 + \iota\omega^N_2), \ \omega^N_0 = \omega^N_3, \ \omega^N_- = \frac{1}{\sqrt{2}} (\omega^N_1 + \iota\omega^N_2). \tag{III.5}$$

By virtue of Eq. (I.12) in Appendix I we obtain, on the basis of (III.2), the following:

$$\begin{aligned} \Lambda\Omega_i = \frac{\iota a}{\sqrt{3}} [&\hat{\boldsymbol{e}}_{-1}(\omega^i_- Y^0_1 + \omega^i_0 Y^1_1) + \hat{\boldsymbol{e}}_0(-\omega^i_- Y^{-1}_1 + \omega^i_+ Y^1_1) \\ &- \hat{\boldsymbol{e}}_1(\omega^i_0 Y^{-1}_1 + \omega^i_+ Y^0_1)]. \end{aligned} \tag{III.6}$$

The last term on the right-hand side of Eq. (12) is, by virtue of (III.4),

$$-\frac{1}{a} \Lambda^2 \Omega^N = \frac{2}{\sqrt{3}} [\omega^N_+ Y^1_1 + \omega^N_0 Y^0_1 + \omega^N_- Y^{-1}_1]. \tag{III.7}$$

We may similarly show, on the basis of (III.2), that

$$-\frac{1}{a} \Lambda^2 \Omega_i = \frac{2}{\sqrt{3}} [\omega^i_+ Y^1_1 + \omega^i_0 Y^0_1 + \omega^i_- Y^{-1}_1]. \tag{III.8}$$

Employing result (I.8) of Appendix I, we have the following harmonic decomposition of the horizontal gradient of the plate function in Eq. (11):

$$
\begin{aligned}
\nabla_1 H_i(\theta, \phi) &= \nabla_1 \sum_{\ell,m} (H_i)_\ell^m Y_\ell^m(\theta, \phi) \\
&= \sum_{\ell,m} (H_i)_\ell^m \left\{ \frac{\hat{\boldsymbol{e}}_{-1}}{\sqrt{2}} [\ell c_\ell^m Y_{\ell+1}^{m+1} + (\ell + 1) c_{\ell-1}^{-m-1} Y_{\ell-1}^{m+1}] \right. \\
&\quad - \hat{\boldsymbol{e}}_0 [\ell b_\ell^m Y_{\ell+1}^m - (\ell + 1) b_{\ell-1}^m Y_{\ell-1}^m] \\
&\quad \left. + \frac{\hat{\boldsymbol{e}}_1}{\sqrt{2}} [\ell c_\ell^{-m} Y_{\ell+1}^{m-1} + (\ell + 1) c_{\ell-1}^{m-1} Y_{\ell-1}^{m-1}] \right\} \\
&= \sum_{\ell,m} Y_\ell^m \left\{ \frac{\hat{\boldsymbol{e}}_{-1}}{\sqrt{2}} \left[(H_i)_{\ell-1}^{m-1} (1 - \delta_{\ell 0}) \right. \right. \\
&\quad \left. \times (\ell - 1) c_{\ell-1}^{m-1} + (H_i)_{\ell+1}^{m-1} (\ell + 2) c_\ell^{-m} \right] \\
&\quad - \hat{\boldsymbol{e}}_o \left[(H_i)_{\ell-1}^m (1 - \delta_{\ell 0}) \right. \\
&\quad \left. \times (\ell - 1) b_{\ell-1}^m - (H_i)_{\ell+1}^m (\ell + 2) b_\ell^m \right] \\
&\quad + \frac{\hat{\boldsymbol{e}}_1}{\sqrt{2}} \left[(H_i)_{\ell-1}^{m+1} (1 - \delta_{\ell 0}) \right. \\
&\quad \left. \left. \times (\ell - 1) c_{\ell-1}^{-m-1} + (H_i)_{\ell+1}^{m+1} (\ell + 2) c_\ell^m \right] \right\}.
\end{aligned}
\tag{III.9}
$$

If we now employ result (I.12) in Appendix I, we also obtain the following result:

$$
\begin{aligned}
\Lambda H_i(\theta, \phi) &= \Lambda \sum_{\ell,m} (H_i)_\ell^m Y_\ell^m(\theta, \phi) \\
&= \iota \sum_{\ell,m} (H_i)_\ell^m \left\{ \frac{\hat{\boldsymbol{e}}_{-1}}{\sqrt{2}} a_\ell^m Y_\ell^{m+1} + \hat{\boldsymbol{e}}_0 m Y_\ell^m - \frac{\hat{\boldsymbol{e}}_1}{\sqrt{2}} a_\ell^{-m} Y_\ell^{m-1} \right\} \\
&= \iota \sum_{\ell,m} Y_\ell^m \left\{ \frac{\hat{\boldsymbol{e}}_{-1}}{\sqrt{2}} a_\ell^{m-1} (H_i)_\ell^{m-1} + \hat{\boldsymbol{e}}_0 m (H_i)_\ell^m \right. \\
&\quad \left. - \frac{\hat{\boldsymbol{e}}_{-1}}{\sqrt{2}} a_\ell^{-m-1} (H_i)_\ell^{m+1} \right\}
\end{aligned}
\tag{III.10}
$$

Combining results (III.6) and (III.9) we then obtain

$$
\begin{aligned}
-\frac{1}{a}\,\nabla_1\, H_i \cdot \mathbf{\Lambda}\Omega_i = \frac{\iota}{\sqrt{3}} \sum_{\ell,m} Y_\ell^m \Bigg\{ & \frac{1}{\sqrt{2}}\,(\omega_-^i\; Y_1^0 + \omega_0^i\; Y_1^1)(A_i)_\ell^m \\
& + (-\omega_-^i\; Y_1^{-1} + \omega_+^i\; Y_1^1)(B_i)_\ell^m \\
& + \frac{1}{\sqrt{2}}\,(\omega_+^i\; Y_1^0 + \omega_0^i\; Y_1^{-1})(-1)^m (A_i)_\ell^{-m*} \Bigg\},
\end{aligned}
\tag{III.11}
$$

where

$$
(A_i)_\ell^m = (H_i)_{\ell-1}^{m+1}(1 - \delta_{\ell 0})(\ell - 1)\, c_{\ell-1}^{-m-1} + (H_i)_{\ell+1}^{m+1}(\ell + 2)\, c_\ell^m, \tag{III.12}
$$

$$
(B_i)_\ell^m = (H_i)_{\ell-1}^m(1 - \delta_{\ell 0})(\ell - 1)\, b_{\ell-1}^m - (H_i)_{\ell+1}^m(\ell + 2)\, b_\ell^m. \tag{III.13}
$$

Employing results (II.10)–(II.12) in Appendix II, we obtain from (III.11) the following:

$$
\begin{aligned}
-\frac{1}{a}\,\nabla_1 H_i \cdot \mathbf{\Lambda}\Omega_i = \iota \sum_{\ell,m} Y_\ell^m \Bigg\{ & \frac{\omega_-^i}{\sqrt{2}} [b_\ell^m (A_i)_{\ell+1}^m + (1 - \delta_{\ell 0})\; b_{\ell-1}^m\; (A_i)_{\ell-1}^m \\
& + c_\ell^m (B_i)_{\ell+1}^{m+1} - (1 - \delta_{\ell 0}) c_{\ell-1}^{-m-1} (B_i)_{\ell-1}^{m+1}] \\
& + \frac{\omega_0^i}{2} [(1 - \delta_{\ell 0})(c_{\ell-1}^{m-1} (A_i)_{\ell-1}^{m-1} \\
& - c_{\ell-1}^{-m-1} (-1)^m (A_i)_{\ell-1}^{-m-1*}) \\
& - c_\ell^{-m} (A_i)_{\ell+1}^{m-1} + c_\ell^m (-1)^m (A_i)_{\ell+1}^{-m-1*}] \\
& + \frac{\omega_+^i}{\sqrt{2}} [b_\ell^m (-1)^m (A_i)_{\ell+1}^{-m*} \\
& + (1 - \delta_{\ell 0}) b_{\ell-1}^m (-1)^m (A_i)_{\ell-1}^{-m*} \\
& + (1 - \delta_{\ell 0}) c_{\ell-1}^{m-1} (B_i)_{\ell-1}^{m-1} - c_\ell^{-m} (B_i)_{\ell+1}^{m-1}] \Bigg\}.
\end{aligned}
\tag{III.14}
$$

From result (III.14) we immediately see that the spherical harmonic coefficients $(\nabla_H \cdot \mathbf{v})_\ell^m$ of the plate divergence in Eq. (11) of the main text are given by

$$
(\nabla_H \cdot \mathbf{v})_\ell^m = \sum_{i=1}^{N-1} \iota \left[\frac{\omega_-^i}{\sqrt{2}}\,(C_-^i)_\ell^m + \frac{\omega_0^i}{2}\,(C_0^i)_\ell^m + \frac{\omega_+^i}{\sqrt{2}}\,(C_+^i)_\ell^m \right], \tag{III.15}
$$

where

$$
\begin{aligned}
(C^i_-)^m_\ell &= b^m_\ell (A_i)^m_{\ell+1} + c^m_\ell (B_i)^{m+1}_{\ell+1} \\
&\quad + (1 - \delta_{\ell 0})[b^m_{\ell-1}(A_i)^m_{\ell-1} - c^{-m-1}_{\ell-1}(B_i)^{m+1}_{\ell-1}] \\
(C^i_0)^m_\ell &= -c^{-m}_\ell (A_i)^{m-1}_{\ell+1} + c^m_\ell (-1)^m (A_i)^{-m-1}_{\ell+1} * \\
&\quad + (1 - \delta_{\ell 0})[c^{m-1}_{\ell-1}(A_i)^{m-1}_{\ell-1} - c^{-m-1}_{\ell-1}(-1)^m (A_i)^{-m-1}_{\ell-1} *] \\
(C^i_+)^m_\ell &= b^m_\ell (-1)^m (A_i)^{-m}_{\ell+1} * - c^{-m}_\ell (B_i)^{m-1}_{\ell+1} \\
&\quad + (1 - \delta_{\ell 0})[b^m_{\ell-1}(-1)^m (A_i)^{-m}_{\ell-1} * + c^{m-1}_{\ell-1}(B_i)^{m-1}_{\ell-1}].
\end{aligned}
\tag{III.16}
$$

We may also express the harmonic coefficients of the horizontal divergence in terms of the Cartesian components of the plate rotation vectors. Employing result (III.15) and (III.16) and the definitions (III.3), we obtain

$$
\begin{aligned}
(\nabla_H \cdot \mathbf{v})^m_\ell = \sum_{i=1}^{N-1} &[(S^i_1)^m_\ell (\omega^i_1 - \omega^N_1) + (S^i_2)^m_\ell (\omega^i_2 - \omega^N_2) \\
&+ (S^i_3)^m_\ell (\omega^i_3 - \omega^N_3)],
\end{aligned}
\tag{III.17}
$$

where

$$
\begin{aligned}
(S^i_1)^m_\ell &= \frac{\iota}{2}[(C^i_-)^m_\ell - (C^i_+)^m_\ell], \\
(S^i_2)^m_\ell &= -\frac{1}{2}[(C^i_-)^m_\ell + (C^i_+)^m_\ell], \\
(S^i_3)^m_\ell &= \frac{\iota}{2}(C^i_0)^m_\ell.
\end{aligned}
\tag{III.18}
$$

We now derive analytic expressions for the radial vorticity field. Combining results (III.6), (III.8), and (III.10) we obtain the following:

$$
\begin{aligned}
-\frac{1}{a}\mathbf{\Lambda} H_i \cdot \mathbf{\Lambda}\Omega_i - \frac{1}{a} H_i \Lambda^2 \Omega_i &= \frac{1}{\sqrt{3}} \sum_{\ell,m} Y^m_\ell \left\{ \frac{1}{\sqrt{2}} (\omega^i_- Y^0_1 + \omega^i_0 Y^1_1) a^{-m-1}_\ell (H_i)^{m+1}_\ell \right. \\
&\quad + (-\omega^i_- Y^{-1}_1 + \omega^i_+ Y^1_1) m (H_i)^m_\ell \\
&\quad + \frac{1}{\sqrt{2}} (\omega^i_+ Y^0_1 + \omega^i_0 Y^{-1}_1) a^{m-1}_\ell (H_i)^{m-1}_\ell \\
&\quad \left. + 2(\omega^i_+ Y^1_1 + \omega^i_0 Y^0_1 + \omega^i_- Y^{-1}_1)(H_i)^m_\ell \right\}.
\end{aligned}
\tag{III.19}
$$

Applying results (II.10)–(II.12) of Appendix II to (III.19), we obtain the following, after some manipulations:

$$-\frac{1}{a}\,\mathbf{\Lambda}H_i\cdot\mathbf{\Lambda}\Omega_i-\frac{1}{a}\,H_i\Lambda^2\Omega_i$$

$$=\sum_{\ell,m}Y_\ell^m\left[\frac{\omega_-^i}{\sqrt{2}}\,(E_-^i)_\ell^m+\frac{\omega_0^i}{2}\,(E_0^i)_\ell^m+\frac{\omega_+^i}{\sqrt{2}}\,(E_+^i)_\ell^m\right], \tag{III.20}$$

where

$$\begin{aligned}
(E_-^i)_\ell^m &= (H_i)_{\ell+1}^{m+1}[b_\ell^m a_{\ell+1}^{-m-1}+c_\ell^m(m-1)]\\
&\quad+(H_i)_{\ell-1}^{m+1}(1-\delta_{\ell 0})[b_{\ell-1}^m a_{\ell-1}^{-m-1}-c_{\ell-1}^{-m-1}(m-1)],\\
(E_0^i)_\ell^m &= (H_i)_{\ell+1}^m[4b_\ell^m-c_\ell^m a_{\ell+1}^m-c_\ell^{-m}a_{\ell+1}^{-m}]\\
&\quad+(H_i)_{\ell-1}^m(1-\delta_{\ell 0})[4b_{\ell-1}^m+c_{\ell-1}^{-m-1}a_{\ell-1}^m+c_{\ell-1}^{m-1}a_{\ell-1}^{-m}],\\
(E_+^i)_\ell^m &= (H_i)_{\ell+1}^{m-1}[b_\ell^m a_{\ell+1}^{m-1}-c_\ell^{-m}(m+1)]\\
&\quad+(H_i)_{\ell-1}^{m-1}(1-\delta_{\ell 0})[b_{\ell-1}^m a_{\ell-1}^{m-1}+c_{\ell-1}^{m-1}(m+1)].
\end{aligned} \tag{III.21}$$

Results (III.7), (III.20), and (III.21) show that the spherical harmonic coefficients $(\hat{\boldsymbol{r}}\cdot\boldsymbol{\nabla}\times\mathbf{v})_\ell^m$ of the radial vorticity in Eq. (12) of the main text are given by

$$\begin{aligned}
(\hat{\boldsymbol{r}}\cdot\boldsymbol{\nabla}\times\mathbf{v})_\ell^m &= \sum_{i=1}^{N-1}\left\{\frac{\omega_-^i}{\sqrt{2}}\,(E_-^i)_\ell^m+\frac{\omega_0^i}{2}\,(E_0^i)_\ell^m+\frac{\omega_+^i}{\sqrt{2}}\,(E_+^i)_\ell^m\right\}\\
&\quad+\frac{2}{\sqrt{3}}\,\delta_{\ell 1}(\omega_+^N\delta_{m1}+\omega_0^N\delta_{m0}+\omega_-^N\delta_{m,-1}).
\end{aligned} \tag{III.22}$$

We may also express the harmonic coefficients of the radial vorticity in terms of the Cartesian components of the plate rotation vectors. Employing result (III.22) and the definitions (III.3) and (III.5), we obtain

$$\begin{aligned}
(\hat{\boldsymbol{r}}\cdot\boldsymbol{\nabla}\times\mathbf{v})_\ell^m &= \sum_{i=1}^{N-1}[(R_1^i)_\ell^m(\omega_1^i-\omega_1^N)+(R_2^i)_\ell^m(\omega_2^i-\omega_2^N)\\
&\quad+(R_3^i)_\ell^m(\omega_3^i-\omega_3^N)]+\sum_{j=1}^{3}\delta_{\ell 1}N_j^m\omega_j^N,
\end{aligned} \tag{III.23}$$

where

$$\begin{aligned}
(R_1^i)_\ell^m &= \frac{1}{2}\,[(E_-^i)_\ell^m-(E_+^i)_\ell^m],\\
(R_2^i)_\ell^m &= \frac{\iota}{2}\,[(E_-^i)_\ell^m+(E_+^i)_\ell^m],\\
(R_3^i)_\ell^m &= \frac{1}{2}\,(E_0^i)_\ell^m,
\end{aligned} \tag{III.24}$$

$$N_1^m = \sqrt{\frac{2}{3}}\,(\delta_{m,-1} - \delta_{m1}),$$

$$N_2^m = \iota\sqrt{\frac{2}{3}}\,(\delta_{m,-1} + \delta_{m1}), \tag{III.25}$$

$$N_3^m = \frac{2}{\sqrt{3}}\,\delta_{m0}.$$

APPENDIX IV. MOMENTUM CONSERVATION IN A MEDIUM WITH 3D VISCOSITY VARIATIONS

The equation of momentum conservation, in Cartesian tensor form, for quasi-static deformation in a continuum is

$$\partial_j T_{ji} + \rho\partial_i\phi = 0, \tag{IV.1}$$

(where $T_{ji} = T_{ij}$ is the stress tensor, ρ is the density, and $\partial_i\phi$ is the body force per unit mass. The inertial force $\rho du_i/dt$ that normally appears on the right-hand side of (IV.1) is neglected because the viscosity of the medium (e.g., the Earth's mantle), and hence its Prandtl number, is extremely large. The total stress T_{ij} may be written as the sum of its deviatoric and spherical components as follows

$$T_{ij} = -P\delta_{ij} + \tau_{ij}, \tag{IV.2}$$

where

$$P = -\tfrac{1}{3}T_{kk}, \tag{IV.3}$$

and

$$\tau_{ij} = T_{ij} - \tfrac{1}{3}T_{kk}\delta_{ij}. \tag{IV.4}$$

As indicated in Eqs. (1) and (2) of the main text, the deviatoric stress τ_{ij} in a solid medium creeping with deviatoric strain rate E_{ij} is given by

$$\tau_{ij} = 2\eta E_{ij} = \eta(\partial_i u_j + \partial_j u_i - \tfrac{2}{3}\partial_k u_k\delta_{ij}), \tag{IV.5}$$

in which η is the effective viscosity [see Eq. (3) of the text] of the solid medium. From Eqs. (IV.2) and (IV.5), we obtain

$$\partial_j T_{ji} = -\partial_i P + \tfrac{1}{3}\eta\partial_i(\partial_k u_k) - \tfrac{2}{3}(\partial_i\eta)(\partial_k u_k) + \eta\partial_j\partial_j u_i$$
$$+ (\partial_j\eta)(\partial_j u_i) + \partial_i(u_j\partial_j\eta) - u_j\partial_j(\partial_i\eta).$$

Employing vector notation, we may rewrite this last expression as

$$\nabla \cdot \underline{\mathbf{T}} = -\nabla P + \tfrac{1}{3}\eta\nabla(\nabla \cdot \mathbf{u}) - \tfrac{2}{3}(\nabla \cdot \mathbf{u})\nabla\eta + \eta\nabla^2\mathbf{u} + (\nabla\eta \cdot \nabla)\mathbf{u} + \nabla(\mathbf{u} \cdot \nabla\eta) - (\mathbf{u} \cdot \nabla)\nabla\eta. \tag{IV.6}$$

Employing the vector calculus identity

$$\nabla(\mathbf{A} \cdot \mathbf{B}) = (\mathbf{A} \cdot \nabla)\mathbf{B} + (\mathbf{B} \cdot \nabla)\mathbf{A} + \mathbf{A} \times (\nabla \times \mathbf{B}) + \mathbf{B} \times (\nabla \times \mathbf{A}),$$

we may rewrite (IV.6) as

$$\nabla \cdot \underline{\mathbf{T}} = -\nabla P + \tfrac{1}{3}\eta\nabla(\nabla \cdot \mathbf{u}) - \tfrac{2}{3}(\nabla \cdot \mathbf{u})\nabla\eta + \eta\nabla^2\mathbf{u} + 2(\nabla\eta \cdot \nabla)\mathbf{u} + \nabla\eta \times (\nabla \times \mathbf{u}). \tag{IV.7}$$

Combining (IV.1) and (IV.7) now yields

$$-\nabla P_1 + \tfrac{1}{3}\eta\nabla(\nabla \cdot \mathbf{u}) + \eta\nabla^2\mathbf{u} - \tfrac{2}{3}(\nabla \cdot \mathbf{u})\nabla\eta + 2(\nabla\eta \cdot \nabla)\mathbf{u} + \nabla\eta \times (\nabla \times \mathbf{u}) + \rho_1\nabla\phi_0 + \rho_0\nabla\phi_1 = 0, \tag{IV.8}$$

in which we have removed the expression

$$-\nabla P_0 + \rho_0\nabla\phi_0 = 0$$

for the hydrostatic equilibrium state and $P_1(|P_1/P_0| \ll 1)$, $\rho_1(|\rho_1/\rho_0| \ll 1)$, $\phi_1(|\phi_1/\phi_0| \ll 1)$ are respectively the perturbations to the pressure, density, and gravitational potential associated with the flow $\mathbf{u}$.

We may formally eliminate the nonhydrostatic pressure P_1 by taking the curl of (IV.8):

$$\eta\nabla^2(\nabla \times \mathbf{u}) + \nabla\eta \times \nabla^2\mathbf{u} + \nabla\eta \times \nabla(\nabla \cdot \mathbf{u}) + 2\nabla \times [(\nabla\eta \cdot \nabla)\mathbf{u}] + \nabla \times [\nabla\eta \times (\nabla \times \mathbf{u})] + \Lambda\left(\frac{\rho_1 g_0}{r} + \frac{\dot{\rho}_0\phi_1}{r}\right) = 0, \tag{IV.9}$$

in which $g_0 = -d\phi_0/dr$, $\dot{\rho}_0 = d\rho_0/dr$, and $\Lambda = \mathbf{r} \times \nabla$. The scalar equation describing (in the limit of no lateral viscosity variations) the poloidal flow is obtained by applying the operator $\Lambda \cdot$ (i.e., $\mathbf{r} \cdot \nabla\times$) to Eq. (IV.9):

$$\eta\nabla^2\left[\nabla^2 r u_r - \frac{1}{r}\frac{\partial}{\partial r}(r^2\nabla \cdot \mathbf{u})\right] + [(\nabla^2\eta) + \nabla\eta \cdot \nabla][\nabla^2 r u_r - 2(\nabla \cdot \mathbf{u})] - r\dot{\eta}\nabla^2(\nabla \cdot \mathbf{u}) - \Lambda \cdot [\nabla\eta \times \nabla(\nabla \cdot \mathbf{u})] - \nabla(r\dot{\eta}) \cdot \nabla^2\mathbf{u} - \Lambda\eta \cdot \nabla^2(\nabla \times \mathbf{u}) - 2\Lambda \cdot \nabla \times [(\nabla\eta \cdot \nabla)\mathbf{u}] - \Lambda \cdot \nabla \times [\nabla\eta \times (\nabla \times \mathbf{u})] = \Lambda^2\left(\frac{\rho_1 g_0}{r} + \frac{\dot{\rho}_0\phi_1}{r}\right), \tag{IV.10}$$

in which $u_r = \hat{\mathbf{r}} \cdot \mathbf{u}$, $\dot{\eta} = \partial\eta/\partial r$, $\Lambda^2 = \boldsymbol{\Lambda} \cdot \boldsymbol{\Lambda}$ is the horizontal Laplacian operator (Backus, 1958). In deriving Eq. (IV.10) we have made use of the vector calculus identities

$$\boldsymbol{\nabla} \times (\mathbf{A} \times \mathbf{B}) = \mathbf{B} \cdot \boldsymbol{\nabla}\mathbf{A} - \mathbf{A} \cdot \boldsymbol{\nabla}\mathbf{B} + \mathbf{A}\boldsymbol{\nabla} \cdot \mathbf{B} - \mathbf{B}\boldsymbol{\nabla} \cdot \mathbf{A},$$

$$\boldsymbol{r} \cdot \nabla^2\mathbf{A} = \nabla^2\mathbf{r} \cdot \mathbf{A} - 2\boldsymbol{\nabla} \cdot \mathbf{A},$$

and

$$\mathbf{r} \cdot (\mathbf{A} \cdot \boldsymbol{\nabla}\mathbf{B}) = \mathbf{A} \cdot \boldsymbol{\nabla}(\mathbf{r} \cdot \mathbf{B}) - \mathbf{A} \cdot \mathbf{B}.$$

A comparison of Eq. (IV.10) (when $\boldsymbol{\nabla} \cdot \mathbf{u} = 0$) with the corresponding Eq. (2) in Stewart (1992) shows that the latter is incomplete and incorrect. The existence of lateral viscosity variations ensures that buoyancy forces [on the right-hand side of Eq. (IV.10)] directly excite toroidal flow, in addition to poloidal flow, and this toroidal flow is implicitly described by the last four terms on the left-hand side of Eq. (IV.10). The scalar equation describing (in the limit of no lateral viscosity variations) the toroidal flow is obtained by applying the operator $\mathbf{r} \cdot$ to Eq. (IV.9):

$$\eta\nabla^2(\boldsymbol{\Lambda} \cdot \mathbf{u}) + \boldsymbol{\Lambda}\eta \cdot \nabla^2\mathbf{u} + \boldsymbol{\Lambda}\eta \cdot \boldsymbol{\nabla}(\boldsymbol{\nabla} \cdot \mathbf{u}) + 2\boldsymbol{\Lambda} \cdot [(\boldsymbol{\nabla}\eta \cdot \boldsymbol{\nabla})\mathbf{u}] + \boldsymbol{\Lambda} \cdot [\boldsymbol{\nabla}\eta \times (\boldsymbol{\nabla} \times \mathbf{u})] = 0. \quad \text{(IV.11)}$$

APPENDIX V. Viscous Stress Acting on an Undulating Surface

We consider here a surface, in a material continuum, obtained by distorting a spherical surface $r = c$ by a small amount $\delta c(\theta, \phi)$ such that $|\delta c(\theta, \phi)/c| \ll 1$. The equation describing this surface may be written as

$$f(r, \theta, \phi) = c, \quad \text{(V.1)}$$

in which $f(r, \theta, \phi) = r - \delta c(\theta, \phi)$. It is clear from (V.1) that $\boldsymbol{\nabla} f$ will be normal to this surface and thus we have

$$\hat{\boldsymbol{n}} \equiv \boldsymbol{\nabla} f = \hat{\boldsymbol{r}} - \frac{1}{c}\boldsymbol{\nabla}_1\, \delta c(\theta, \phi), \quad \text{(V.2)}$$

in which $\hat{\boldsymbol{n}}$ is the vector normal to the undulating surface, $\hat{\boldsymbol{r}}$ is the unit radial vector, and $\boldsymbol{\nabla}_1$ is the horizontal gradient operator (see Appendix I). The normal vector $\hat{\boldsymbol{n}}$ is, to within order $|\delta c/c|^2$, a unit vector. The stress vector $\mathbf{t}$ acting on each element of the undulating surface is given by

$$\mathbf{t}(r = c + \delta c) = \hat{\boldsymbol{n}} \cdot \underline{\mathbf{T}}\,(c + \delta c), \quad \text{(V.3)}$$

in which $\underline{\mathbf{T}}\,(c + \delta c)$ is the stress tensor evaluated at $r = c + \delta c$. In an effectively viscous continuum we have (see Appendix IV)

$$\underline{\mathbf{T}} = -P\underline{\mathbf{I}} + 2\eta\underline{\mathbf{E}}, \tag{V.4}$$

in which P is the pressure, η is the dynamic viscosity, and $\underline{\mathbf{E}}$ is the deviatoric strain-rate tensor. Combining (V.2)–(V.4), we obtain

$$\mathbf{t} = -(P_0 + P_1)\hat{\boldsymbol{r}} + 2\eta(E_{rr}\hat{\boldsymbol{r}} + E_{r\theta}\hat{\boldsymbol{\theta}} + E_{r\phi}\hat{\boldsymbol{\phi}}) + \frac{P_0}{c}\nabla_1\,\delta c, \tag{V.5}$$

in which we have ignored the second-order terms $P_1\,\delta c$ and $\delta c\,\underline{\mathbf{E}}$. Employing the expressions for the strain-rate tensor components in spherical polar coordinates (e.g., Morse and Feshbach, 1953, p. 117), we obtain from (V.5) the following expression

$$\mathbf{t}(r = c + \delta c) = -\hat{\boldsymbol{r}}[P_0 + P_1]_{r=c+\delta c} + \frac{P_0(c + \delta c)}{c}\nabla_1\delta c + \hat{\boldsymbol{r}}2\eta\left[\frac{\partial u_r}{\partial r} - \frac{1}{3}\nabla\cdot\mathbf{u}\right]_{r=c+\delta c} + \eta\left[\nabla_H u_r + r\frac{\partial}{\partial r}\left(\frac{\mathbf{u}_H}{r}\right)\right]_{r=c+\delta c}, \tag{V.6}$$

in which P_0 and P_1 are respectively the hydrostatic and nonhydrostatic pressure, ∇_H is the horizontal gradient operator on the spherical surface $r = c$, and $\mathbf{u}_H = u_\theta\,\hat{\boldsymbol{\theta}} + u_\phi\,\hat{\boldsymbol{\phi}}$ is the horizontal flow velocity. The hydrostatic pressure gradient is $dP_0/dr = -\rho_0 g_0$, and thus we may write (V.6) as the following first-order accurate expression:

$$\mathbf{t}(r = c + \delta c) = -\hat{\boldsymbol{r}}[P_0 + P_1 - \rho_0 g_0\,\delta c]_{r=c} + \frac{P_0(r = c)}{c}\nabla_1\delta c + \hat{\boldsymbol{r}}2\eta\left[\frac{\partial u_r}{\partial r} - \frac{1}{3}\nabla\cdot\mathbf{u}\right]_{r=c} + \eta\left[\nabla_H u_r + r\frac{\partial}{\partial r}\left(\frac{\mathbf{u}_H}{r}\right)\right]_{r=c}. \tag{V.7}$$

The continuity of stress across the undulating surface requires that $\mathbf{t}(r = c + \delta c^+) = \mathbf{t}(r = c + \delta c^-)$, and thus, using (V.7), we obtain the following matching conditions:

$$-P_1(r = c^+) + \rho_0(r = c^+)g_0\delta c + 2\eta\left[\frac{\partial u_r}{\partial r} - \frac{1}{3}\nabla\cdot\mathbf{u}\right]_{r=c^+} = -P_1(r = c^-) + \rho_0(r = c^-)g_0\delta c + 2\eta\left[\frac{\partial u_r}{\partial r} - \frac{1}{3}\nabla\cdot\mathbf{u}\right]_{r=c^-}, \tag{V.8}$$

$$\eta\left[\nabla_H u_r + r\frac{\partial}{\partial r}\left(\frac{\mathbf{u}_H}{r}\right)\right]_{r=c^+} = \eta\left[\nabla_H u_r + r\frac{\partial}{\partial r}\left(\frac{\mathbf{u}_H}{r}\right)\right]_{r=c^-}. \tag{V.9}$$

APPENDIX VI. DYNAMIC TOPOGRAPHY WITH LATERAL VISCOSITY VARIATIONS

We derive here explicit expressions for the spherical harmonic components of the dynamic surface topography δa_ℓ^m, on the basis of Eq. (161) in the main text. The covariant equations of momentum conservation, obtained by Phinney and Burridge (1973, see their Eq. [4.10]) applied to the problem of quasistatic deformation, yield the following expression:

$$r\frac{d}{dr}[(T^{0-})_\ell^m + (T^{0+})_\ell^m] + 3[(T^{0+})_\ell^m + (T^{0-})_\ell^m] - 2\Omega_1^\ell(T^{+-})_\ell^m - \Omega_2^\ell[(T^{++})_\ell^m + (T^{--})_\ell^m] + 2\rho_0\Omega_1^\ell(\phi_1)_\ell^m = 0, \quad \text{(VI.1)}$$

in which the terms $(T^{\alpha\beta})_\ell^m$ are the generalized spherical harmonic coefficients of the contravariant stress tensor

$$T^{\alpha\beta} = -P_1 e^{\alpha\beta} + 2\eta E^{\alpha\beta}, \quad \text{(VI.2)}$$

where $e^{\alpha\beta}$ is the contravariant representation of δ_{ij} and $E^{\alpha\beta}$ is the contravariant strain-rate tensor defined in Eq. (109) of the main text. Substitution of Eqs. (110) and (111) of the main text into Eq. (VI.2) yields

$$\sum_{\ell,m}(T^{0\pm})_\ell^m Y_\ell^{\pm 1m} = \sum_{s,t}\sum_{u,v}[\eta_s^t Y_s^{0t}]\left[\left(\frac{d}{dr} - \frac{1}{r}\right)(U^+)_u^v + \frac{1}{r}\Omega_1^u(U^0)_u^v\right]Y_u^{\pm 1v},$$

$$\sum_{\ell,m}(T^{\pm\pm})_\ell^m Y_\ell^{\pm 2m} = \sum_{s,t}\sum_{u,v}[\eta_s^t Y_s^{0t}][\Omega_2^u(U^\pm)_u^v]Y_u^{\pm 2v}, \quad \text{(VI.3)}$$

$$\sum_{\ell,m}(T^{+-})_\ell^m Y_\ell^{0m} = \sum_{\ell,m}(P_1)_\ell^m Y_\ell^{0m} + \sum_{s,t}\sum_{u,v}[\eta_s^t Y_s^{0t}]\frac{1}{r}[\Omega_1^u(U^P)_u^v - 2(U^0)_u^v]Y_u^{0v},$$

where $(U^P)_\ell^m = (U^+)_\ell^m + (U^-)_\ell^m$. By virtue of the orthogonality property and coupling relation [see Eqs. (II.17) and (II.19) in Appendix II] for generalized spherical harmonics Y_ℓ^{Nm}, we then obtain from (VI.3) the following:

$$(T^{+-})_\ell^m = (P_1)_\ell^m + \frac{(-1)^m}{r}\sum_{s,t}[\Omega_1^s(U^P)_s^t - 2(U^0)_s^t] \times \sum_{J=|\ell-s|}^{\ell+s}[(2\ell+1)(2s+1)(2J+1)]^{1/2} \times \begin{pmatrix}\ell & s & J\\ 0 & 0 & 0\end{pmatrix}\begin{pmatrix}\ell & s & J\\ -m & t & m-t\end{pmatrix}\eta_J^{m-t}, \quad \text{(VI.4)}$$

$$
\begin{aligned}
(T^{++})^m_\ell + (T^{--})^m_\ell = \frac{(-1)^m 2}{r} \sum_{s,t} \Omega_2^s \Bigg\{ (U^P)^t_s \sum_{J=|\ell-s|}^{\ell+s} \left[\frac{1 + (-1)^{\ell+s+J}}{2} \right] \\
\times [(2\ell + 1)(2s + 1)(2J + 1)]^{1/2} \\
\times \begin{pmatrix} \ell & s & J \\ 2 & -2 & 0 \end{pmatrix} \begin{pmatrix} \ell & s & J \\ -m & t & m - t \end{pmatrix} \eta_J^{m-t} - (U^T)^t_s \\
\times \sum_{J=|\ell-s|}^{\ell+s} \left[\frac{1 - (-1)^{\ell+s+J}}{2} \right] \\
\times [(2\ell + 1)(2s + 1)(2J + 1)]^{1/2} \\
\times \begin{pmatrix} \ell & s & J \\ 2 & -2 & 0 \end{pmatrix} \begin{pmatrix} \ell & s & J \\ -m & t & m - t \end{pmatrix} \eta_J^{m-t} \Bigg\},
\end{aligned}
\tag{VI.5}
$$

$$
\begin{aligned}
(T^{0-})^m_\ell + (T^{0+})^m_\ell = -(-1)^m \sum_{s,t} \Bigg\{ \left[\left(\frac{d}{dr} - \frac{1}{r} \right) (U^P)^t_s + \frac{2}{r} \Omega_1^s (U^0)^t_s \right] \\
\times \sum_{J=|\ell-s|}^{\ell+s} \left[\frac{1 + (-1)^{\ell+s+J}}{2} \right] [(2\ell + 1)(2s + 1) \\
\times (2J + 1)]^{1/2} \begin{pmatrix} \ell & s & J \\ 1 & -1 & 0 \end{pmatrix} \begin{pmatrix} \ell & s & J \\ -m & t & m - t \end{pmatrix} \eta_J^{m-t} \\
- \left(\frac{d}{dr} - \frac{1}{r} \right) (U^T)^t_s \sum_{J=|\ell-s|}^{\ell+s} \left[\frac{1 - (-1)^{\ell+s+J}}{2} \right] \\
\times [(2\ell + 1)(2s + 1)(2J + 1)]^{1/2} \\
\times \begin{pmatrix} \ell & s & J \\ 1 & -1 & 0 \end{pmatrix} \begin{pmatrix} \ell & s & J \\ -m & t & m - t \end{pmatrix} \eta_J^{m-t} \Bigg\},
\end{aligned}
\tag{VI.6}
$$

where $(U^T)^m_\ell = (U^+)^m_\ell - (U^-)^m_\ell$. If we now substitute expressions (VI.4)–(VI.6) into Eq. (VI.1), and we employ the free-slip (i.e., $T^{0-} = T^{0+} = 0$), zero radial velocity (i.e., $U^0 = 0$) boundary conditions that obtain at $r = a$, we then find that

$$
\begin{aligned}
-(P_1)^m_\ell(r = a^-) = {} & -\rho_0^-(\phi_1)^m_\ell(a) + (-1)^m \sum_{s,t} \left\{ \Omega_1^s \left[\frac{(U^P)^t_s}{r} \right]_{r=a^-} \right. \\
& \times \sum_{J=|\ell-s|,2}^{\ell+s} [(2\ell+1)(2s+1)(2J+1)]^{1/2} \\
& \left. \times \begin{pmatrix} \ell & s & J \\ 0 & 0 & 0 \end{pmatrix} \begin{pmatrix} \ell & s & J \\ -m & t & m-t \end{pmatrix} \eta_J^{m-t} \right\} \\
& + \frac{\Omega_2^\ell}{\Omega_1^\ell} (-1)^m \sum_{s,t} \Omega_2^s \left\{ \left[\frac{(U^P)^t_s}{r} \right]_{r=a^-} \sum_{J=|\ell-s|,2}^{\ell+s} \right. \\
& \times [(2\ell+1)(2s+1)(2J+1)]^{1/2} \\
& \left. \times \begin{pmatrix} \ell & s & J \\ 2 & -2 & 0 \end{pmatrix} \begin{pmatrix} \ell & s & J \\ -m & t & m-t \end{pmatrix} \eta_J^{m-t} \right. \\
& - \left[\frac{(U^T)^t_s}{r} \right]_{r=a^-} \sum_{J=|\ell-s|+1,2}^{\ell+s-1} [(2\ell+1) \\
& \times (2s+1)(2J+1)]^{1/2} \begin{pmatrix} \ell & s & J \\ 2 & -2 & 0 \end{pmatrix} \\
& \left. \times \begin{pmatrix} \ell & s & J \\ -m & t & m-t \end{pmatrix} \eta_J^{m-t} \right\} \\
& + \frac{(-1)^m}{2\Omega_1^\ell} \sum_{s,t} \left\{ \left[r \frac{d^2}{dr^2} (U^P)^t_s + 2\Omega_1^s \frac{d}{dr} (U^0)^t_s \right]_{r=a^-} \right. \\
& \times \sum_{J=|\ell-s|,2}^{\ell+s} [(2\ell+1)(2s+1)(2J+1)]^{1/2} \\
& \times \begin{pmatrix} \ell & s & J \\ 1 & -1 & 0 \end{pmatrix} \begin{pmatrix} \ell & s & J \\ -m & t & m-t \end{pmatrix} \eta_J^{m-t} \\
& - \left[r \frac{d^2}{dr^2} (U^T)^t_s \right]_{r=a^-} \sum_{J=|\ell-s|+1,2}^{\ell+s-1} [(2\ell+1) \\
& \times (2s+1)(2J+1)]^{1/2} \begin{pmatrix} \ell & s & J \\ 1 & -1 & 0 \end{pmatrix} \\
& \left. \times \begin{pmatrix} \ell & s & J \\ -m & t & m-t \end{pmatrix} \eta_J^{m-t} \right\}, \qquad \text{(VI.7)}
\end{aligned}
$$

in which we employ the notation $\Sigma_{J=k,2}$ to imply a sum over the terms with $J = k$, $k + 2$, $k + 4, \ldots$. According to Eq. (119) in the main text, we may relate the flow scalars U^P, U^T, U^0 to the corresponding poloidal and toroidal flow scalars as follows:

$$\begin{aligned}
(U^P)^m_\ell &= -2\Omega^\ell_1 \left[\frac{dp^m_\ell}{dr} + \frac{p^m_\ell}{r} \right], \\
(U^T)^m_\ell &= \iota 2\Omega^\ell_1 q^m_\ell, \\
(U^0)^m_\ell &= -2(\Omega^\ell_1)^2 \frac{p^m_\ell}{r},
\end{aligned} \tag{VI.8}$$

where $\iota = \sqrt{-1}$, p^m_ℓ and q^m_ℓ are respectively the spherical harmonic coefficients of the poloidal and toroidal flow scalars. If we now substitute Eq. (VI.7) into Eq. (161) of the main text and employ (VI.8), we then find

$$\begin{aligned}
g_0(\rho_0^+ - \rho_0^-)\delta a^m_\ell = {} & (\rho_0^+ - \rho_0^-)(\phi_1)^m_\ell(a) - (-1)^m \sum_{s,t} 6(\Omega^s_1)^2 \\
& \times \left[\frac{1}{r} \frac{dp^t_s}{dr} \right]_{r=a^-} \sum_{J=|\ell-s|,2}^{\ell+s} P^J_0(\ell, m, s, t)\eta^{m-t}_J \\
& - (-1)^m \frac{\Omega^\ell_2}{\Omega^\ell_1} \sum_{s,t} 2\Omega^s_2\Omega^s_1 \\
& \times \left\{ \left[\frac{1}{r} \frac{dp^t_s}{dr} \right]_{r=a^-} \sum_{J=|\ell-s|,2}^{\ell+s} P^J_2(\ell, m, s, t)\eta^{m-t}_J + \iota \left[\frac{q^t_s}{r} \right]_{r=a^-} \right. \\
& \left. \times \sum_{J=|\ell-s|+1,2}^{\ell+s-1} P^J_2(\ell, m, s, t)\eta^{m-t}_J \right\} \\
& - \frac{(-1)^m}{\Omega^\ell_1} \sum_{s,t} \Omega^s_1 \left\{ \left[r \frac{d^3p^t_s}{dr^3} + \frac{2(\Omega^s_2)^2}{r} \frac{dp^t_s}{dr} \right]_{r=a^-} \right. \\
& \times \sum_{J=|\ell-s|,2}^{\ell+s} P^J_1(\ell, m, s, t)\eta^{m-t}_J \\
& \left. + \iota \left[r \frac{d^2q^t_s}{dr^2} \right]_{r=a^-} \sum_{J=|\ell-s|+1,2}^{\ell+s-1} P^J_1(\ell, m, s, t)\eta^{m-t}_J \right\},
\end{aligned} \tag{VI.9}$$

in which

$$\begin{aligned}
P^J_k(\ell, m, s, t) = {} & [(2\ell + 1)(2s + 1)(2J + 1)]^{1/2} \\
& \times \begin{pmatrix} \ell & s & J \\ k & -k & 0 \end{pmatrix} \begin{pmatrix} \ell & s & J \\ -m & t & m - t \end{pmatrix}.
\end{aligned}$$

In the limit of no lateral variations of viscosity, it is readily shown that Eq. (VI.9) reduces to

$$\delta a_\ell^m = \frac{\eta_0^0}{g_0(\rho_0^- - \rho_0^+)} \left[-r \frac{d^3 p_\ell^m}{dr^3} + \frac{3\ell(\ell+1)}{r} \frac{dp_\ell^m}{dr} \right]_{r=a^-} + \frac{(\phi_1)_\ell^m(a)}{g_0}.$$

APPENDIX VII. NONHYDROSTATIC GEOID IN A SELF-GRAVITATING MANTLE

We provide here a brief derivation of the nonhydrostatic geoid produced by buoyancy-induced flow in a self-gravitating mantle. The derivation closely follows that in Appendix A in Forte and Peltier (1987) and corrects the typographical errors present there.

The total gravitational potential perturbation due to internal density anomalies and boundary deflections is

$$\begin{aligned}(\phi_1)_\ell^m(r) = (U_{\text{int}})_\ell^m(r) &+ \frac{4\pi a G}{2\ell+1} \Delta\rho_{mo} \left(\frac{r}{a}\right)^\ell (\delta a)_\ell^m \\ &+ \frac{4\pi b G}{2\ell+1} \Delta\rho_{cm} \left(\frac{b}{r}\right)^{\ell+1} (\delta b)_\ell^m,\end{aligned} \tag{VII.1}$$

in which G is the universal gravitational constant, δa is the boundary perturbation of the outer surface and $\Delta\rho_{mo} = 2.2$ Mg/m^3 is the corresponding density jump, δb is the perturbation of the core–mantle boundary (CMB) and $\Delta\rho_{cm} = 4.43$ Mg/m^3 is density jump across the CMB. The term $(U_{\text{int}})_\ell^m(r)$ is the gravitational potential due to internal density anomalies:

$$(U_{\text{int}})_\ell^m(r) = \frac{4\pi G}{2\ell+1} \int_b^a \frac{r_<^\ell}{r_>^{\ell+1}} (\rho_1)_\ell^m(r') r'^2 \, dr', \tag{VII.2}$$

where $r_< = \min(r, r')$ and $r_> = \max(r, r')$. As shown in Eqs. (162) and (164) of the main text, the surface topography $(\delta a)_\ell^m$ and CMB topography $(\delta b)_\ell^m$ contains contributions $(\phi_1)_\ell^m/g_0$ arising from self-gravitation. Equation (VII.1) is therefore an implicit equation for $(\phi_1)_\ell^m(r = a,b)$, which may be solved by evaluating (VII.1) at $r = a$ and $r = b$ and then solving the resulting two equations for $(\phi_1)_\ell^m(a)$ and $(\phi_1)_\ell^m(b)$. In this manner we obtain

$$\begin{aligned}\frac{(\phi_1)_\ell^m(a)}{g_0} = \frac{3}{2\ell+1} &\left[(1-K_a)(1-K_b) - K_a K_b \left(\frac{b}{a}\right)^{2\ell+1} \right]^{-1} \\ &\times \left[(1-K_b) \frac{U_a}{\bar\rho} + K_b \left(\frac{b}{a}\right)^{\ell+2} \frac{U_b}{\bar\rho} + \frac{\Delta\rho_{mo}}{\bar\rho} \right. \\ &\times \left. \left(1 - K_b + \left(\frac{b}{a}\right)^{2\ell+1} K_b \right) A_\ell^m + \frac{\Delta\rho_{cm}}{\bar\rho} \left(\frac{b}{a}\right)^{\ell+2} B_\ell^m \right],\end{aligned} \tag{VII.3}$$

in which

$$U_a = \int_b^a \left(\frac{r'}{a}\right)^{\ell+2} (\rho_1)_\ell^m(r')\, dr', \qquad U_b = \int_b^a \left(\frac{b}{r'}\right)^{\ell-1} (\rho_1)_\ell^m(r')\, dr',$$

$$K_a = \frac{3}{2\ell + 1}\frac{\Delta\rho_{mo}}{\bar{\rho}}, \qquad K_b = \frac{3}{2\ell + 1}\left(\frac{b}{a}\right)\frac{\Delta\rho_{cm}}{\bar{\rho}},$$

where $\bar{\rho} = 5.52$ Mg/m^3 is the Earth's mean density, A_ℓ^m is the surface topography in the absence of self-gravitation [i.e., when $(\phi_1)_\ell^m(a) = 0$ in Eq. (162)], and B_ℓ^m is the CMB topography in the absence of self-gravitation [i.e., when $(\phi_1)_\ell^m(b) = 0$ in Eq. (164)]. The term $(\phi_1)_\ell^m(a)/g_0$ in (VII.3) is, of course, the nonhydrostatic geoid.

References

Aki, K., and Richards, P. G. (1980). "Quantitative Seismology," Vol. II. Freeman, San Francisco.

Backus, G. E. (1958). A class of self-sustaining dissipative spherical dynamos. *Ann. Phys. (Leipzig)* [7] **4,** 372–447.

Backus, G. E. (1967). Converting vector and tensor equations to scalar equations in spherical coordinates. *Geophys. J. R. Astron. Soc.* **13,** 71–101.

Batchelor, G. K. (1967). "An Introduction to Fluid Dynamics." Cambridge Univ. Press, Cambridge, UK.

Borch, R. S., and Green, H. W., II (1987). Dependence of creep in olivine on homologous temperature and its implications for flow in the mantle. *Nature (London)* **330,** 345–348.

Čadek, O., Ricard, Y., Martinec, Z., and Matyska, C. (1993). Comparison between Newtonian and non-Newtonian flow driven by internal loads. *Geophys. J. Int.* **112,** 103–114.

Carter, N. L. (1976). Steady state flow of rocks. *Rev. Geophys. Space Phys.* **14,** 301–360.

Christensen, U. (1984). Convection with pressure- and temperature-dependent non-Newtonian rheology. *Geophys. J. R. Astron. Soc.* **77,** 343–384.

Christensen, U., and Harder, H. (1991). 3-D convection with variable viscosity. *Geophys. J. Int.* **104,** 213–226.

Coble, R. L. (1963). A model for boundary diffusion controlled creep in polycrystalline materials. *J. Appl. Phys.* **34,** 1679–1682.

Condon, E. U., and Shortley, G. H. (1963). "The Theory of Atomic Spectra." Cambridge Univ. Press, Cambridge, UK.

DeMets, C., Gordon, R. G., Argus, D. F., and Stein, S. (1990). Current plate motions. *Geophys. J. Int.* **101,** 425–478.

Edmonds, A. R. (1960). "Angular Momentum in Quantum Mechanics." Princeton Univ. Press, Princeton, NJ.

Forte, A. M. (1992). The kinematics and dynamics of poloidal-toroidal coupling of mantle flow. *EOS, Trans. Am. Geophys. Union* **73,** 273, Spring Meet. Suppl.

Forte, A. M., and Peltier, W. R. (1987). Plate tectonics and aspherical Earth structure: The importance of poloidal-toroidal coupling. *J. Geophys. Res.* **92,** 3645–3679.

Forte, A. M., and Peltier, W. R. (1991a). Viscous flow models of global geophysical observables. I. Forward problems. *J. Geophys. Res.* **96,** 20,131–20,159.

Forte, A. M., and Peltier, W. R. (1991b). Gross Earth data and mantle convection: New inferences of mantle viscosity. *NATO ASI Series* **334,** 425–444.

Forte, A. M., Woodward, R. L., Dziewonski, A. M., and Peltier, W. R. (1992). 3-D Models of mantle heterogeneity derived from joint inversions of seismic and geodynamic data. *EOS, Trans. Am. Geophys. Union* **73,** 200, Spring Meet. Suppl.

Forte, A. M., Peltier, W. R., Dziewonski, A. M., and Woodward, R. L. (1993a). Dynamic surface topography: A new interpretation based upon mantle flow models derived from seismic tomography. *Geophys. Res. Lett.* **20,** 225–228.

Forte, A. M., Dziewonski, A. M., and Woodward, R. L. (1993b). Aspherical structure of the mantle, tectonic plate motions, nonhydrostatic geoid, and topography of the core-mantle boundary. *AGU Geodyn. Series* **72,** 135–166.

Gable, C. W., O'Connell, R. J., and Travis, B. J. (1991). Convection in three dimensions with surface plates: Generation of toroidal flow. *J. Geophys. Res.* **96,** 8391–8405.

Goldstein, H. (1980). "Classical Mechanics," 2nd ed. Addison-Wesley, Reading, MA.

Green, H. W. (1970). Diffusional flow in polycrystalline materials. *J. Appl. Phys.* **41,** 3899–3901.

Hager, B. H., and Clayton, R. W. (1989). Constraints on the structure of mantle convection using seismic observations, flow models, and the geoid. *In* "Mantle Convection" (W. R. Peltier, ed.), pp. 657–763. Gordon & Breach, New York.

Hager, B. H., and O'Connell, R. J. (1981). A simple global model of plate dynamics and mantle convection. *J. Geophys. Res.* **86,** 4843–4867.

Hager, B. H., and Richards, M. A. (1989). Long-wavelength variations in the Earth's geoid: Physical models and dynamical implications. *Philos. Trans. R. Soc. London, Ser.* **328,** 309–327.

Hager, B. H., Clayton, R. W., Richards, M. A., Comer, R. P., and Dziewonski, A. M. (1985). Lower mantle heterogeneity, dynamic topography and the geoid. *Nature (London)* **313,** 541–545.

Herring, C. (1950). Diffusional viscosity of a polycrystalline solid. *J. Appl. Phys.* **21,** 437–495.

Jarvis, G. T., and McKenzie, D. P. (1980). Convection in a compressible fluid with infinite Prandtl number. *J. Fluid Mech.* **96,** 515–583.

Jarvis, G. T., and Peltier, W. R. (1982). Mantle convection as a boundary layer phenomenon. *Geophys. J. R. Astron. Soc.* **68,** 385–424.

Justice, J. H. (1978). Two-dimensional recursive filtering in theory and practice. *In* "Applied Time Series Analysis" (D. F. Findley, ed.). Academic Press, New York.

Karato, S.-I., Paterson, M. S., and Fitzgerald, J. D. (1986). Rheology of synthetic olivine aggregates: Influence of grain size and water. *J. Geophys. Res.* **91,** 8151–8176.

Kohlstedt, D. L., and Hornack, P. (1981). Effect of oxygen partial pressure on the creep of olivine. *AGU Geodyn. Series* **4,** 101–107.

Lanczos, C. (1961). "Linear Differential Operators." Van Nostrand, New York.

LeBlanc, R. (1986). "New Perspective on the $U(n)$ Wigner-Racah calculus: III. A Note on $SU(2)$ Wigner Coefficients." Prepr. NP86103. University of Michigan, Ann Arbor.

LeBlanc, R. (1987). New perspective on the $U(n)$ Wigner-Racah calculus: III. Applications to $U(2)$ and $U(3)$. *J. Phys. A: Math. Gen.* **20,** 5015–5021.

Martinec, Z., Matyska, C., Čadek, O., and Hrdina, P. (1993). The Stokes problem with 3D Newtonian rheology in a spherical shell. *Comput. Phys. Commun.* **76,** 63–79.

McKenzie, D. P., Roberts, J. M., and Weiss, N. O. (1974). Convection in the Earth's mantle: Towards a numerical simulation. *J. Fluid Mech.* **62,** 465–538.

Minster, J. B., and Jordan, T. H. (1978). Present-day plate motions. *J. Geophys. Res.* **83,** 5331–5354.

Morse, P. M., and Feshbach, J. (1953). "Methods of Theoretical Physics," Vols. I and II. McGraw-Hill, New York.

Nicolas, A., and Poirier, J.-P. (1976). "Crystalline Plasticity and Solid State Flow in Metamorphic Rocks." Wiley, New York.

O'Connell, R. J., Gable, C. W., and Hager, B. H. (1991). Toroidal-poloidal partitioning of lithospheric plate motions. *NATO ASI Series* **334,** 535–551.

Olson, P., and Bercovici, D. (1991). On the equipartitioning of kinetic energy in plate tectonics. *Geophys. Res. Lett.* **18,** 1751–1754.

Pekeris, C. L. (1935). Thermal convection in the interior of the Earth. *Mon. Not. R. Astron. Soc., Geophys. Suppl.* **3,** 343–367.

Peltier, W. R. (1972). Penetrative convection in the planetary mantle. *Geophys. Astrophys. Fluid Dyn.* **5,** 47–88.

Peltier, W. R. (1982). Dynamics of the ice age Earth. *Adv. Geophys.* **24,** 1–146.

Peltier, W. R. (1985). Mantle convection and viscoelasticity. *Annu. Rev. Fluid Mech.* **17,** 561–608.

Peltier, W. R. (1989). Mantle viscosity. *In* "Mantle Convection" (W. R. Peltier, ed.), pp. 389–478. Gordon & Breach, New York.

Peltier, W. R., and Solheim, L. P. (1992). Mantle phase transitions and layered chaotic convection. *Geophys. Res. Lett.* **19,** 321–324.

Phinney, R. A., and Burridge, R. (1973). Representation of the elastic-gravitational excitation of a spherical Earth model by generalized spherical harmonics. *Geophys. J. R. Astron. Soc.* **34,** 451–487.

Ribe, N. M. (1992). The dynamics of twin shells with variable viscosity and the origin of toroidal flow. *Geophys. J. Int.* **110,** 537–552.

Ricard, Y., and Vigny, C. (1989). Mantle dynamics with induced plate tectonics. *J. Geophys. Res.* **94,** 17,543–17,559.

Ricard, Y., Fleitout, L., and Froidevaux, C. (1984). Geoid heights and lithospheric stresses for a dynamic Earth. *Ann. Geophys. (Gauthier-Villars)* **2,** 267–286.

Ricard, Y., Froidevaux, C., and Fleitout, L. (1988). Global plate motion and the geoid: A physical model. *Geophys. J. Int.* **93,** 477–484.

Ricard, Y., Doglioni, C., and Sabadini, R. (1991). Differential rotation between lithosphere and mantle: A consequence of lateral mantle viscosity variations. *J. Geophys. Res.* **96,** 8407–8415.

Richards, M. A., and Engebretson, D. C. (1992). Large-scale mantle convection and the history of subduction. *Nature (London)* **355,** 437–440.

Richards, M. A., and Hager, B. H. (1984). Geoid anomalies in a dynamic Earth. *J. Geophys. Res.* **89,** 5987–6002.

Richards, M. A., and Hager, B. H. (1989). Effects of lateral viscosity variations on long-wavelength geoid anomalies and topography. *J. Geophys. Res.* **94,** 10,299–10,313.

Ricoult, D. L., and Kohlstedt, D. L. (1985). Experimental evidence for the effect of chemical environment upon the creep rate of olivine. *AGU Geophys. Monogr., Am. Geophys. Union* **31,** 171–184.

Romanowicz, B., and LeStunff, Y. (1993). Upper mantle Q tomography and the viscosity profile of the mantle. *EOS, Trans. Am. Geophys. Union* **74,** 439, Fall Meet. Suppl.

Solheim, L. P., and Peltier, W. R. (1990). Heat transfer and the onset of chaos in an axisymmetric, anelastic model of whole mantle convection. *Geophys. Astrophys. Fluid Dyn.* **53,** 205–255.

Solheim, L. P., and Peltier, W. R. (1993). Mantle phase transitions and layered convection. *C.J. Earth Sci.* **30,** 881–893.

Solheim, L. P., and Peltier, W. R. (1994). Avalanche effects in phase transition modulated thermal convection: A model of the earth's mantle. *J. Geophys. Res.* **99,** 6997–7018.

Stewart, C. A. (1992). Thermal convection in the Earth's mantle: Mode coupling induced by temperature-dependent viscosity in a 3-dimensional spherical shell. *Geophys. Res. Lett.* **19,** 337–340.

Stocker, R. L., and Ashby, M. F. (1973). On the rheology of the upper mantle. *Rev. Geophys. Space Phys.* **11,** 391–426.

Su, W.-J., and Dziewonski, A. M. (1992). On the scale of mantle heterogeneity. *Phys. Earth Planet. Inter.* **74,** 29–54.

Tackley, P. J. (1993). Effects of strongly temperature-dependent viscosity on time-dependent three-dimensional models of mantle convection. *EOS, Trans. Am. Geophys. Union* **74,** 79, Fall Meet. Suppl.

Turcotte, D. L., and Oxburgh, E. R. (1967). Finite amplitude convective cells and continental drift. *J. Fluid Mech.* **28,** 29–42.

Weertman, J. (1968). Dislocation climb theory of steady state creep. *Trans. Am. Soc. Met.* **61,** 681–694.

Weertman, J. (1978). Creep laws for the mantle of the Earth. *Philos. Trans. R. Soc. London, Ser. A.* **288,** 9–26.

Weertman, J., and Weertman, J. R. (1975). High temperature creep of rock and mantle viscosity. *Annu. Rev. Earth Planet. Sci.* **3,** 293–315.

Woodward, R. L., Forte, A. M., Su, W.-J., and Dziewonski, A. M. (1993). Constraints on the large-scale structure of the Earth's mantle. *AGU Geophys. Monogr. Am. Geophys. Union* **74,** 89–109.

Zerr, A., and Boehler, R. (1993). Melting of (Mg,Fe)SiO_3 perovskite to 650 Kbar: Indication of very high melting temperature in the lower mantle. *Science* **262,** 553–555.

Zhang, S., and Christensen, U. (1993). Some effects of lateral viscosity variations on geoid and surface velocities induced by density anomalies in the mantle. *Geophys. J. Int.* **114,** 531–547.